Monitoring Dynamic Properties of Railway Tracks Using Train-borne Vibrometer Measurement

Zeng, Y.

Important note
To cite this publication, please use the final published version (if applicable).
Please check the document version above.

MONITORING DYNAMIC PROPERTIES OF RAILWAY TRACKS USING TRAIN-BORNE VIBROMETER MEASUREMENT

MONITORING DYNAMIC PROPERTIES OF RAILWAY TRACKS USING TRAIN-BORNE VIBROMETER MEASUREMENT

Dissertation

for the purpose of obtaining the degree of doctor
at Delft University of Technology
by the authority of the Rector Magnificus prof.dr.ir. T.H.J.J. van der Hagen
chair of the Board for Doctorates
to be defended publicly on
Monday 4 December 2023 at 10:00 o'clock

by

Yuanchen ZENG

Bachelor of Engineering in Mechatronics, Zhejiang University, China
born in Hebei, China

This dissertation has been approved by the promotors.

Composition of the doctoral committee:

Rector Magnificus	chairperson
Prof.dr. Z. Li	Delft University of Technology, promotor
Dr. A.A. Núñez Vicencio	Delft University of Technology, copromotor

Independent members:
Prof.dr. R.P.B.J. Dollevoet	Delft University of Technology
Prof.dr. B.H.K. De Schutter	Delft University of Technology
Prof.dr. M. Veljkovic	Delft University of Technology
Prof.dr. W. Zhang	Southwest Jiaotong University, China
Prof.dr. D. Galar	Luleå University of Technology, Sweden

CONTENTS

SUMMARY

Monitoring the dynamic properties of railway tracks is essential for the safety of train operation and the efficiency of track maintenance. Several vibration-based technologies are available for measuring such properties, but each has its limitations such as low efficiency and limited frequency band. There is still a lack of train-borne technologies applicable to extracting the load-response relationship of track structures, especially when a variety of track components and a wide frequency range are concerned. A laser Doppler vibrometer (LDV) is a noncontact sensing instrument for vibration measurement. A train-borne LDV can target its laser spot on tracks, continuously scan track structures during train operation, and directly measure track vibrations in response to the moving train. It has the potential to complement existing technologies and monitor the dynamic properties of railway tracks.

This dissertation develops a new technology based on train-borne LDV for measuring the vibration and load-response relationship of railway tracks over a wide frequency range. To address the key challenges discussed in Chapter 1, the developed technology consists of four interconnected cornerstones, corresponding to Chapter 2~5.

Chapter 2 reduces speckle noise in LDV measurements on a moving platform. Speckle noise is problematic for such measurements due to the drastic in-plane motion of the laser spot on target surfaces. It is found that as the moving speed increases, the speckle noise occurs more frequently with shorter durations, greater amplitudes, and broader frequency bands. A three-step framework is proposed for removing the speckle noise in the post-processing stage, which works by detecting and replacing spikes and then smoothing out residual noise. Specifically, we develop a wavelet-based spike detection method in Step 1, an autoregressive integrated moving average-based imputation method in Step 2, and adopt a Butterworth filter in Step 3. The method is validated in the TU Delft V-Track test rig at different locations along the track and at different speeds (0.5~20 km/h). The LDV effectively captures the dominant track vibrations at 500~700 Hz with good repeatability between different laps and good agreement with trackside measurements in V-Track. In addition to the proposed methods, different alternative methods can be adapted and used in the three steps of the framework.

Chapter 3 identifies modal parameters from structural vibration response under operational conditions. Effective analysis of vibration response without load information is crucial for structural condition monitoring. Time-frequency representation is necessary for analyzing train-track vibration response due to its nonstationary characteristics and broadband nature. An operational modal analysis method in time-frequency representation is developed. Short-time frequency domain decomposition and a convolution-based strategy are proposed to obtain singular values and local mode shape similarity, respectively, which are further fused into mode indicators by a fuzzy-based strategy. The method is an interpretable and explicit tool that provides not only a global view of the modal characteristics over time and frequency but also estimates of modal parameters. It is applicable to strongly nonstationary responses under time-varying loads and conditions and also robust to the length of signals. The method is validated using sleeper vibrations under train passage at speeds of 8 km/h in V-Track

and 15~200 km/h in field tests. The rigid-body motions and bending modes of the sleepers are identified at frequencies up to 6,500 Hz in V-Track and 4,500 Hz in the field tests, and the identification results are comparable to hammer tests.

Chapter 4 investigates the speed-dependent characteristics of track vibration measurement with a train-borne LDV. In a train-borne LDV system, the train speed affects both the intensity of track vibrations and speckle noise. The quality of train-borne LDV signals is essential to their usability. A holistic methodology for characterizing train-borne LDV measurements is proposed combining numerical simulations, laboratory measurements in V-Track, and field measurements on the CTO measurement train. Validated models are used to separately simulate sleeper vibrations and speckle noise at different speeds. A vibration-noise separation method is developed and validated to separate structural vibration from speckle noise adaptively at different speeds and robustly under different scenarios. Simulations and measurements show that as train speed increases (from 2 to 12 km/h in V-Track and from 5 to 30 km/h on the CTO train), speckle noise increases almost linearly while track vibration (at frequencies up to 1,500 Hz in V-Track and 300 Hz on the CTO train) increases nonlinearly. This difference leads to the nonlinear behavior of the signal-to-noise ratio with respect to train speed. The speeds that yield the highest signal-to-noise ratio are different for different tack structures, measurement configurations, and operational conditions.

Chapter 5 estimates railway track transfer functions from LDV and accelerometer measurements on a moving vehicle. Characterizing the load-response relationship of railway tracks requires both wheel-rail force (input) and track vibration response (output). Operational modal analysis is applied to vehicle impact response at a joint to obtain its modal parameters, which further support the estimation of dynamic wheel-rail forces from vehicle vibrations using a Duhamel integral-based method. Meanwhile, a speed-adaptive despeckle and compensation method is applied to LDV signals to reduce speckle noise and extract track vibrations. Railway track transfer functions are then estimated using the estimated wheel-rail force as input and the extracted track vibrations as output. The proposed method is validated in laboratory measurements in V-Track at different track locations (with or without joints) and speeds (8~16 km/h). The estimated transfer functions are compared with trackside measurements and hammer tests, and they show good agreement at 200~800 Hz. The differences in the estimated transfer functions between different track sections reflect the variation of track dynamic properties.

This dissertation concludes with Chapter 6. In general, this dissertation investigates the train-borne LDV technology for track vibration measurement at three levels. First, numerical simulations provide insights into the mechanisms and characteristics of speckle noise and track vibration. Second, laboratory measurements in V-Track provide well-controlled and well-observed conditions for testing the train-borne LDV technology, and the highest speed tested is 20 km/h. Third, field measurements on the CTO train provide realistic conditions to further test the technology and the associated methods, and the highest speed tested is 30 km/h. The investigations yield coherent results and demonstrate the feasibility and usability of the train-borne LDV technology for measuring track dynamic properties, thus potentially enabling more efficient and informative rail infrastructure monitoring.

SAMENVATTING

Het monitoren van de dynamische eigenschappen van spoorconstructies is essentieel voor zowel de veiligheid van railvervoer als de efficiëntie van spooronderhoud. Voor het meten van deze eigenschappen zijn nu al diverse, op trillingen gebaseerde, technologieën beschikbaar maar elk heeft zijn beperkingen, zoals een lage efficiency en een beperkte frequentieband. Het ontbreekt nog altijd aan een systeem voor het meten van trillingen dat direct onder een railvoertuig kan worden gemonteerd en waarmee de relatie tussen de dynamische respons en belasting van spoorconstructies kan worden bepaald in een breed frequentiebereik. Een laser-Doppler-vibrometer (LDV) is een contactloos meetinstrument voor trillingsmetingen. Een op een trein gemonteerde LDV (trein-gebonden LDV) kan zijn laserspot op het spoor richten, en tijdens het rijden de spoorconstructie continu scannen en daarbij direct de trillingen in het spoor meten als reactie op de bewegende trein. LDV heeft de potentie om de bestaande technologieën voor monitoring van het spoor aan te vullen en daarbij tevens de dynamische eigenschappen van spoorconstructies te bepalen.

Dit proefschrift beschrijft de ontwikkeling van nieuwe technologie om met een trein-gebonden LDV de trillingen en de relatie tussen de respons en de belasting van spoorconstructies te meten over een breed frequentiebereik. Om de belangrijkste uitdagingen zoals besproken in Hoofdstuk 1 aan te pakken, bestaat de ontwikkelde technologie uit vier pijlers, overeenkomend met Hoofdstukken 2~5.

Hoofdstuk 2 behandelt de vermindering van spikkelruis in LDV-metingen vanaf een bewegend platform. Spikkelruis is problematisch voor dergelijke metingen vanwege de significante in-plane beweging van de laserspot op doeloppervlakken. In hoofdstuk 2 wordt aangetoond dat naarmate de treinsnelheid toeneemt, spikkelruis vaker voorkomt met een kortere duur, grotere amplitudes en bredere frequentiebanden. Er wordt een raamwerk in drie stappen voorgesteld voor het verwijderen van de spikkelruis in de nabewerkingsfase, gericht op het detecteren en vervangen van pieken en het vervolgens glad maken van de resterende ruis. We ontwikkelen hiermee een op wavelet-gebaseerde piek-detectiemethode in Stap 1, een vervangingstechniek gebaseerd op autoregressieve geïntegreerde bewegende gemiddelden in Stap 2 en het gebruiken van een Butterworth-filter in Stap 3. De methode is getest met de TU Delft V-Track op verschillende posities op het spoor van de testopstelling en bij verschillende snelheden (0.5~20 km/u). De LDV legt effectief de dominante spoorvibraties vast bij 500~700 Hz met goede herhaalbaarheid tussen verschillende testronden en goede overeenstemming met aparte metingen langs het spoor van de V-Track. Naast de voorgestelde methoden kunnen verschillende alternatieve methoden worden aangepast en gebruikt in de drie stappen van het raamwerk.

Hoofdstuk 3 gaat over de identificatie van de modale parameters uit de structurele trillingsrespons onder operationele omstandigheden. Effectieve analyse van de trillingsrespons zonder belastingsinformatie is cruciaal voor structural health monitoring. Een tijd-frequentieweergave is noodzakelijk voor de analyse van trein-spoor trillingen vanwege de niet-stationaritaire eigenschappent en het brede frequentiebereik van het signaal. Een methode voor operationele modale analyse in de tijd-frequentieweergave wordt ontwikkeld. Korte-tijd-frequentiedomein-decompositie en een op convolutie-gebaseerde benadering worden voorgesteld om singuliere waarden en lokale modusvormgelijkenis te verkrijgen, die vervolgens worden samengevoegd tot modusindicatoren met behulp van een fuzzy-gebaseerde aanpak. De methode is een interpreteerbaar - en expliciet instrument dat niet alleen een algemeen beeld geeft van de modale kenmerken in de tijd en frequentie, maar die ook schattingen van modale parameters mogelijk maakt. Het is toepasbaar op sterk niet-stationaire reacties onder tijdsafhankelijke

belastingen en omstandigheden en is ook robuust ten opzichte van de signaallengte. De methode is getest met dwarsliggertrillingen bij treinpassage onder snelheden van 8 km/u in V-Track en 15~200 km/u in veldtests. De starre lichaamsbewegingen en buigingsmodussen van de dwarsliggers zijn herkenbaar bij frequenties tot 6,500 Hz in V-Track en 4,500 Hz in de veldtests. De resultaten zijn vergelijkbaar met hamertesten.

Hoofdstuk 4 gaat over onderzoek naar de snelheidsafhankelijke kenmerken van spoortrillingsmetingen met een aan de trein-gebonden LDV. De snelheid van de trein beïnvloedt zowel de intensiteit van spoortrillingen als de spikkelruis. De kwaliteit van het LDV-signaal is essentieel voor de toepasbaarheid voor monitoring. Een holistische methodologie voor de karakterisering van trein-gebonden LDV metingen wordt voorgesteld, waarbij numerieke simulaties, laboratoriummetingen in V-Track en veldmetingen op de CTO-meettrein worden gecombineerd. Gevalideerde modellen worden gebruikt om afzonderlijke dwarsliggertrillingen en spikkelruis te simuleren bij verschillende snelheden. Een methode voor het onderscheiden van structurele trillingen en ruis is ontwikkeld en gevalideerd, adaptief bij verschillende snelheden en robuust onder verschillende omstandigheden. Simulaties en metingen tonen aan dat naarmate de snelheid van de trein toeneemt (van 2 tot 12 km/u in V-Track en van 5 tot 30 km/u op de CTO-trein), het spikkelruis vrijwel lineair toeneemt, terwijl de spoortrillingen (bij frequenties tot 1,500 Hz in V-Track en 300 Hz op de CTO-trein) niet-lineair toenemen. Dit onderscheid leidt tot het niet-lineaire gedrag van de signaal-ruisverhouding in relatie tot de snelheid van de trein. De snelheden die de hoogste signaal-ruisverhouding opleveren, zijn verschillend voor diverse spoorconstructies, meetconfiguraties en operationele omstandigheden.

Hoofdstuk 5 betreft een schatting van de overdrachtsfuncties van spoorconstructies van LDV- en versnellingsmetingen vanaf een bewegend voertuig. Het karakteriseren van de relatie tussen de respons en de belasting van spoorconstructies vereist zowel een kracht vanuit het wiel-rail-raakvlak (input) als de trillingsrespons van het spoor (output). Operationele modale analyse wordt toegepast op de voertuig-impact respons bij een raillas om de modale parameters te verkrijgen, die vervolgens een schatting van de dynamische wiel-rail kracht mogelijk maken uit voertuigtrillingen met behulp van een methode op basis van Duhamel-integraal. Tegelijkertijd wordt een snelheidsadaptieve ontspikkel- en compensatiemethode toegepast op de LDV-signalen om het spikkelruis te verminderen en spoorvibraties te extraheren. De overdrachtsfuncties van spoorconstructies worden vervolgens bepaald met de geschatte wiel-rail kracht als input en de geëxtraheerde spoorvibraties als output. De voorgestelde methode is getest in laboratoriummetingen met de V-Track op verschillende posities op de testopstelling, met en zonder raillassen en onder verschillende snelheden (8~16 km/u). De geschatte overdrachtsfuncties zijn vergeleken met metingen en hamertesten op de testopstelling en vertonen goede overeenstemming tussen de 200 Hz en 800 Hz. De verschillen in de geschatte overdrachtsfuncties tussen verschillende spoorwegsecties weerspiegelen de variatie van de dynamische eigenschappen van het spoor.

Dit proefschrift wordt afgesloten met Hoofdstuk 6. In het algemeen onderzoekt dit proefschrift voor trein-gebonden LDV-technologie voor trillingsmetingen van spoorconstructies op drie niveaus. Ten eerste bieden numerieke simulaties inzicht in de mechanismen en kenmerken van het spikkelruis en de spoortrillingen. Ten tweede bieden laboratoriummetingen met de V-Track goed beheersbare en goed meetbare condities voor het testen van trein-gebonden LDV-technologie, en de hoogst geteste snelheid is 20 km/u. Ten derde bieden veldmetingen op de CTO-trein realistische omstandigheden om de technologie en de bijbehorende methoden verder te testen, en de hoogst geteste snelheid is 30 km/u. De onderzoeken leveren coherente resultaten op en tonen de haalbaarheid en bruikbaarheid aan van LDV-technologie voor het meten van de dynamische eigenschappen van spoorwegen, hetgeen in potentie meer efficiënte en meer gedetailleerde monitoring van spoorweginfrastructuur mogelijk maakt.

1

INTRODUCTION

1.1. Background

Dynamic properties of railway tracks affect the load-bearing capacity of rail infrastructure, the interaction between trains and tracks, and the safety and ride quality of train operations. Due to train load and aging, track dynamic properties degrade over time and deviate over different locations. Thus, monitoring these properties for well-informed, effective, and efficient track maintenance is essential [1, 2].

Structural vibration measurement is an effective approach to monitoring dynamic properties [3, 4]. Existing vibration-based technologies for monitoring track dynamic properties are summarized in Table 1.1. Some examples are shown in Figure 1.1.

Table 1.1: Existing vibration-based technologies for monitoring track dynamic properties.

Technologies	Excitation	Response sensing	Advantages	Disadvantages
Impact modal test [5~8]	Impact on railhead by a hammer or a falling weight with a force transducer	Accelerometers on rails or sleepers	Low noise, high repeatability, high coherence	Unloaded, labor-intensive, need different hammers, require operation shutdown
Pass-by measurement [9~13]	Passing trains	Accelerometers or geophones on rails or sleepers or track slabs	Different train loads, low noise	Unknown train load, cost-prohibitive for large-scale monitoring
Vehicle vibration measurement [14~22]	A running train	Accelerometers on axle boxes or bogie frames or car body	Low cost, high speed, efficient for large-scale monitoring	Less sensitive to components below rails
Specialized stiffness measurement train [23, 24]	Periodic load from an oscillating mass	Accelerometers on wheels and oscillating mass	Measure dynamic stiffness	A single frequency at a time, limited train speed
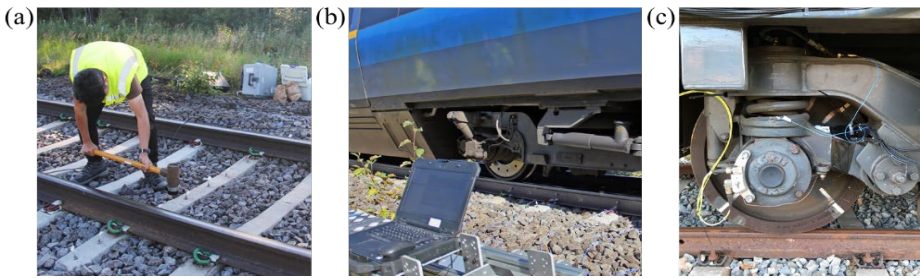
Figure 1.1: Examples of vibration-based technologies for measuring track dynamic properties. (a) Impact hammer test; (b) Pass-by measurement; (c) Vehicle vibration measurement.

Impact modal tests and pass-by measurements are usually applied only at hot spots due to their high costs. In contrast, train-borne technologies are more efficient for large-scale monitoring. In vehicle vibration measurements, railway tracks are monitored indirectly through wheel-rail contact, so the load on tracks and the response of tracks are

coupled in vehicle vibrations. Stiffness measurement trains excite track structures with controlled loads at a single frequency. In general, there is still a lack of train-borne technologies suitable for measuring the dynamic response of track components below rails and extracting their load-response relationship in a wide range of frequencies.

A laser Doppler vibrometer (LDV) is a laser-based sensing instrument that measures the vibration velocity of a target based on its Doppler frequency shift, i.e., the change in laser frequency proportional to the relative velocity between the laser source and the target. The noncontact sensing nature of LDV has the advantages of accessing places unsuitable for contact-based sensors, measuring different objects or locations with the same instrumentation, and avoiding the influence of sensor mass on target dynamics. It can provide high accuracy and sensitivity for vibration measurements over a wide range of frequencies and has been applied to many engineering structures for modal identification and damage detection [25~27]. In most existing applications, LDVs are set statically for measuring at discrete points or along closed paths [25~27]. Alternatively, an LDV can be mounted on a train to target its laser spot on tracks, scan track structures during train operation, and measure track vibrations in response to the moving train [28]. In a simulation study, train-borne LDVs are used to identify the mode shapes of a bridge [29]. In experimental studies, train-borne LDVs are used to measure the rail vibrations in order to identify rail bending modes [30] and detect welds [31].

Train-borne LDV has the potential to complement existing track monitoring technologies to monitor track dynamic properties. It enables direct and continuous vibration measurement of various track components and further supports estimating the load-response relationship of railway tracks. We are unaware of previous research using this technology to monitor track components below rails, such as sleepers. However, there are still many challenges in applying train-borne LDV to rail infrastructure monitoring, and some will be discussed in the next section.

1.2. QUESTIONS AND CHALLENGES

The following research questions are answered in this dissertation.

- How does noise behave in LDV signals? How to mitigate severe speckle noise at high moving speeds?

- How to interpret vibration response under operational conditions without load information? How to identify dynamic properties from structural vibrations?

- How does a train-borne LDV perform in measuring railway track vibrations? How to characterize the influence of train speed on its performance?

- How to define and estimate the load-response relationship of railway tracks from a moving vehicle?

The challenges behind the above research questions are further discussed as follows.

1.2.1. HOW TO MITIGATE SPECKLE NOISE AT HIGH MOVING SPEEDS?

Speckle noise has been reported as a major noise source in LDV measurements [25~27]. It originates from speckle patterns that appear when a laser beam is scattered on an

optically rough surface [32]. In signals measured by an LDV, speckle noise appears as random spikes in time and broadband noise floor in spectra [27]. The severity of speckle noise depends not only on laser and target properties but also on the change of speckle patterns due to the relative motion between laser and target [27, 32]. Therefore, different measurement setups of LDV usually show different severity of speckle noise. Depending on the number of measurement locations, this dissertation classifies LDV measurement setups into discrete measurement and continuous measurement. Table 1.2 summarizes the influence of speckle noise for different measurement setups from the literature. Compared to the discrete measurement category, speckle noise is more troublesome for the continuous measurement category due to more drastic changes in speckle patterns. Speckle noise is more severe at higher scanning or moving speeds.

Table 1.2: Speckle noise in different LDV measurement setups.

Categories	Measurement setups	Influence of speckle noise
Discrete measurement (at one or multiple discrete locations)	**Single-point LDV**: The laser spot is targeted at a fixed point [33~37]. **Stepped scanning LDV**: The laser spot scans along selected points stepwise and dwells at each for a duration [38~40]. Most setups are used for modal analysis.	• Some of the literature encounters the speckle noise problem. • Speckle noise occurs locally and occasionally.
Continuous measurement (along a continuous path)	**Continuous scanning LDV**: The laser spot repeatedly scans an object continuously along a closed path [41~49]. Most setups are used for modal analysis.	• Most of the literature encounters the speckle noise problem. • Speckle noise is quasi-periodic. • Speckle noise gets more severe at higher scanning frequencies.
	LDV on moving platform (LDVom): The laser spot scans an object continuously along an open path [28~30, 50~53]. Most setups are used for large-scale structures.	• Most of the literature encounters the speckle noise problem. • Speckle noise is highly irregular. • Speckle noise gets more severe at higher moving speeds.

Over the past years, manufacturers and users have been working on mitigating speckle noise in LDV measurements. Table 1.3 summarizes the existing approaches for different measurement setups from the literature. They are classified into three stages – instrumentation, measurement, and post-processing. The approaches in the three stages should be combined to achieve the best signal quality, especially in challenging situations. In the instrumentation stage, innovations in LDV technology enable users to improve signal quality by properly selecting LDV equipment. In the measurement stage, users can mitigate speckle noise by optimizing measurement settings or treating target surfaces. However, an LDV on moving platform (LDVom), such as a train-borne LDV, is usually intended for measuring large-scale structures. Lowering the moving speed increases the measurement time, and surface treatment on working surfaces or large-scale structures is not possible or is expensive. Therefore, many existing approaches in the measurement stage are incompatible with train-borne LDV.

Table 1.3: Approaches for mitigating speckle noise.

Setups	Mitigation in instrumentation stage	Mitigation in measurement stage	Mitigation in post-processing stage
Single-point or stepped scanning LDV	• A tracking LDV with its laser spot tracking a target position [36].	• Treat the target surface with retroreflective tape [33].	• Kurtosis ratio-based method [34], Gaussian filter [35], decorrelation and linear prediction [37], median filter [38].
Continuous scanning LDV	*(Applicable to all setups)* • Adaptive optics [54, 55]. • High-frequency scanning average [56]. • Signal diversity with multiple detectors [54, 57, 58] or laser heads [59, 60]. • Built-in tracking filter [30, 61].	• Adjust the scanning frequency [41, 44, 45, 48], the measurement length [47, 48], and the distance between LDV and target [48]. • Treat the surface with retroreflective tape [46].	• Smooth the identified mode shapes [45~47]. • Neglect frequencies related to the scanning frequency [41]. • Windowing [44], wavelet or high-pass filter-based spike removal [49].
LDV on moving platform	• A mobile LDV with a large spot size [51].	• Adjust the sensitivity and the moving speed [52].	• Kurtosis and linear prediction [53], empirical wavelet transform [62], Fourier analysis [63], ensemble empirical mode decomposition [64].

Further, speckle noise can be reduced in the post-processing stage. For continuous scanning LDV, the availability of repeated measurements allows speckle noise reduction, such as by averaging multiple measurements or neglecting frequencies related to the scanning frequency. However, for LDVom measurements on large-scale structures or structures under time-varying excitations, repeated measurements are not possible or are expensive. Therefore, signal processing is necessary. Many conventional filtering or denoising methods are available for this, but they may yield unsatisfactory performance since they are not tailored to handle speckle noise [62]. For example, low-pass filters can smooth speckle noise but not remove it [43].

Therefore, specialized signal processing methods have been developed to reduce speckle noise. For discrete measurements, the ratio of the kurtosis of a raw signal to the kurtosis of its trimmed version is used to select the undistorted part of a signal [34]. In [37], speckle noise is detected using short-time energy and kurtosis and then replaced through linear prediction. A few methods have been developed for continuous LDV measurements where speckle noise occurs more frequently. In [49], speckle noise is detected based on high-pass filtering or wavelet transform and removed through interpolation or curve fitting. In [53], speckle noise is detected based on the kurtosis ratio and replaced through linear prediction. In [62], speckle noise is reduced using empirical wavelet transform. These methods are tested at the scanning speed of 0.05 m/s, 0.01 m/s, and 0.1 m/s, respectively. Reducing speckle noise is more challenging at higher speeds. In [63], low-pass filtering and oscillation detrending are combined to reduce speckle noise, and it is tested for a case of harmonic vibrations at speeds up to 20 m/s. In [64],

1

an ensemble empirical mode decomposition method is proposed and validated at the speed of 0.85 m/s and 2.8 m/s in two experiments, respectively. Therefore, further development and validation of post-processing methods are needed to reduce speckle noise in non-periodic vibration measurements with LDVom at high speeds.

1.2.2. HOW TO IDENTIFY DYNAMIC PROPERTIES FROM VIBRATIONS?

For vibration-based condition monitoring of large-scale structures, it is usually difficult or expensive to excite structures with controlled loads or measure operational loads. Therefore, the interpretation of vibration response without accurate load information is crucial. Operational modal analysis (OMA) enables modal characteristics of a structure to be identified solely from the vibration response under operational loads and conditions. It does not require manual generation and sensing of excitations and has become increasingly popular in structural health monitoring.

OMA methods are generally classified into time-domain methods and frequency-domain methods. Time-domain methods are based on the analysis of time histories or correlation functions, e.g., natural excitation techniques, autoregressive moving average, stochastic subspace identification, blind source separation, and Bayesian time-domain approach [65~68]. They are usually computationally demanding and require proper selection of model order and exclusion of spurious modes [65, 66]. Frequency-domain methods are based on Fourier spectrum or power spectral density (PSD), which are naturally more interpretable. The most basic frequency-domain method is the peak-picking method [65, 66], which considers one mode at a time. Least square frequency methods [69, 70] identify multiple modes together by iteratively estimating a parameterized spectrum. Further, Bayes' theorem is incorporated to infer probability distributions of modal parameters [71], such as the spectral density approach [72], Fourier transform approach [73], Markov chain Monte Carlo approach [74], and expectation-maximization approach [75]. These Bayesian methods provide a rigorous formulation that makes full use of measurement data, but they face many challenges in solving ill-conditioned problems and estimating closely-spaced modes [76].

Frequency domain decomposition (FDD) is an extension of the peak-picking method, which can identify closely-spaced modes and does not require numerical iterations [66]. The method is used for modal analysis in [77] and then systematized to identify natural frequencies and mode shapes under broadband excitations in [78]. Since then, it has been applied to the health monitoring of many engineering structures [29, 79~81]. Meanwhile, many variants of the FDD method have been proposed in the literature. The estimation of damping ratios is achieved by converting the PSD back to the time domain (known as enhanced FDD) [82, 83] or by fitting the PSD in the narrow frequency band of a mode [84, 85]. The FDD method is further adapted for nonstationary responses or heavily damped structures by jointly using two PSD estimates and detrending the correlation function [86, 87]. Moreover, model errors and measurement noise are considered in the analysis by estimating the PSD matrix via maximum likelihood [88].

The FDD-based methods can produce a spectrum describing the dominance of modes in frequency but cannot directly capture the change of modal characteristics over time. To address this issue, a time-frequency representation is needed. Such methods based on blind source separation are developed [89, 90], but they may produce spurious

modes, and the numerical accuracy is sensitive to the number of sensors. In [91~94], continuous wavelet transform (CWT) is combined with ridge extraction, but the performance is sensitive to noise. Further, CWT is combined with singular value decomposition, but the proper selection of the mother wavelet and its parameters can be tricky because they are not directly related to structural dynamics, and a long nonstationary signal needs to be split into segments [95, 96]. Thus, spurious modes and implicit parameter design reduce the physical interpretability of OMA. To our knowledge, no existing method can produce a time-frequency representation indicating both the dominance of structural modes and the correlation of their mode shapes.

1.2.3. HOW TO CHARACTERIZE THE INFLUENCE OF TRAIN SPEED?

For track vibration measurements using a train-borne LDV, train speed is a major factor of concern. To achieve more efficient rail infrastructure monitoring, a higher speed is pursued, but this results in more severe speckle noise and a shorter length of signals when measuring a certain track section. To reduce the interference of speckle noise, a lower speed is preferred according to Section 1.2.1, but it can lead to smaller track vibrations because track response depends on the dynamic loading condition. Therefore, train speed affects train-borne LDV measurements in the following aspects.

- *Influence of train speed on track dynamics*: Track vibrations are excited by wheel-rail forces, including quasi-static components due to moving loads and dynamic components due to track irregularities [97]. As the train speed increases, wheel and sleeper passage frequencies increase linearly, and the corresponding track response amplitude first increases and then may decrease after resonance [9, 98, 99]. For the dynamic response due to irregularities, its frequencies increase linearly with the increasing train speed, while the track vibration amplitude increases first fast and then slowly [100]. Therefore, the dependency of track vibrations on train speeds is affected by several different mechanisms simultaneously, leading to a complex nonlinear behavior. In addition, a train-borne LDV measures a track component only when the laser spot scans its surface. As the train speed increases, the signal length becomes shorter, which may lead to more uncertainties in the measured response.

- *Influence of train speed on speckle noise*: In LDVom measurements, the severity of speckle noise highly depends on the speed of the moving platform, such as a running train. Simulations and experiments show that the amplitude of speckle noise increases with the increase in the in-plane speed between the laser spot and the target [48, 52, 101].

Therefore, the variation of track vibration and speckle noise with respect to train speeds affects the quality and usability of train-borne LDV signals. No published research has investigated such speed-dependent characteristics. This requires an in-depth understanding of how train speeds physically affect track vibration and speckle noise. Meanwhile, track vibration and speckle noise are mixed in real-life measurements. Therefore, effective methods are needed to separate them at various speeds in order to analyze their speed-dependent characteristics. Most of the methods for speckle noise reduction in Section 1.2.1 are developed for low speeds (<0.1 m/s) [49, 53, 62] or

harmonic vibrations [63]. The method in [64] is validated in two experiments, each with a constant speed (0.85 m/s and 2.8 m/s), and selecting parameters, such as the number of intrinsic mode functions, requires human judgment and can vary for different experiments and speeds. In the literature, there is a lack of methods capable of separating structural vibrations from speckle noise adaptively at different speeds.

1.2.4. HOW TO ESTIMATE LOAD-RESPONSE RELATIONSHIP?

A transfer function (TF) characterizes structural dynamics in terms of its load-response (input-output) relationship, and it is known as a frequency response function (FRF) in the frequency domain. A TF or FRF of a railway track structure is an effective representation of its dynamic properties, which is often defined in terms of the load on rails as input and the response of rails or sleepers as output [102~104]. They can be used to identify modal characteristics and stiffness of railway tracks and detect damage in track structures [5~8]. As introduced in Section 1.1, a train-borne LDV can directly measure the vibration of railway tracks under the moving train load, which has the potential to complement existing technologies and support the estimation of railway track TFs from a moving train. No research has been conducted to implement and assess such a technology. The major challenges are summarized below.

- *Obtain dynamic train loads (input) to railway tracks*: Railway tracks are loaded by trains through wheel-rail contact forces, which are broadband in frequency due to irregularities of wheels and tracks. Such loads can be obtained by measurement or estimation. In practice, the instrumentation and calibration of sensors on a vehicle for wheel-rail force measurement are complicated [105, 106]. Since static wheel-rail loads are not a major concern for TF estimation, an alternative solution is to estimate dynamic wheel-rail forces from vehicle vibrations. Many methods have been developed on this topic [107~110], most of which require a vehicle model with known parameters. This may be difficult or expensive to achieve in real life because of changes and degradation of vehicle parameters, such as changes in vehicle body mass due to changes in passenger or good loads and degradation of springs or dampers.

- *Measure dynamic responses (output) of railway tracks*: A train-borne LDV enables noncontact and continuous measurement of track vibrations. As introduced in Section 1.2.1 and 1.2.3, speckle noise in LDV signals must be effectively mitigated at different train speeds to improve their signal-to-noise ratio. Since an LDV measures the relative velocity between the laser spot and the laser head along the laser beam direction, the vibrations of the laser head and other optical components affecting the laser beam need to be compensated to avoid their disturbance to track response measurements.

- *Estimate railway track TFs with moving load and response*: Conventionally, a TF is defined based on load and response at fixed locations. When measuring railway track TFs from a running train, the locations of both load and response move and the input-output relationship varies. Therefore, proper segmentation is needed to divide a continuous railway track structure into distributed sections and estimate an average input-output relationship from measurements on each

track section. Meanwhile, non-parametric methods for estimating a TF from load and response signals have been studied for decades [111~114]. Essentially, they smooth the ratio of the output spectrum to the input spectrum using different strategies, such as windowing and averaging, for the purpose of reducing errors caused by noise, transient, and leakage. Their performance under the disturbance of segmentation and speckle noise remains to be assessed.

1.3. OBJECTIVES

This dissertation aims to address the above challenges that hinder train-borne LDV from measuring the dynamic properties of railway tracks. The objectives corresponding to these challenges are given as follows.

- To develop and validate a post-processing method for reducing speckle noise in LDVom measurements at high speeds.

- To develop and validate an OMA method in time-frequency representation for identifying modal parameters of a structure from its nonstationary vibration response under operational conditions.

- To develop a holistic method based on simulations and measurements for characterizing track vibration measurements with a train-borne LDV and investigate its speed-dependent characteristics.

- To develop and validate a method for estimating dynamic wheel-rail forces and TFs of railway tracks from LDV and accelerometer measurements on a moving vehicle.

1.4. CONTRIBUTIONS

The overall contribution of this dissertation is **the development and validation of a new technology based on train-borne LDV for measuring the vibration and load-response relationship of railway tracks over a wide frequency range**. Figure 1.2 shows the testing of the technology in the TU Delft V-Track test rig, and Figure 1.3 shows such a train-borne LDV system instrumented on the CTO measurement train of TU Delft. This dissertation demonstrates the applicability of the train-borne LDV technology for more efficient and informative rail infrastructure monitoring.

Figure 1.2: LDV on the moving platform of the TU Delft V-Track test rig.

Figure 1.3: Train-borne LDV on the CTO measurement train of TU Delft.

Specifically, the developed technology consists of the following four cornerstones with their validity experimentally proved within a certain scope.

- Based on the characteristics of the speckle noise from LDVom measurements, **a three-step framework for speckle noise reduction** is developed. A wavelet-based spike detection method, an autoregressive integrated moving average-based imputation method, and a Butterworth filter are used at the three steps, respectively. The method is validated in V-Track at speeds up to 20 km/h through comparisons with trackside measurements.

- By extending the FDD method, **an interpretable OMA method in time-frequency representation** is developed. It provides not only a global view of modal characteristics over time and frequency but also estimates of modal parameters. It is applicable to strongly nonstationary responses under time-varying loads and conditions and robust to the length of signals. The method is validated using sleeper vibrations under train passage in V-Track and in the field.

- By combining numerical simulations, laboratory measurements, and field measurements, **a holistic methodology for characterizing train-borne LDV measurements** is developed. Speckle noise is separated from structural vibrations adaptively at different speeds and robustly under different scenarios. The speed-dependent characteristics of sleeper vibration measurements are determined. As sleeper vibrations compete with speckle noise at different speeds, an optimal speed range yields the highest signal-to-noise ratio.

- Based on the above methods, **a methodology for estimating railway track TFs from LDV and accelerometer measurement on a moving vehicle** is developed. OMA of a vehicle passing over joints is combined with contact force estimation from vehicle vibrations, which eliminates the need to define vehicle parameters for wheel-rail force estimation. The proposed method is validated in V-Track at different track locations and speeds (8~16 km/h). The estimated TFs are compared with trackside measurements and hammer tests, and they show good agreement at 200~800 Hz. The differences in the estimated TFs between different track sections reflect the variation of track dynamic properties.

1.5. Dissertation Outline

The structure of this dissertation is shown in Figure 1.4. Chapter 2 presents the development and validation of the speckle noise reduction method, which focuses more on the processing of signals measured by LDV. Chapter 3 presents the development and validation of the operational modal analysis method in time-frequency representation, which focuses more on the interpretation of track vibrations under passing trains. Chapter 4 further combines the understanding of the speckle noise and track vibration to investigate the speed-dependent characteristics of track vibration measurements using a train-borne LDV. Chapter 5 incorporates the knowledge from the previous chapters and presents the development and validation of the TF estimation method from LDV and accelerometer measurements on a moving vehicle.
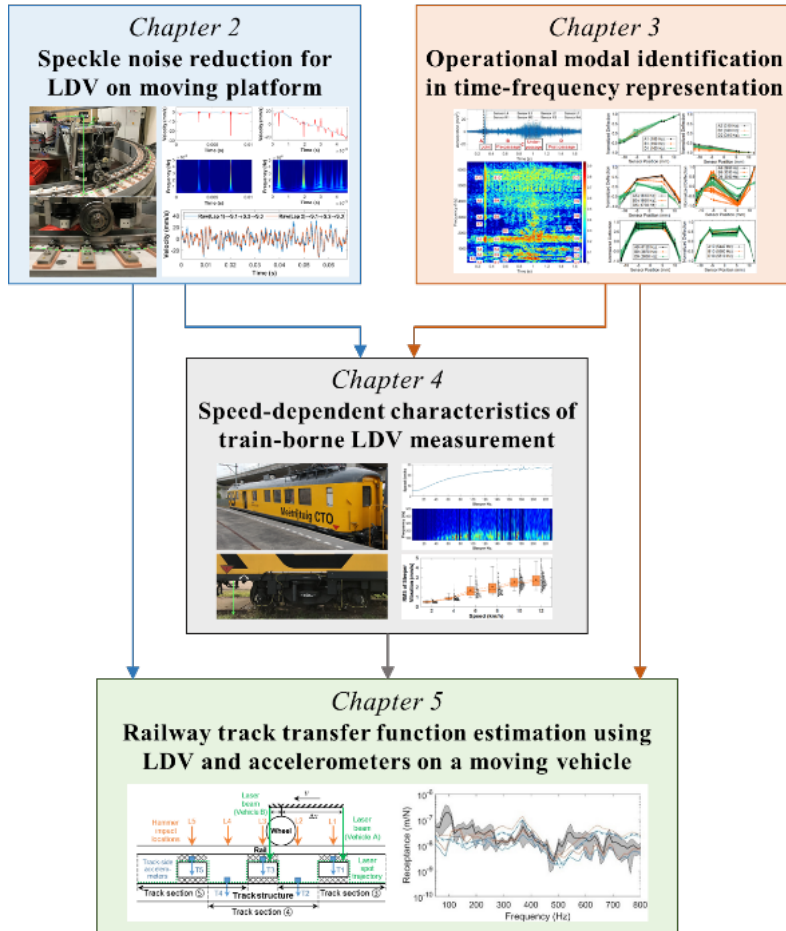

Figure 1.4: Structure of this dissertation.

1

2

SPECKLE NOISE REDUCTION FOR LDV ON MOVING PLATFORM

Speckle noise is a major problem for structural vibration measurements with a laser Doppler vibrometer on moving platform (LDVom) due to its highly random, frequent, and broadband nature, especially at high moving speeds. This chapter develops a new post-processing framework to reduce speckle noise based on a case study of LDVom measurements on railway tracks. First, the characteristics of the speckle noise from LDVom measurements in a vehicle-track test rig are studied. As the speed increases, the speckle noise occurs more frequently, with shorter intervals, shorter durations, larger amplitudes, and broader frequency bands. Then, a three-step despeckle framework is proposed, consisting of spike detection, imputation, and smoothing. This framework works by detecting and replacing spikes, recovering false positives, and smoothing false negatives and residual noise. To showcase this framework, we use a wavelet-based method for Step 1, an autoregressive integrated moving average-based method for Step 2, and a Butterworth filter for Step 3. Besides, the parameter selection strategies and the alternative methods are discussed. Next, the methods are validated through qualitative comparison and quantitative evaluation using a Monte Carlo-based strategy. We demonstrate that the proposed methods effectively reduce the speckle noise at speeds of at least 20 km/h while avoiding the pseudo vibrations. Finally, we show that the LDVom successfully captures the track vibrations at dominant frequencies of 500~700 Hz with good repeatability between different laps and good agreement with trackside measurements.

2.1. Introduction

Speckle noise is problematic for structural vibration measurements with a laser Doppler vibrometer on moving platform (LDVom) at high speeds. Specialized signal processing methods are needed to reduce speckle noise in such challenging situations. This chapter studies the time and frequency characteristics of speckle noise and develops a new post-processing framework for speckle noise reduction. The LDVom measurement in the TU Delft V-Track test rig is used as a case study, and the proposed methods are adaptable to different kinds of structural vibration measurements.

The remainder of this chapter is organized as follows. In Section 2.2, speckle noise samples are collected from LDVom measurements, and their characteristics are investigated. In Section 2.3, a three-step despeckle framework is proposed. To showcase this framework, we develop a wavelet-based spike detection method for Step 1, an autoregressive integrated moving average-based imputation method for Step 2, and a traditional smoothing filter for Step 3. Moreover, the alternative methods at different steps are discussed. In Section 2.4 and Section 2.5, stepwise validation and verification are performed, respectively. Finally, the conclusions are summarized in Section 2.6.

2.2. Characteristics of the Speckle Noise

2.2.1. LDVom measurements in the laboratory

Figure 2.1 shows the experimental setup of LDVom measurements in the V-Track test rig that resembles train-track interaction [115, 116]. The scaled track structure consists of rails, sleepers, and track slabs. Rails are supported by sleepers through fasteners and rail pads, and sleepers are assembled on track slabs through bolts and sleeper pads. The vehicle system consists of an upper mass suspended on a lower mass with a wheel. The suspension provides not only stiffness and damping but also a static vertical load to place the wheel in contact with the rail. The upper mass of the vehicle is connected to a beam, which is driven by a motor to rotate around the central axis of the test rig.
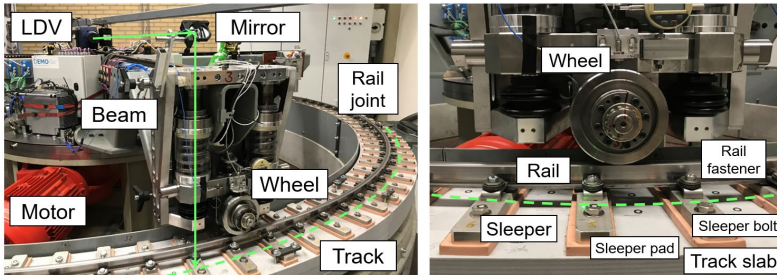
Figure 2.1: LDVom measurement setup in the V-Track test rig. The green arrows represent the laser beam, and the green dashes represent the path of the laser spot.

A one-dimensional LDV (Polytec RSV-150) is mounted on the beam near its rotation axis. A mirror is fixed on the end of the beam to direct the laser onto the track. As the beam rotates, the wheel rolls along the rail, and the laser spot scans along the track structure. This enables the track vibration to be excited by the moving vehicle and then measured by the LDVom. Besides, there are four joints in the test rig connecting

different rail pieces. When the wheel rolls over the joints, impacts occur. This chapter uses the sampling frequency of 102,400 Hz and the static wheel load of 4,000 N.

2.2.2. CHARACTERISTICS IN THE TIME DOMAIN

Gaining insights into the speckle noise is the first step towards reducing it. In the time domain, speckle noise appears as random spikes. First, we manually label more than one thousand spike samples from LDVom measurements at three speeds – 0.5 km/h, 5 km/h, and 20 km/h. This method is reliable when spikes behave differently from genuine vibrations. Figure 2.2 shows a sample of LDVom measurement with seven spikes labeled. We defined three features to characterize the spikes in the time domain – interval, duration, and amplitude. A spike interval is the time difference between two adjacent spikes, denoted as b. A spike duration is the time difference between the boundaries of a spike (e.g., Points A and B), denoted as l. A spike amplitude, denoted as h, is the difference between the local peak or valley of a spike (e.g., Point C) and the average amplitude of its boundaries (e.g., Points A and B). Spike amplitude is positive for a peak whereas negative for a valley.
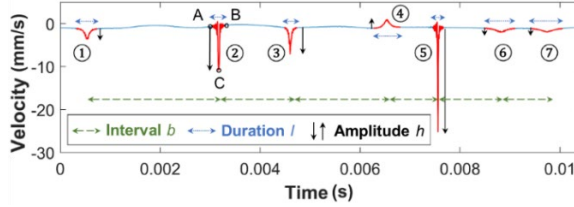
Figure 2.2: A sample of LDVom measurement with labeled spikes (0.5 km/h).
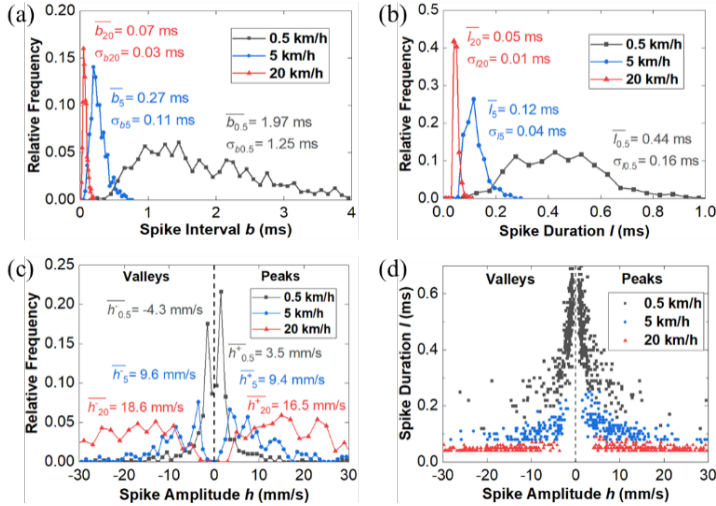
Figure 2.3: Time-domain characteristics of the speckle noise. $\bar{b}_v, \bar{l}_v, \bar{h}_v^+, \bar{h}_v^-$ denote the means of spike intervals, spike durations, peak amplitudes, and valley amplitudes at speed v, respectively; σ_{bv} and σ_{lv} denote the standard deviations of spike intervals and spike durations at speed v, respectively. (a) Distributions of spike intervals; (b) Distributions of spike durations; (c) Distributions of spike amplitudes; (d) Relationship between durations and amplitudes.

The distribution of each feature is estimated based on the relative frequency of its values in consecutive and non-overlapping bins within the total number of samples. As shown in Figure 2.3 (a)~(c), the distributions of spike intervals, durations, and amplitudes at different speeds reflect the randomness of the speckle noise. At higher moving speeds, spikes occur more frequently with shorter durations and larger amplitudes. The amplitude distributions of the peaks are similar to those of the valleys. In addition, the duration of each spike is plotted against its amplitude in Figure 2.3 (d). The hyperbolic shape shows that a spike is more likely to be shorter in duration if it is greater in amplitude and vice versa.

2.2.3. CHARACTERISTICS IN THE FREQUENCY DOMAIN

Considering the discreteness and nonstationarity of the speckle noise, we adopt continuous wavelet transform (CWT) with Morlet wavelet [117] to study its characteristics in the frequency domain. Figure 2.4 shows the spectrograms for the three samples of LDVom signals at different speeds. It shows that spikes are discrete in time and broadband in frequency. As the speed increases, the frequency band is broader since the spike duration is shorter and the spike amplitude is larger. Additionally, the low-frequency parts of a spike may overlap with genuine vibrations or adjacent spikes.
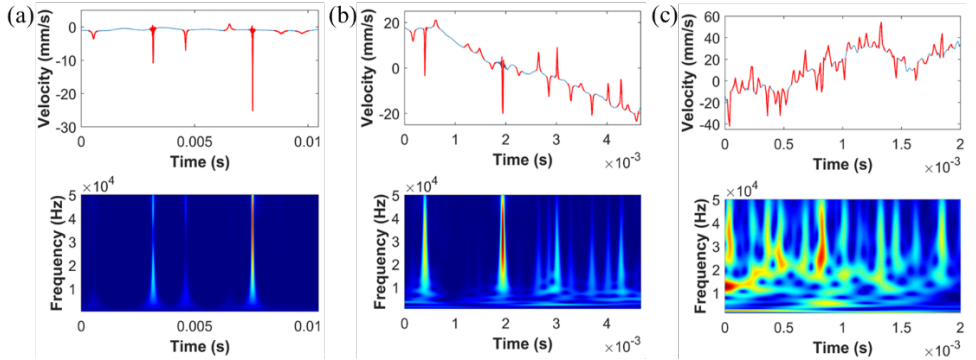
Figure 2.4: Frequency-domain characteristics of the speckle noise. (a) Sample at 0.5 km/h; (b) Sample at 5 km/h; (c) Sample at 20 km/h.

The above characteristics of speckle noise in time and frequency domains account for the limited performance of conventional filters and motivate us to develop new methods for reducing speckle noise (despeckle). The parameter selection in the proposed despeckle methods requires some prior estimates of spike characteristics. Instead of manual spike collection, a fast approach is to directly observe an LDV signal and roughly estimate the features of spikes, e.g., the average spike duration $\bar{l}$ and the minimum spike amplitude $h_{\min}$.

2.3. DESPECKLE METHODOLOGY

When applying conventional methods to despeckle, such as a low-pass filter, both spikes and genuine vibrations are affected, and the amplitude of spikes can be shortened but not eliminated. It is more problematic when speckle noise overlaps with genuine

vibrations in the frequency band of interest, leading to severe residual noise and causing confusion in signal interpretation. Therefore, we propose a new despeckle framework, which consists of three steps:

Step 1. Spike detection: distinguish spikes from genuine vibrations.

Step 2. Imputation: replace spikes based on time series modeling and predictions.

Step 3. Smoothing: filter out residual noise.

The main feature of this framework is that spikes are detected and replaced before being filtered. To showcase how these steps work, we propose a specific method for each of the three steps. Although these methods are used in the case study on railway tracks, they are adaptable to other structural vibration measurements. Moreover, the alternative methods at different steps and their pros and cons are discussed.

2.3.1. STEP 1: SPIKE DETECTION

Step 1 aims to detect spikes in LDV signals based on their characteristics. In this section, we propose a wavelet-based spike detection method.

2.3.1.1. WAVELET DECOMPOSITION AND RECONSTRUCTION

As a tool for processing nonstationary signals, wavelet transform breaks up a signal into shifted and scaled wavelets. The discrete wavelet decomposition (DWT) of a time series u consists of convolving u with two orthogonal filters (a low-pass filter LoF and a high-pass filter HiF) and downsampling the results by two [118], as expressed by the following operator pair,

$$\begin{cases} \mathrm{DWT_A}(u) = (u * LoF) \downarrow 2 \\ \mathrm{DWT_D}(u) = (u * HiF) \downarrow 2 \end{cases} \tag{2.1}$$

where $\mathrm{DWT_A}$ and $\mathrm{DWT_D}$ correspond to the outputs of the low-pass filter and the high-pass filter, respectively, $*$ denotes the convolution operator, and $\downarrow$ denotes the downsampling operator. Based on Eq. (2.1), the DWT of a signal x produces two series of wavelet coefficients,

$$\begin{cases} cA_1 = \mathrm{DWT_A}(x) \\ cD_1 = \mathrm{DWT_D}(x) \end{cases} \tag{2.2}$$

where cA_1 are the approximation coefficients and cD_1 are the detail coefficients [118]. The approximation coefficients can be further decomposed through DWT as follows,

$$\begin{cases} cA_{k+1} = \mathrm{DWT_A}(cA_k) \\ cD_{k+1} = \mathrm{DWT_D}(cA_k) \end{cases} \quad k = 1, 2, \dots \tag{2.3}$$

where cA_k and cD_k are wavelet coefficients at the k-th level. Based on Eq. (2.3), DWT can be performed in a cascading process. The black paths in Figure 2.5 indicate the process of cascading DWT applied to a signal x.
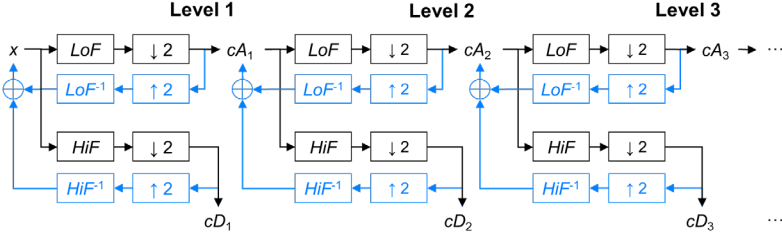
Figure 2.5: Block diagram of cascading DWT (black paths) and IDWT (blue paths).

Reversely, inverse discrete wavelet transform (IDWT) represents the inverse process of DWT [118], and the corresponding operator pair is,

$$\begin{cases} \text{IDWT}_A(u) = \big((u)\uparrow 2\big) * LoF^{-1} \\ \text{IDWT}_D(u) = \big((u)\uparrow 2\big) * HiF^{-1} \end{cases} \tag{2.4}$$

where LoF^{-1} and HiF^{-1} are the inverse filters of LoF and HiF, respectively, and $\uparrow$ denotes the upsampling operator. The signal x and its approximation coefficients cA_k at any level can be reconstructed from the IDWT of wavelet coefficients at the next level, as expressed below.

$$\begin{cases} x = \text{IDWT}_A(cA_1) + \text{IDWT}_D(cD_1) \\ cA_k = \text{IDWT}_A(cA_{k+1}) + \text{IDWT}_D(cD_{k+1}) \quad k = 1,2,... \end{cases} \tag{2.5}$$

The cascading reconstruction process of x is shown by the blue paths in Figure 2.5. Therefore, when the signal x is decomposed to the n-th level ($n>1$), it can be exactly reconstructed as follows.

$$x = R_n(cA_n) + \sum_{k=1}^{n} R_k(cD_k) \tag{2.6}$$

where $R_n(cA_n)$ is the n-step reconstruction of cA_n and $R_k(cD_k)$ is the k-step reconstruction of cD_k:

$$\begin{cases} R_n(cA_n) = \text{IDWT}_A^{\,n}(cA_n) \\ R_1(cD_1) = \text{IDWT}_D(cD_1) \\ R_k(cD_k) = \text{IDWT}_A^{\,k-1}\big[\text{IDWT}_D(cD_k)\big] \quad k = 2,....,n \end{cases} \tag{2.7}$$

where $\text{IDWT}^k(\cdot)$ represents repeating IDWT k times. Eq. (2.6) shows that a signal can be represented as the superposition of a term related to approximation coefficients and n terms related to detail coefficients, describing the deterministic component and the noise, respectively.

2.3.1.2. WAVELET-BASED SPIKE DETECTION

Detail coefficients are sensitive to nonsmooth features in a signal, e.g., jumps and spikes, and have been used to detect spikes or outliers [49, 119~121]. Instead of directly using detail coefficients, we propose a new method as follows.

Step A1. Perform n-level DWT of a signal x according to Eq. (2.2) and (2. 3) to obtain a series of detail coefficients cD_1, cD_2, …, cD_n.

Step A2. Perform k-step reconstruction of cD_k ($k=1$, …, n) according to Eq. (2.7) to obtain a series of reconstructed signals $R_1(cD_1)$, $R_2(cD_2)$, …, $R_n(cD_n)$.

Step A3. Calculate a spike indicator based on the reconstructed signals $R_k(cD_k)$ as follows.

$$R_{\mathrm{D}} = \sum_{k=1}^{n} \left| R_k\left(cD_k\right) \right| \qquad (2.8)$$

Step A4. Label the locations at which R_D is greater than a threshold T_1 as spikes.

Using the reconstructed signals $R_k(cD_k)$ to indicate spikes has the following advantages over using the detail coefficients cD_k.

- The detail coefficients are scaling factors of DWT, so detecting spikes based on them requires some prior estimates or assumptions, e.g., in [119, 120]. In contrast, the reconstructed signals directly represent the amplitude of the noise in a signal.

- Each level of DWT reduces the size of the detail coefficients by half, which needs to be handled when labeling spikes, e.g., in [119, 120]. In contrast, the reconstructed signals are of the same length as the original signal and do not require special treatment.

2.3.1.3. PARAMETER SELECTION

There are three important parameters to select in the proposed method.

Wavelet type. Haar wavelet is recommended because it has shown effectiveness in producing large detail coefficients at locations of outliers [119, 120].

Decomposition level n. It determines the depth to which the noise is decomposed. As n increases, the spike indicator R_D increases, getting closer to the spike amplitude, but the temporal resolution of $R_n(cD_n)$ deteriorates. Therefore, we recommend using n that meets the following criterion so that the resolution of $R_n(cD_n)$ is sufficiently higher compared to the average spike duration.

$$n \ll \log_2\left(\bar{l} \cdot f_{\mathrm{s}}\right) \qquad (2.9)$$

where $\bar{l}$ is a rough estimate of the average spike duration, and f_s is the sampling frequency.

Threshold T_1. It can be selected based on the cumulative frequency distribution of R_D above different values, denoted as $P(R_D>R)$. Ideally, as R increases from 0 to infinity, $P(R_D>R)$ decreases from 1 to 0, first sharply and then slowly. The critical point is a good balance between fewer false positives (genuine vibrations are labeled as spikes) and fewer false negatives (spikes are missed), so the value of the critical point can be selected as the threshold T_1. In the absence of a significant critical point

(usually when speckle noise occurs very frequently), T_1 can be set to a value providing a reasonable proportion of labeled points, e.g., $P(R_D > T_1) \approx 0.5$. This leaves some small-amplitude spikes unlabeled to reduce the amount of imputation in Step 2, and these false negatives can be reduced in Step 3.

2.3.2. Step 2: Imputation

Step 2 aims to replace the detected spikes with estimates based on nearby unlabeled points. This process is known as imputation and is commonly used to handle missing data or outliers [122, 123]. Generally, missing points or outliers occur occasionally [124, 125], whereas, in our case, spikes occur more frequently, especially at high speeds. Meanwhile, false positives may occur during spike detection, i.e., genuine vibrations are labeled as spikes, and their original values should not be discarded.

The basic idea of imputation is to build a time series model and make predictions at locations labeled as spikes. A widely-used time series model is the autoregressive integrated moving average (ARIMA) model. For example, in [124], an ARIMA model with exogenous inputs is used for outlier imputation, and in [126], a seasonal ARIMA model is used for missing data imputation. In this section, we use a non-seasonal ARIMA model because the LDVom measurements on large-scale structures do not follow a seasonal pattern.

2.3.2.1. Training and replacement with an ARIMA model

A non-seasonal ARIMA model is defined as a three-tuple ARIMA(p, d, q). The autoregressive order p defines the number of past points used to regress the evolving point. The differencing order d defines the times of differencing applied to the original series. The moving average order q defines the number of past regression errors used to regress the evolving error. The ARIMA model for a time series x_t indexed by t is [127],

$$\left(1 - \sum_{i=1}^{p} \alpha_i L^i \right)(1 - L)^d x_t = \left(1 + \sum_{j=1}^{q} \theta_j L^j \right)\varepsilon_t \tag{2.10}$$

where ε_t is the regression error indexed by t, α_i is the coefficient for the i-th autoregressive term ($i=1, \ldots, p$), θ_j is the coefficient for the j-th moving average term ($j=1, \ldots, q$), L^i is the i-step lag operator, and $(1-L)^d$ represents the d-th order differencing.

The regression coefficients of an ARIMA model with defined orders can be estimated based on a time series from measurements, named the training process. Considering the presence of speckle noise, we list three training strategies in Table 2.1, including their advantages and disadvantages.

A trained ARIMA model can predict the values of the future points $\hat{x}_{t+1}$, ..., $\hat{x}_{t+s}$ based on the past points $x_{t-p-d+1}$, ..., x_t through differencing, forecasting, and reversing. For example, the process of one-step ($s=1$) prediction in the case of $d=1$ is as follows.

$$\begin{cases} y_t = x_t - Lx_t \\ \hat{y}_{t+1} = \sum_{i=0}^{p-1} \alpha_{i+1} L^i y_t + \sum_{j=0}^{q-1} \theta_{j+1} L^j \varepsilon_t \\ \hat{x}_{t+1} = \hat{y}_{t+1} + x_t \end{cases} \tag{2.11}$$

Table 2.1: Different training strategies for imputation.

Strategies	Descriptions	Advantages	Disadvantages
Direct training	• Train the model using all data points, including spikes, through a traditional method, e.g., the Box-Jenkins method [127].	• The most straightforward.	• The participation of spikes may skew the regression coefficients of the model [124].
Training with unlabeled points	• Train the model using only unlabeled data through the methods in [128, 129].	• Only genuine vibrations (except false negatives) are used for training.	• Loss of information in case of false positives. • Problematic when speckle noise affects most parts of the signal.
Training after manipulation [124, 130]	• Replace the detected spikes with local means or other statistics. • Train the model using the manipulated signal through a traditional method.	• Maintain the data size for training. • Reduce the disturbance of spikes.	• Manipulation may induce extra dynamics or eliminate important dynamics.

As mentioned above, false positives may exist in the time series after spike detection. To reduce the influence of imputation on false positives, we apply the following replacement strategy after making predictions at the locations of labeled points.

$$x^r_t = \begin{cases} \hat{x}_t & \text{if } |\hat{x}_t - x_t| \geq \lambda \cdot h_{\min} \\ x_t & \text{if } |\hat{x}_t - x_t| < \lambda \cdot h_{\min} \end{cases} \tag{2.12}$$

where x_t is the original value, $\hat{x}_t$ is the predicted value, λ is a scaling factor, $h_{\min}$ is a rough estimate of the minimum spike amplitude, and x^r_t is the point after replacement. This strategy detects a false positive and trusts its original value when the difference between the predicted and original values is sufficiently small.

2.3.2.2. Multi-offset and bi-directional imputation

Based on the above fundamentals, we propose the following steps of bi-directional training and replacement to involve data points on both sides of a spike in the imputation process.

Step B1. Train a time series model along the forward direction using a strategy in Table 2.1.

Step B2. Make predictions for each segment of labeled points along the forward direction and make replacements according to Eq. (2.12). Use the replaced segments for future predictions.

Step B3. Perform Step B1 and B2 along the backward direction.

Step B4. Average the forward and backward replacement results.

Based on the bi-directional training and replacement process, we further propose a multi-offset imputation method, as shown in Figure 2.6. The major steps are as follows.

Step C1. Pad the original signal on both ends with $d+p$ points that are equal to the first and the last points, respectively.

Step C2. Downsample the padded signal by a factor of r.

Step C3. For each downsampled signal with a certain offset, perform bi-directional training and replacement (Step B1~B4) to produce an imputation result.

Step C4. Upsample each imputation result by the factor of r through interpolation and average all the imputation results with different offsets.
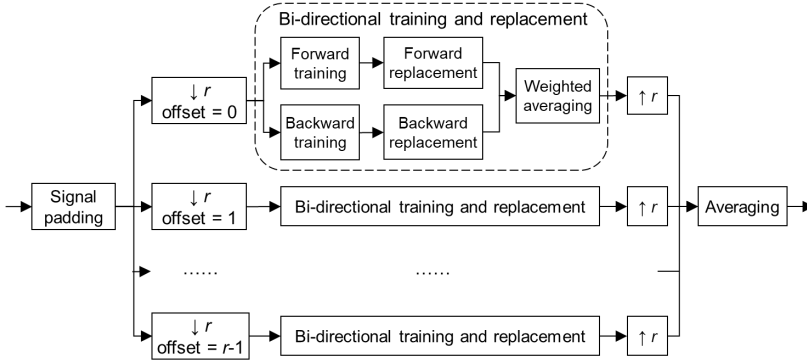

Figure 2.6: Flowchart of multi-offset imputation with bi-directional training and replacement.

Padding the signal in Step B1 allows the imputation process to cover the entire signal. Downsampling in Step B2 reduces the model order. Using downsampled signals with different offsets in Step B3 and B4 can improve the imputation accuracy. Additionally, the proposed imputation method is applicable not only to ARIMA models but also to other time series models.

2.3.2.3. Parameter selection

There are several parameters to select in the proposed imputation method. First, the ARIMA model orders (d, p, q) need to be selected depending on the choice of the training strategy. For training with unlabeled data or after manipulation, spikes are excluded, so the model orders can be selected through traditional methods, e.g., the autocorrelation function (ACF)-based method [127] and the Akaike information criterion [131]. For the direct training strategy, selecting the model orders is tricky due to the involvement of spikes in regression. We propose the following strategy to deal with this situation.

Differencing order d. Appropriate differencing is necessary to treat the nonstationarity caused by spikes. A good choice of d should provide a differenced time series with an ACF that rapidly decays with respect to the lag [127]. Therefore, we recommend increasing d from 1 until the ACF meets this criterion.

Moving average order q. Since the ACF usually turns from positive to negative after differencing, an appropriate q is needed. Meanwhile, q should not be too large so as to limit the influence of regression errors due to spikes, e.g., $q=1$ can be sufficient.

Autoregressive order p. It should be selected properly to capture the dynamics of genuine vibrations. We recommend initially setting p based on the average spike duration $\bar{l}$ as follows and then adjusting it by evaluating the imputation performance.

$$p = \frac{\bar{l} \cdot f_s}{r} \tag{2.13}$$

Downsampling is recommended in Step B2 when the sampling frequency f_s is high enough. According to Eq. (2.13), a larger downsampling factor r can reduce the autoregressive order p of the ARIMA model, thereby reducing the computational cost. Meanwhile, the integer r should be restricted so that f_s/r is sufficiently higher than the highest frequency of interest.

The scaling factor λ in Eq. (2.12) determines the boundary between trusting the original point and the predicted value. It should be set to a small value, e.g., at least below 0.2, so that false positives are recovered but not real spikes. In this case, the imputation performance is not sensitive to λ, since only predicted points with small deviations from the original points are affected.

Finally, for each segment of labeled points, we recommend predicting additional c points ahead in both directions in Step B2 and calculating the weighted average of the bi-directional results in Step B4 based on the following weighting functions.

$$w_f(x) = \begin{cases} \dfrac{-2|e_f|}{|e_f|+|e_b|}\dfrac{x}{l}+1 & 0 \le x < \dfrac{l}{2} \\ \dfrac{-2|e_b|}{|e_f|+|e_b|}\left(\dfrac{x}{l}-1\right) & \dfrac{l}{2} \le x \le l \end{cases} \quad w_b(x) = \begin{cases} \dfrac{2|e_f|}{|e_f|+|e_b|}\dfrac{x}{l} & 0 \le x < \dfrac{l}{2} \\ \dfrac{2|e_b|}{|e_f|+|e_b|}\dfrac{x}{l}+\dfrac{|e_f|-|e_b|}{|e_f|+|e_b|} & \dfrac{l}{2} \le x \le l \end{cases} \tag{2.14}$$

where l is the length of labeled points, $w_f(x)$ (or $w_b(x)$) is the weight for the forward (or backward) replacement result at position x, and e_f (or e_b) is the forward (or backward) terminal error, i.e., the average prediction error for the additional c points. The parameter c can be set to a small integer, such as 3~5. The above averaging strategy is illustrated in Figure 2.7, in which both the distance to the boundary and the terminal error contribute to the determination of weights. The following properties hold for the weighting functions in Eq. (2.14).

- $w_f(x)+w_b(x)=1$; $w_f(0)=1$; $w_b(l)=1$.

- $w_f(x)$ is a decreasing function of x, and $w_b(x)$ is an increasing function of x.

- If $|e_f|/|e_b|$ decreases, $w_f(x)$ will increase and $w_b(x)$ will decrease, and vice versa.

- At the midpoint ($x=l/2$), the weights depend only on the terminal errors:

$$w_f\left(\frac{l}{2}\right) = \frac{|e_b|}{|e_f|+|e_b|} \quad w_b\left(\frac{l}{2}\right) = \frac{|e_f|}{|e_f|+|e_b|} \tag{2.15}$$
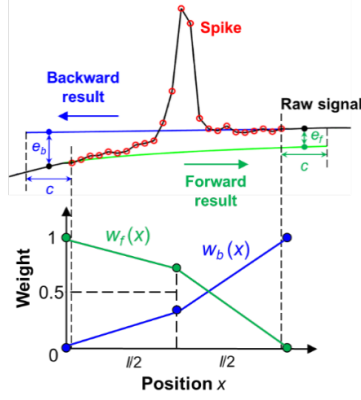
Figure 2.7: Weighting functions.

2.3.3. STEP 3: SMOOTHING

The signal processed after Step 1 and Step 2 may still contain undesired noise, such as false negatives in spike detection that remain untreated, errors induced in the imputation process, and abrupt changes due to switching between the two options in Eq. (2.12).

Step 3 aims to reduce the residual noise while preserving the genuine vibration. It is implemented by applying a classical smoothing or denoising method because the residual noise is no longer as broadband as the raw speckle noise. In this chapter, we use a low-pass filter. The gain of an m-order low-pass Butterworth filter is [132]:

$$G^2(\omega) = \frac{G_0^{\ 2}}{1 + \left(\dfrac{j\omega}{j\omega_c}\right)^{2m}} \tag{2.16}$$

where G_0 is the gain at zero frequency and ω_c is the cut-off frequency. The amplitude-frequency response of a Butterworth filter is monotonic, being maximally flat in the passband while rolling off toward zero in the stopband [133]. The cut-off frequency can be set equal to the highest frequency of interest.

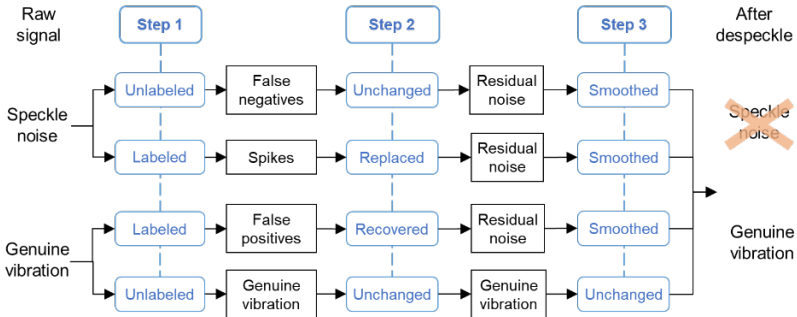### 2.3.4. DIFFERENT OPTIONS AT DIFFERENT STEPS

Figure 2.8: Signal flow in the three-step despeckle framework.

Figure 2.8 illustrates the signal flow in the proposed despeckle framework. Spikes are detected in Step 1 and replaced in Step 2. False positives are recovered in Step 2. False negatives and residual noise are smoothed in Step 3.

Table 2.2: Different options in Step 1 (Spike detection).

Methods	Descriptions	Advantages	Disadvantages
Wavelet-based (Section 2.3.1)	• Calculate a spike indicator through wavelet decomposition and reconstruction.	• The spike indicator reflects the noise amplitude.	• Require multi-level DWT and IDWT.
Wavelet-based [49, 119, 120]	• Calculate the detail coefficients through wavelet decomposition.	• No IDWT required.	• Thresholding requires prior estimates or assumptions. • Size reduction due to downsampling.
High-pass filter-based [49]	• Filter the raw signal with a high-pass filter.	• Easy to implement in frequency domain.	• Frequency-dependent time delay.
Local statistics-based [34, 37, 53]	• Calculate the local variance/kurtosis in a sliding window.	• Easy to implement in time domain.	• Spike boundaries are difficult to determine.
Short-time energy-based [37]	• Calculate the average short-time energy in a sliding window.	• Sensitive to spikes of long duration.	• Spike boundaries are difficult to determine.
Residual-based [124]	• Build a time series model for the raw signal. • Calculate residuals to indicate outliers.	• Independent of frequency characteristics.	• Outliers degrade the regression performance.

Table 2.3: Different options in Step 2 (Imputation).

Methods	Descriptions	Advantages	Disadvantages
ARIMA-based (Section 2.3.2)	• Model the time series by ARIMA models. • Replace spikes through multi-offset and bi-directional imputation.	• Fitting an ARIMA model is deterministic and fast.	• Only linear dynamics is captured. • Spikes degrade the training performance.
ARIMA-based [124]	• Outliers are replaced by local means. • Model the manipulated time series by an ARIMA model and make predictions.	• Fitting an ARIMA model is deterministic and fast. • The disturbance of outliers is reduced.	• Only linear dynamics is captured. • Manipulation may induce extra dynamics or eliminate important dynamics.

Linear prediction-based [37, 53]	• Model the time series by a linear prediction model. • Replace spikes through linear prediction.	• Fitting a linear prediction model is fast.	• Only linear dynamics is captured.
Support vector machine (SVM)-based [130]	• Replace outliers or missing values with temporal information. • Model the time series by an SVM and make predictions.	• Capture nonlinear dynamics by a kernel method. • The disturbance of outliers is reduced.	• Non-explicit interpretability. • Manipulation may induce extra dynamics or eliminate important dynamics.
Artificial neural network (ANN)-based [134]	• Model the time series by an ANN and make predictions. • Optimization is usually required to improve accuracy.	• Capture nonlinear dynamics.	• Computationally demanding. • Non-explicit interpretability.
Kalman filter-based [125, 135]	• Model the signal by a Kalman filter and make predictions.	• Capture dynamic trends.	• Sensitive to model design.
Interpolation-based [49, 136]	• Interpolate based on adjacent points.	• No modeling required.	• Difficult to capture dynamic behaviors.

Table 2.4: Different options in Step 3 (Smoothing).

Methods	Descriptions	Advantages	Disadvantages
Low/band-pass filter (Section 2.3.3)	• Filter the signal with a low/band-pass filter.	• Clear physical meaning. • Preserve genuine vibrations.	• Sensitive to the cut-off frequency. • Frequency-dependent time delay.
Mean filter [137]	• Calculate the weighted average in a sliding window.	• Easy to implement in time domain.	• Reduce genuine vibrations. • Sensitive to window design.
Median filter [138, 139]	• Calculate the local median in a sliding window.	• Easy to implement in time domain.	• Reduce genuine vibrations. • Sensitive to window design.
Lee filter [140]	• Calculate local statistics in a sliding window.	• Balance between original values and local statistics.	• Reduce genuine vibrations. • Sensitive to window design.
Sigma filter [141]	• Calculate the local mean within a certain deviation.	• Exclude outliers. • Easy to implement in time domain.	• Reduce genuine vibrations.
Wavelet denoise [62, 142, 143]	• Perform wavelet transform. • Filter out large wavelet coefficients. • Reconstruct the signal.	• Suitable for nonstationary changes.	• Sensitive to wavelet type and decomposition level.

In the proposed despeckle framework, we use a wavelet-based method for Step 1, an ARIMA-based method for Step 2, and a Butterworth filter for Step 3. A significant advantage of the proposed framework is that other different methods can also be adapted and used at different steps. Table 2.2~2.4 lists some other alternative methods from our literature survey, including some post-processing methods mentioned in Section 1.2.1. These tables are intended to provide some potential options for each step and discuss their pros and cons.

2.4. STEPWISE VALIDATION

In this section, the proposed despeckle framework is validated following a stepwise process.

2.4.1. VALIDATION OF STEP 1

Taking the signal in Figure 2.4 (a) as an example, we show the reconstructed signal $R_k(cD_k)$ at different level k in Figure 2.9 (a), where as k increases, the temporal resolution of $R_k(cD_k)$ deteriorates, while its size remains the same as the original signal. Further, we show the spike indicator R_D for different n in Figure 2.9 (b), where as n increases, R_D gets larger at the locations of spikes, and the amplitude of R_D is correlated with the corresponding spike amplitude.

According to Eq. (2.9), the decomposition level of $n=3$ is selected. Then, the cumulative frequency distribution of R_D is plotted in Figure 2.10 (0.5 km/h). A critical point can be observed, so the threshold of $T_1=0.1$ mm/s is selected. The corresponding detection result in Figure 2.9 (c) shows that all the manually selected spikes in Figure 2.4 (a) are automatically detected.
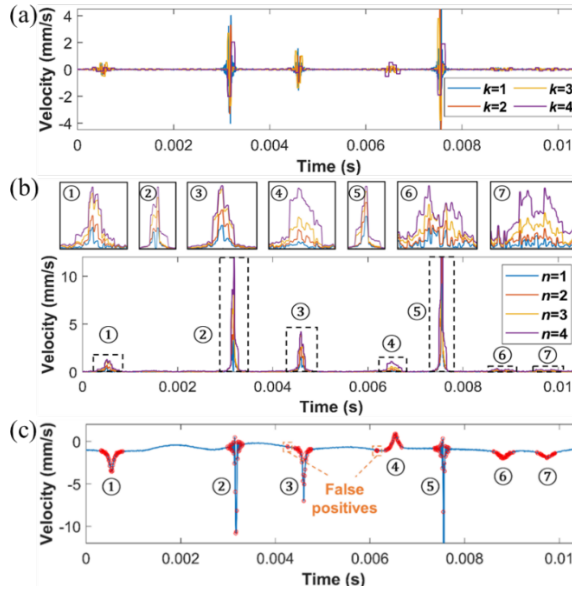

Figure 2.9: Wavelet-based spike detection at 0.5 km/h. (a) Reconstructed signal $R_k(cD_k)$ at different k; (b) Spike indicators R_D for different n; (c) Spike detection result.
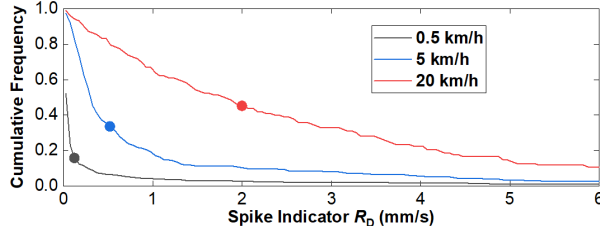
Figure 2.10: Cumulative frequency of spike indicators R_D at different speeds.
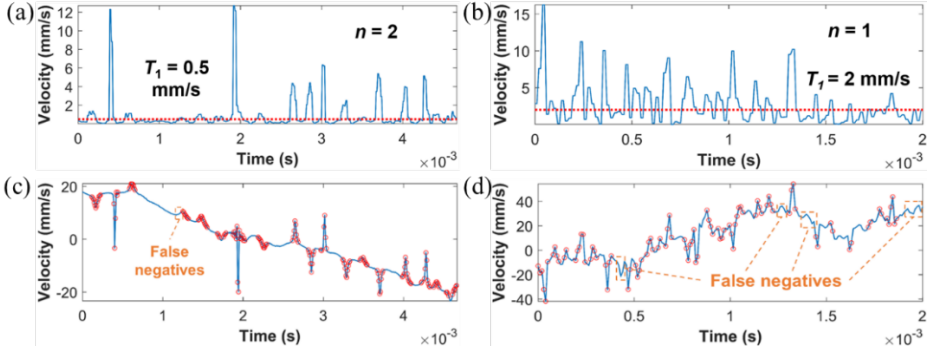

Figure 2.11: Wavelet-based spike detection at 5 km/h and 20 km/h. (a) Spike indicator R_D at 5 km/h; (b) Spike indicator R_D at 20 km/h; (c) Spike detection result at 5 km/h; (d) Spike detection result at 20 km/h.

Similarly, Figure 2.10 and 2.11 show the spike detection results for the two samples in Figure 2.4 (b) and (c), respectively. For the higher speeds, the selected n is smaller due to the shorter spike duration, and the selected T_1 is larger due to the larger spike amplitude. It is noteworthy that in Figure 2.10 no critical point is observed at 20 km/h, so we select $T_1=2$ mm/s to label approximately half of the points as spikes. Compared with the manual selection in Figure 2.4, most of the spikes are detected. Meanwhile, some false negatives can be observed, e.g., the points labeled in Figure 2.9 (c) and Figure 2.11 (c) and (d). They will be addressed through the replacement strategy in Step 2 and the smoothing method in Step 3, respectively.

2.4.2. VALIDATION OF STEP 2

In our case study, we use the strategy of direct training in Table 2.1 for imputation. To showcase the design of ARIMA models following Section 2.3.2.3, we take the above three samples as examples and show their ACFs at different differencing orders d in Figure 2.12. The plots for $d=0$ show slow-decay patterns, the plots for $d=1$ show rapid-decay patterns, and the plots for $d=2$ indicate over-differencing. Meanwhile, the ACFs turn from positive to negative after differencing. Therefore, we select $d=1$ and $q=1$ for all the three samples.

Since speckle noise masks genuine vibrations in real signals, we propose a Monte Carlo-based strategy to create artificial noisy signals by superposing the collected spike samples with base signals free of speckle noise (from non-LDV measurements or simulations). At each time instant of a base signal, a random number between 0 and 1 is generated. Once it is smaller than a defined scalar p_s, a spike sample is randomly selected,

and its amplitude is scaled by a factor a_s. Then, the left and right halves of the spike sample are scaled separately and superposed with the base signal with smooth transitions. Afterward, imputation is performed for the artificial signal at the locations of spikes, and the imputation error is quantified through comparisons with the base signal, as shown in Figure 2.13. Additionally, the spike occurrence rate and amplitude are adjustable by changing p_s and a_s, respectively, which allows us to evaluate the imputation accuracy under different speckle noise severity.

2
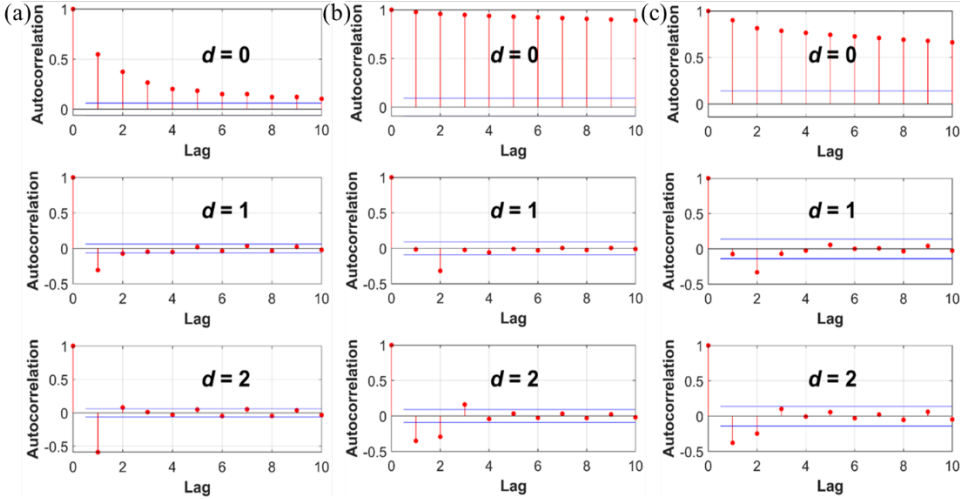
Figure 2.12: ACF plots for different d. (a) 0.5 km/h; (b) 5 km/h; (c) 20 km/h.
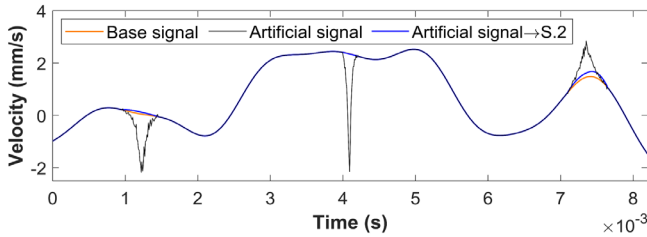
Figure 2.13: An imputation example based on an artificial signal. 'Artificial signal→S.2' represents applying Step 2 alone to the artificial signal.

Following the above strategy, three artificial signals with different speckle noise severity are generated. Table 2.5 and 2.6 compare the imputation performance between different ARIMA model orders, including the mean square error (MSE) at all spike locations and the total CPU time (on Intel Xeon E5-2643 @3.30 GHz). The influence of p is small in a certain range ($p=20\sim50$) but becomes significant when it is too large or too small. It shows that the combination of $d=1$, $q=1$, and $p=40$ outperforms the other choices in terms of imputation errors, demonstrating the effectiveness of the model order selection strategy in Section 2.3.2.3.

2

Table 2.5: Imputation performance under different d and q.

ARIMA models			Artificial signal 1 $p_s=0.002$, $a_s=1$		Artificial signal 2 $p_s=0.004$, $a_s=1$		Artificial signal 3 $p_s=0.004$, $a_s=2$	
p	d	q	MSE (mm/s)	CPU time (s)	MSE (mm/s)	CPU time (s)	MSE (mm/s)	CPU time (s)
$p=40$ (acc. to Eq. (2.13))	$d=0$	$q=1$ (acc. to Figure 2.12)	0.010537	81.843	0.004112	79.97	0.004225	79.11
	$d=2$		0.002198	101.84	0.002133	110.41	0.001667	107.94
	$d=1$ (acc. to Figure 2.12)		0.001373	88.67	0.001571	88.03	0.001240	89.08
		$q=0$	0.004033	72.11	0.003596	103.88	0.004343	60.44
		$q=2$	0.001390	89.31	0.001572	97.27	0.001336	91.16

Table 2.6: Imputation performance under different p.

ARIMA models			Artificial signal 1		Artificial signal 2		Artificial signal 3	
p	d	q	MSE (mm/s)	CPU time (s)	MSE (mm/s)	CPU time (s)	MSE (mm/s)	CPU time (s)
$p=0$	$d=1$ (acc. to Figure 2.12)	$q=1$ (acc. to Figure 2.12)	0.002581	3.23	0.002187	6.52	0.002065	5.36
$p=5$			0.002699	8.03	0.002145	11.05	0.001886	9.95
$p=10$			0.002812	11.45	0.002128	16.11	0.001846	16.80
$p=20$			0.001257	35.11	0.002136	33.69	0.001748	34.73
$p=30$			0.001297	52.27	0.002056	55.27	0.001579	56.39
$p=40$ (Eq. (2.13))			0.001373	88.67	0.001571	88.03	0.001240	89.08
$p=50$			0.002009	114.97	0.001636	130.31	0.001278	118.16
$p=60$			0.004671	148.22	0.002460	155.94	0.004929	160.08
$p=70$			0.004438	265.78	0.003492	289.16	0.004598	287.84

Table 2.7: Imputation performance under different downsampling strategies.

Downsampling strategies			Artificial signal 1		Artificial signal 2		Artificial signal 3	
r	p	Offset	MSE (mm/s)	CPU time (s)	MSE (mm/s)	CPU time (s)	MSE (mm/s)	CPU time (s)
$r=1$	$p=40$	/	0.001373	88.67	0.001571	88.03	0.001240	89.08
$r=2$	$p=20$	Single offset	0.001434	24.80	0.001656	29.90	0.001593	28.90
		Multiple offsets	0.001429	49.59	0.001643	59.80	0.001243	57.80
$r=3$	$p=20$	Single offset	0.001425	15.23	0.001672	18.51	0.001359	17.70
		Multiple offsets	0.001423	45.69	0.001657	55.53	0.001347	53.11

Table 2.8: MSE (mm/s) under different averaging strategies.

Averaging strategies	Artificial signal 1	Artificial signal 2	Artificial signal 3
Only forward replacement	0.006353	0.005300	0.005774
Only backward replacement	0.005937	0.005342	0.005797
Direct average	0.003723	0.003276	0.003307
Weighted average (Section 2.3.2.3)	0.001373	0.001571	0.001240

Table 2.7 compares the imputation performance under different downsampling strategies, in which p is adjusted with respect to the downsampling factor r according to Eq. (2.13). A higher r significantly reduces the computational cost, and averaging the imputation results from multiple offsets slightly improves the imputation accuracy over using only one offset.

Table 2.8 compares the imputation accuracy under different averaging strategies in the bi-directional training and replacement process. Compared to the other strategies, the proposed weighted averaging strategy reduces the imputation error significantly.

2.4.3. VALIDATION OF STEP 3

In this section, we use real signals to validate the despeckle framework. First, three samples measured at 0.5 km/h are shown in Figure 2.14. For each sample, the upper plot compares the raw signal with the product of the first two steps, while the lower plot compares the final despeckle outcome with the result of applying the filter in Step 3 alone to the raw signal. We adopt a low-pass filter with ω_c=3 kHz in Step 3, considering the track vibration is generally below 3 kHz. It shows that the speckle noise is effectively eliminated by detecting and replacing the spikes, whereas the direct use of the low-pass filter leaves significant residual noise because the speckle noise at 0.5 km/h contains components below 3 kHz, as shown in Figure 2.4 (a).

Similarly, Figure 2.15 shows three despeckle samples at 5 km/h. Compared to Figure 2.14, the residual noise after direct filtering becomes lighter since the speckle noise at 5 km/h has a higher frequency band, according to Figure 2.4 (b). However, as the sharpness of spikes is reduced, the residual noise looks more like vibrations. This pseudo vibration is not a real structural response but the low-frequency part of the speckle noise due to insufficient despeckle. The proposed three-step framework can effectively avoid this problem.

The despeckle performance for signals measured at 20 km/h is shown in Figure 2.16. Since the speckle noise affects most parts of the signals, the despeckle framework allows some false negatives (small-amplitude spikes) in Step 1 so as to reduce the amount of imputation in Step 2. Then, the residual noise is filtered out in Step 3. In this way, the proposed three-step framework effectively reduces speckle noise while avoiding pseudo vibrations.
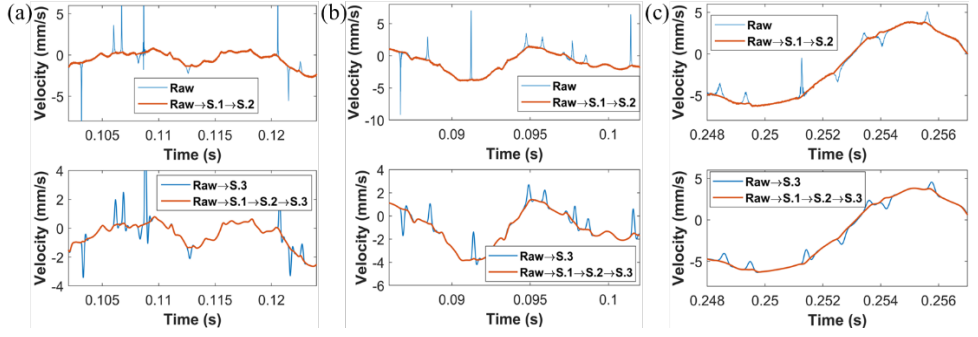
Figure 2.14: Despeckle samples at 0.5 km/h. 'Raw' represents the raw signal, 'Raw→S.1→S.2' represents the product of the first two steps, 'Raw→S.1→S.2→S.3' represents the final despeckle outcome, 'Raw→ S.3' represents applying Step 3 alone to the raw signal. (a) Sample L1; (b) Sample L2; (c) Sample L3.
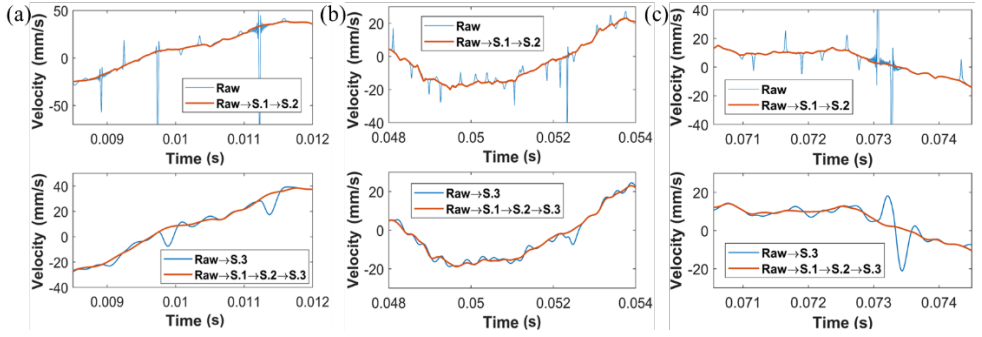
Figure 2.15: Despeckle samples at 5 km/h. (a) Sample M1; (b) Sample M2; (c) Sample M3.
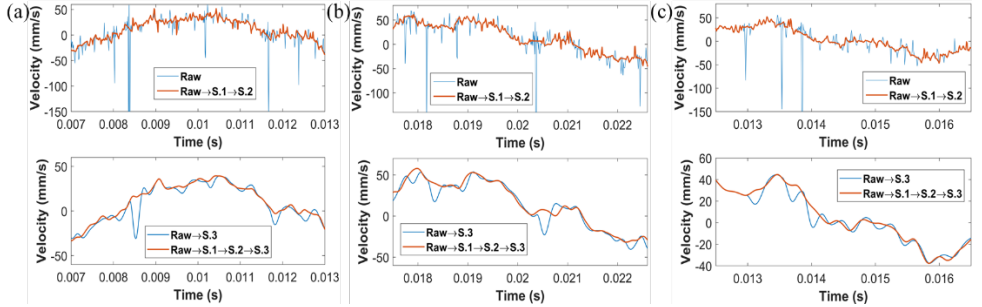
Figure 2.16: Despeckle samples at 20 km/h. (a) Sample H1; (b) Sample H2; (c) Sample H3.

2.5. Comparison with Trackside Measurements

To verify the LDVom measurements, we mount two accelerometers (PCB 356B21) near the laser spot trajectory on one sleeper and one segment of the track slab, as shown in Figure 2.17. The trackside measurements are performed under the same conditions as the LDVom measurements. Among the different speeds, we only analyze 20 km/h because a higher speed is desired for more efficient monitoring and the speckle noise is

more severe. Besides, to enable comparisons in the same unit, we convert accelerations to velocities through frequency-domain integration [144].

Figure 2.17: Setup of trackside vibration measurements.

First, the track vibration excited by passing the joint in Segment A is analyzed. Figure 2.18 (a) shows the raw LDVom signals at two laps (rotations of the beam), and the upper plot in Figure 2.18 (b) shows the corresponding despeckle results using the prop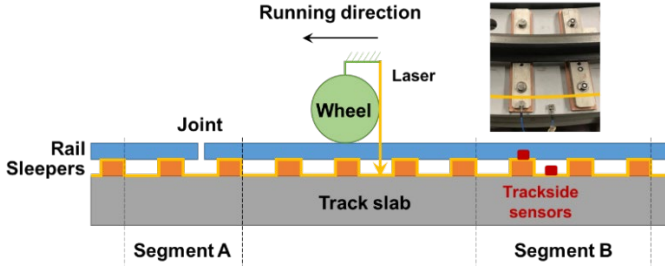osed methods (a 150~3,000 Hz band-pass filter is adopted in Step 3), which reflects good repeatability between the two laps. The bottom plot in Figure 2.18 (b) shows the averaged trackside measurements for two laps. The LDVom measurements after despeckle have good agreement with the trackside measurements. The dominant component at around 500 Hz is measured, and some high-frequency behavior related to sleeper dynamics is captured. The amplitudes of trackside measurements are lower than the LDVom measurements because the accelerometers are located at a distance from the joint. In addition, given the fact that the laser irradiates sleepers and track slabs in turn as the platform moves, we find that the proposed method is effective for the measurements on both surfaces.

Figure 2.18: Comparison with trackside measurements (Segment A). (a) Raw LDV signals at different laps; (b) Despeckle results and trackside signals.

Then, the measurement results on the normal track in Segment B are shown in Figure 2.19, including their time-frequency characteristics (at the same scale) after CWT with Morlet wavelet [117]. Compared with the trackside measurements, the LDVom successfully captures the dominant track vibration at 500~700 Hz, and their amplitudes

are similar. The repeatability and agreement are not as good as those in Figure 2.18 due to the lower vibration amplitude and the random nature of wheel-track dynamics.

Finally, the computational cost of the proposed methods is evaluated. In our case study, passing each sleeper segment at 20 km/h takes approximately 22.6 ms, while the corresponding CPU time for despeckle is 17.5 s on average. Although the despeckle algorithm cannot be implemented in real-time, it can be applied offline at acceptable computational costs.

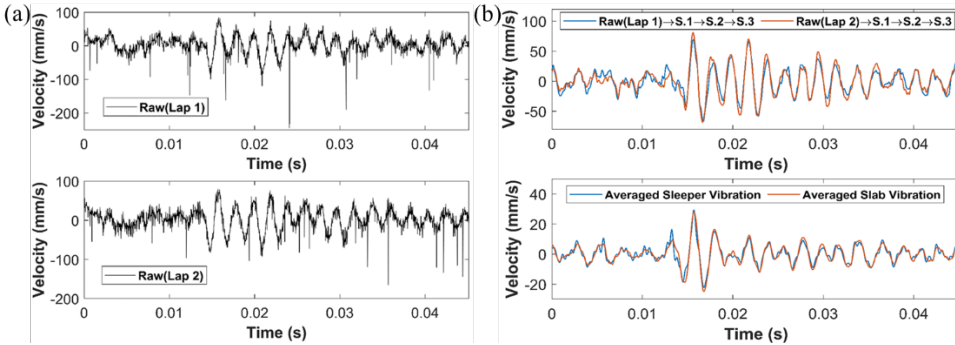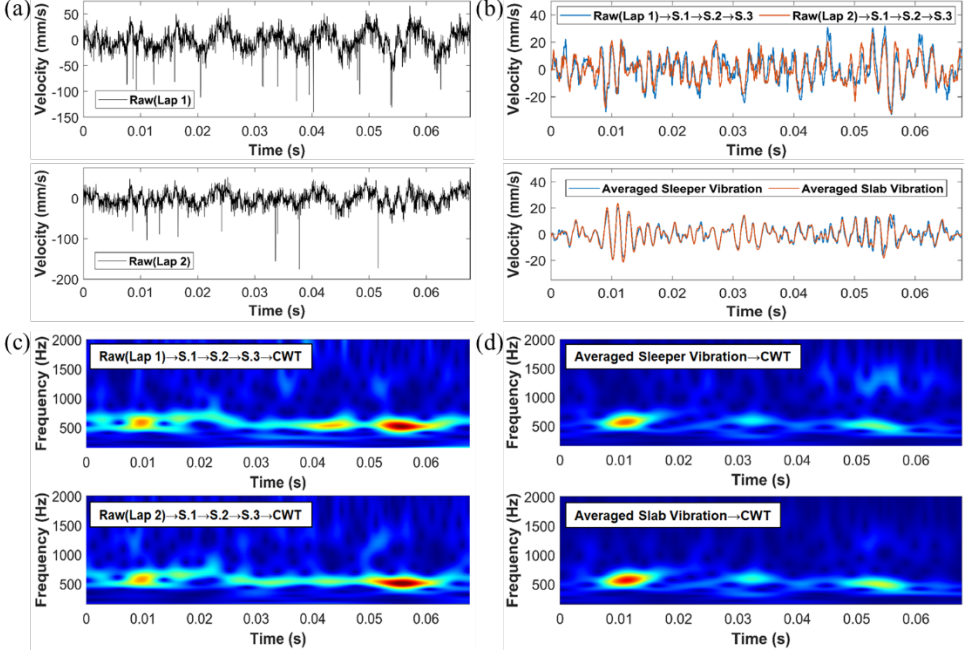Figure 2.19: Comparison with trackside measurements (Segment B). (a) Raw LDV signals at different laps; (b) Despeckle results and trackside signals; (c) Despeckle results in the time-frequency domain; (d) trackside signals in the time-frequency domain.

2.6. CONCLUSIONS

In this chapter, we study the characteristics of the speckle noise from LDVom measurements on railway tracks, propose and validate a three-step framework for speckle noise reduction, and compare the LDVom measurements with the trackside measurements. Specifically, we develop a wavelet-based spike detection method in Step 1 and an ARIMA-based imputation method in Step 2 and adopt a Butterworth filter in Step 3. The main conclusions are summarised below.

- In the time domain, the spikes occur discretely with random amplitudes and durations. In the frequency domain, they are broadband and can overlap with genuine vibrations. As the moving speed increases, the speckle noise occurs more frequently with shorter durations, greater amplitudes, and broader frequency bands.

- When applying conventional methods to despeckle, the amplitude of spikes can be shortened but not eliminated, which can lead to pseudo vibrations. The three-step framework can avoid this problem by detecting and replacing spikes, recovering false positives, and smoothing false negatives and residual noise.

- In addition to the proposed methods, different alternative methods can be adapted and used in the three steps of the despeckle framework. In Step 2, different training strategies can be selected considering the presence of speckle noise in time series.

- The proposed methods can effectively reduce the speckle noise at different speeds, among which the highest speed in this chapter is 20 km/h. The computational cost of the proposed methods is acceptable for offline applications.

- In our case study, the LDVom measurements can successfully capture the dominant components of the track vibrations at around 500~700 Hz with good repeatability between different laps and good agreement with trackside measurements.

2

2

3

OPERATIONAL MODAL IDENTIFICATION IN TIME-FREQUENCY REPRESENTATION

Operational modal analysis (OMA) enables the identification of modal characteristics under operational loads and conditions. Traditional frequency-domain methods cannot directly capture modal changes over time while existing time-frequency representations are not sufficiently interpretable due to spurious modes and implicit parameter design. This chapter develops a new OMA method in time-frequency representation based on frequency domain decomposition (FDD). Short-time FDD and a convolution-based strategy are proposed to obtain singular values and local mode shape similarity, respectively, which are further fused into mode indicators by a fuzzy-based strategy mimicking the modal assurance criterion. The method provides not only a global view of the modal characteristics over time and frequency but also estimates of modal parameters. It is applicable to strongly nonstationary responses under time-varying loads and conditions. All the parameters explicitly affect the time-frequency representation, and the interpretability is enhanced by including physical information from the user's prior knowledge in selecting parameters and peak bands. The proposed method is validated based on a study of railway sleepers under train passage. The rigid-body motions and bending modes are identified at frequencies up to 6,500 Hz in laboratory tests and 4,500 Hz in field tests at speeds up to 200 km/h. The identified natural frequencies and mode shapes agree with the experimental modal analysis. The proposed method outperforms the experimental modal analysis in terms of broad frequency range and low measurement cost and can be potentially applied to structural health monitoring under operational conditions.

3.1. INTRODUCTION

Operational modal analysis (OMA) enables the modal characteristics of a structure to be identified from its vibration response under operational loads and conditions. OMA methods in time-frequency representation can capture changes in modal characteristics over time. This chapter develops an interpretable OMA method suitable for strongly nonstationary responses by extending the frequency domain decomposition (FDD) method to a time-frequency representation. A study of railway sleepers under train passage is used to showcase the proposed method. The characteristics of the train-induced load on a sleeper vary considerably as the train approaches, passes, and leaves, which further affects the stiffness and damping of track components [145~147]. As a result, the sleeper vibration in response to train passage is significantly nonstationary. In addition, the damping effect from rail pads and ballast makes modal identification more challenging.

The remainder of this chapter is organized as follows. In Section 3.2, the fundamentals of FDD are briefly introduced. In Section 3.3, the new OMA method and the corresponding parameter selection strategy are proposed. In Section 3.4, the proposed method is validated through theoretical analysis and laboratory experiments. In Section 3.5, the proposed method is applied to field tests and compared with experimental modal analysis (EMA). Finally, some discussions are presented in Section 3.6, and the conclusions are summarized in Section 3.7.

3.2. FUNDAMENTALS OF FREQUENCY DOMAIN DECOMPOSITION

Structural responses are usually measured by accelerometers at a sampling frequency f_s. Estimating the PSD matrix of the response is the first step in FDD. Welch modified periodogram method [148] is widely used owing to its computational efficiency [66]. First, the measured response is divided into n_c overlapped (overlap ratio α_b) segments of equal length n_b, and a window function tapers each segment to reduce the leakage effect. The recommended overlap ratio α_b and window function are 0.5 and Hanning window, respectively [148]. Then, the modified periodogram $\mathbf{I}_k(f_n)$ is calculated for each windowed segment based on fast Fourier transform (FFT), where f_n is the n-th discrete frequency as follows [148].

$$f_n = \frac{nf_s}{n_b} \quad n = 0, \ ...,(n_b - 1)/2, \ n_b/2 \tag{3.1}$$

Next, the PSD matrix at each frequency f_n is estimated by averaging the periodograms over all n_c segments as follows [148].

$$\hat{\mathbf{S}}_{yy}(f_n) = \frac{1}{n_c}\sum_{k=1}^{n_c}\mathbf{I}_k(f_n) \tag{3.2}$$

Once $\hat{\mathbf{S}}_{yy}(f_n)$ is obtained, singular value decomposition (SVD) is applied to obtain [66],

$$\hat{\mathbf{S}}_{yy}(f_n) = \mathbf{U}(f_n)\mathbf{V}(f_n)\mathbf{U}(f_n)^{\mathrm{H}} \tag{3.3}$$

where $\mathbf{V}(f_n)$ is a diagonal matrix with singular values arranged in descending order and $\mathbf{U}(f_n)$ is a unitary matrix containing the singular vectors corresponding to the singular values. At each frequency f_n, a singular value in $\mathbf{V}(f_n)$ indicates the contribution of the corresponding singular vector in $\mathbf{U}(f_n)$, just as a modal response indicates the contribution of the corresponding mode shape based on the modal expansion of the structural response [66].

Mathematically, the number of segments n_c in PSD estimation determines the number of non-zero singular values in $\mathbf{V}(f_n)$ at each frequency [78], and multiple non-zero singular values allow for the identification of closely-spaced modes. All non-zero singular values can be plotted in a spectrum, where a resonance peak indicates the possible existence of a mode at the corresponding frequency. To further confirm such a mode, the singular vector of the peak is usually compared with other singular vectors at its adjacent frequencies. A popular scheme to quantify the similarity between two vectors is the modal assurance criterion (MAC) [66], denoted as $MAC(\boldsymbol{p}, \boldsymbol{q})$, which is equal to 0 (or 1) when the two vectors, $\boldsymbol{p}$ and $\boldsymbol{q}$, are orthogonal (or proportional). If the singular vectors in the vicinity of a peak are of high similarity (MAC greater than a threshold), they are identified as belonging to the same dominant mode [66, 86].

Once a mode is confirmed, its modal parameters can be estimated following the strategy of enhanced FDD [82, 83]. First, an auto PSD function is created using the identified singular values at the corresponding frequencies, representing an equivalent single degree of freedom system. Then, inverse FFT is applied to the auto PSD to obtain an autocorrelation function in the time domain. The zero crossings of the autocorrelation function can give an estimate of the damped natural frequency, while the extremes can be used to estimate the logarithmic decrement δ through linear regression. Further, the damping ratio is calculated as follows [82, 83].

$$\xi = \frac{\delta}{\sqrt{\delta^2 + 4\pi^2}} \tag{3.4}$$

Finally, a real-valued mode shape vector can be obtained from each of the identified singular vectors. A simple approach [66] is to normalize the complex singular vector by the maximum absolute value of its components and then rotate each component to 0°(or 180°) if its phase lies in the first or fourth (or the second or third) quadrant. A mode shape vector can be displayed with respect to sensor positions in a static plot. It is noteworthy that the problem of spatial aliasing can occur when the number of sensors is insufficient. In this case, the identified mode shape should be interpreted carefully.

In general, the validity of FDD is based on the assumptions of white noise excitations, low structural damping ratios, and orthogonal mode shapes for closely-spaced modes [86]. If these assumptions are not fully satisfied or measurement noise is present, the identification result is an approximation to real modal characteristics [86, 149].

3.3. TIME-FREQUENCY REPRESENTATION OF OMA

This chapter develops a new OMA method, named TFOMA, by extending the FDD method to a time-frequency representation. Figure 3.1 shows its framework. First, short-time FDD and a convolution-based strategy are proposed to obtain singular values and

local mode shape similarity, respectively. Then, they are fused into mode indicators by a fuzzy-based strategy, and modal parameters are further estimated. Section 3.3.1~3.3.3 will introduce these main steps, and Section 3.3.4 will discuss the parameter selection strategy.
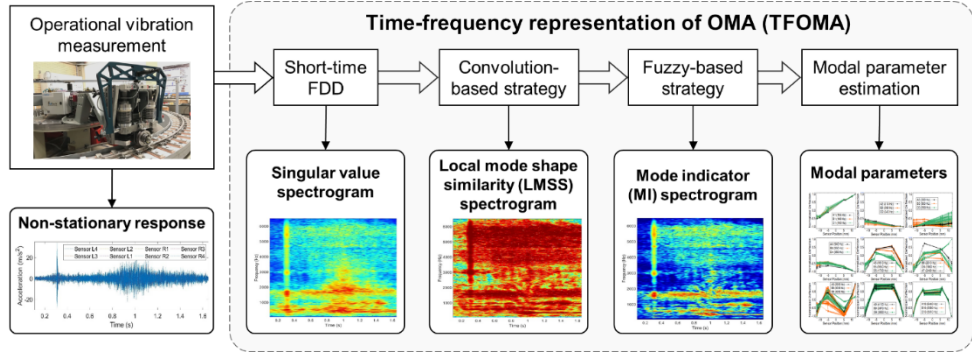
Figure 3.1: Framework of TFOMA.

3.3.1. SHORT-TIME FDD

In FDD, Fourier transform is used to average the frequency information over the entire signal time, which is theoretically applicable to stationary processes. Short-time Fourier transform [150] is a modified version of Fourier transform for strongly nonstationary signals. We apply a similar strategy to FDD as follows and name it short-time FDD (STFDD),

$$\mathbf{STFDD}\{\mathbf{y}(s)\}(t,f) = \mathbf{FDD}\{\mathbf{y}(s)r(s-t)\}(f) \tag{3.5}$$

where $\mathbf{y}(s)$ is the vector of synchronized measurement from multiple sensors at sampling time s and $r(s-t)$ represents a rectangular window centered at t.

Figure 3.2: Short-time FDD and singular value spectrogram.

As illustrated in Figure 3.2, $\mathbf{y}(s)$ is broken into segments of equal length with an overlap ratio α_s, and the procedures of PSD estimation and SV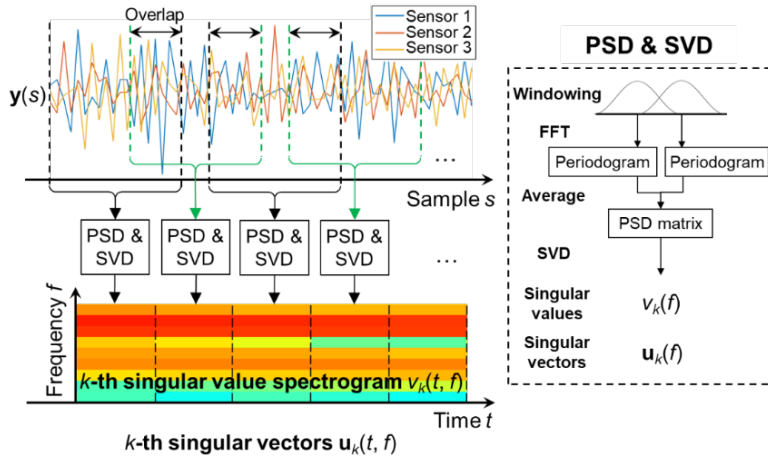D are applied to each segment, producing a series of singular value matrices $\mathbf{V}(t, f)$ and singular vector matrices $\mathbf{U}(t, f)$. The k-th diagonal term in $\mathbf{V}(t, f)$ is denoted as $v_k(t, f)$, and the k-th singular vector in $\mathbf{U}(t, f)$ is denoted as $\mathbf{u}_k(t, f)$. At the k-th level, a singular value spectrogram can be obtained by plotting $v_k(t, f)$ over time and frequency with color mapping. According to Section 3.2, the number of effective spectrograms is equal to the number of non-zero singular values, which is further equal to n_c used in PSD estimation. It is noteworthy that STFDD also holds the drawbacks of STFT, such as the trade-off between time and frequency resolutions (discussed in Section 3.3.4).

3

3.3.2. LOCAL MODE SHAPE SIMILARITY

A peak in a singular value spectrogram indicates the possible existence of a structural mode. According to MAC, a mode is effectively dominant when the singular vector of the peak has a high similarity to the singular vectors in its vicinity. To enable comparisons in both time and frequency dimensions, we propose a convolution-based strategy to quantify the local similarity of singular vectors. In a two-dimensional representation, e.g., an image, convolution works by applying a kernel to each location and evaluating the central element based on all elements in the kernel [151, 152]. In the time-frequency representation, we adapt it to compute the following scalar, named local mode shape similarity (LMSS),

$$l_k(t,f) = \sum_{dt=-a}^{a} \sum_{df=-b}^{b} \omega(dt,df) \cdot MAC\left(\mathbf{u}_k(t,f), \mathbf{u}_k(t + dt \cdot \Delta t, f + df \cdot \Delta f)\right) \tag{3.6}$$

where a, b are the half kernel sizes (number of elements) in time and frequency, respectively, Δt, Δf are the time and frequency resolutions, respectively, and $\omega(dt, df)$ represents the weight at each element of the kernel.

LMSS is a weighted sum of MAC values between the central element and all other elements in a kernel. In this chapter, a separable kernel with Gaussian functions [152, 153] is used, and its weights are determined as follows,

$$\omega(dt,df) = \begin{cases} 0 & \text{if } dt = 0 \text{ and } df = 0 \\ \dfrac{\omega_0(dt,df)}{\displaystyle\sum_{dt'=-a}^{a} \sum_{df'=-b}^{b} \omega_0(dt',df') - \omega_0(0,0)} & \text{otherwise} \end{cases} \tag{3.7}$$

where the weight of the central element is zero and $\omega_0(dt, df)$ is the un-normalized weight calculated based on the following Gaussian functions,

$$\omega_0(dt,df) = \exp\left(-\frac{dt^2}{2\sigma_t^2}\right) \cdot \exp\left(-\frac{df^2}{2\sigma_f^2}\right) \cdot \exp\left(-\frac{dv_{(t,f)}(dt,df)^2}{2\sigma_v^2}\right) \tag{3.8}$$

where $dv_{(t, f)}(dt, df)$ denotes the logarithmic difference in singular values with respect to the central element, as calculated as follows.

$$dv_{(t,f)}(dt, df) = \log\left[v_k\left(t + dt \cdot \Delta t, f + df \cdot \Delta f\right)\right] - \log\left[v_k\left(t, f\right)\right] \tag{3.9}$$

Further, σ_t, σ_f, σ_v are standard deviations characterizing the decay rates of the weight as dt, df, dv increase, respectively. We recommend determining them as follows,

$$\sigma_t = \frac{a+1}{3} \quad \sigma_f = \frac{b+1}{3} \quad \sigma_{v_{(t,f)}} = \sqrt{\frac{1}{(2a+1)\cdot(2b+1)-1}\sum_{dt=-a}^{a}\sum_{df=-b}^{b}\left[dv_{(t,f)}(dt, df)\right]^2} \tag{3.10}$$

Eq. (3.8)~(3.10) reflect that, from the kernel center to the kernel boundary, the weight decreases from one towards zero as dt or df increases, according to the three-sigma rule. This property allows comparisons to be made in a localized manner with smooth transitions at kernel boundaries. Additionally, the weight is lower when an element's singular value deviates more from the center's. This property enhances the adaptability of LMSS to structural modes with different bandwidths since the weight decays faster in case of a sharper resonance peak and vice versa. Meanwhile, it allows LMSS to better capture the shift in resonance frequency over time.

Figure 3.3 illustrates the calculation process of LMSS at the k-th level. An LMSS spectrogram can be obtained by plotting $l_k(t, f)$ over time and frequency with color mapping. The value of each point indicates the similarity of mode shapes between that point and its vicinity, and a peak region indicates a high local similarity at that time and frequency, which can help to confirm the dominance of a mode.
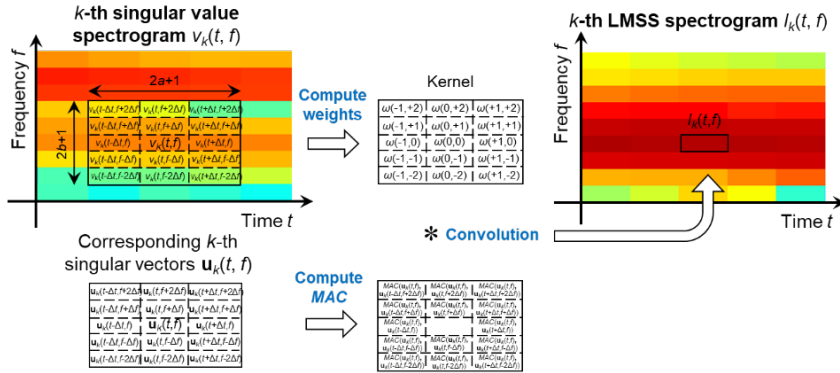

Figure 3.3: Local mode shape similarity and its spectrogram.

3.3.3. Mode indicator

After obtaining the singular value spectrogram and the LMSS spectrogram, structural modes can be identified from regions with both large singular values and large LMSS. In this chapter, a fuzzy-based fusion strategy is proposed to fuse $v_k(t, f)$ and $l_k(t, f)$ at each time and frequency into a mode indicator (MI), denoted as $MI_k(t, f)$. Fuzzy set theory quantifies the membership of an element in a set through a membership function [154], which is usually used to handle vague information, e.g., fusing multiple images [155~157]. It is suitable for computing MI because there is no precise relationship to determine the existence of modes based on $v_k(t, f)$ and $l_k(t, f)$ but rather a soft and flexible thresholding strategy according to MAC.

First, all $v_k(t, f)$ and $l_k(t, f)$ are normalized as follows.

$$\begin{cases} v_k'\left(t, f_n\right) = \dfrac{\log\left(v_k\left(t, f\right)\right) - \min\left(\log\left(v_k\left(t, f\right)\right)\right)}{\max\left(\log\left(v_k\left(t, f\right)\right)\right) - \min\left(\log\left(v_k\left(t, f\right)\right)\right)} \\[4mm] l_k'\left(t, f\right) = \dfrac{l_k\left(t, f\right) - \min\left(l_k\left(t, f\right)\right)}{\max\left(l_k\left(t, f\right)\right) - \min\left(l_k\left(t, f\right)\right)} \end{cases} \tag{3.11}$$

Then, we use the following membership function to compute the MI,

$$MI_k\left(t, f\right) = \left[v_k'\left(t, f\right)\right]^{\lambda_v} \cdot \left[l_k'\left(t, f\right)\right]^{\lambda_l} \tag{3.12}$$

where λ_v and λ_l are the contribution exponents of $v'_k(t, f)$ and $l'_k(t, f)$, respectively.

Figure 3.4 illustrates the calculation of MI, in which the membership function with $\lambda_v=1$ and $\lambda_l=3$ is shown as an example. It can be seen that $MI_k(t, f)$ approaches 0 when $v'_k(t, f)$ or $l'_k(t, f)$ is small and tends to 1 as $v'_k(t, f)$ and $l'_k(t, f)$ increase. Meanwhile, $l'_k(t, f)$ is more dominant than $v'_k(t, f)$ owing to the selection of λ_v and λ_l. As a consequence, when $l'_k(t, f)$ is less than 0.45, $MI_k(t, f)$ is lower than 0.1 even if $v'_k(t, f)$ is large. The selection of λ_v and λ_l enables the proposed fuzzy-based strategy to mimic a thresholding strategy of MAC and provide a soft and interpretable fusion between $v_k(t, f)$ and $l_k(t, f)$.
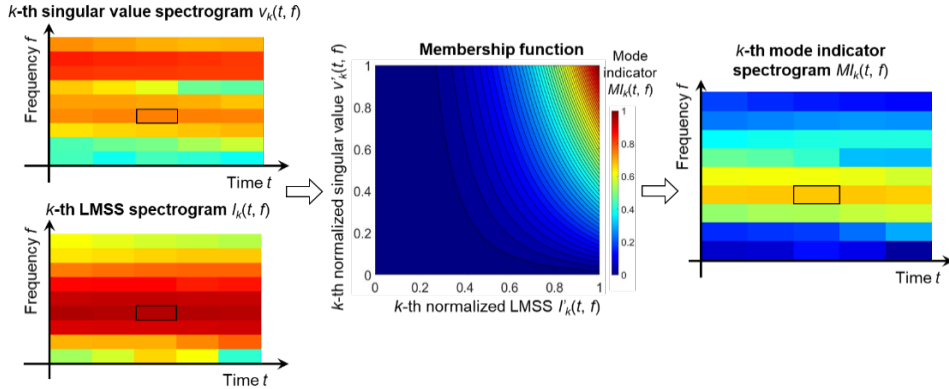

Figure 3.4: Membership function and mode indicator spectrogram.

As shown in Figure 3.4, the computed MIs at the k-th level $MI_k(t, f)$ can be plotted as an MI spectrogram with peak regions indicating the presence of structural modes. Then, a frequency band that peaks continuously over time at physically meaningful frequencies is selected for each mode. To further estimate the modal parameters of a mode, the singular values in its frequency band with MIs greater than a threshold are selected to create auto PSD functions, which can then be used to estimate the natural frequency and damping ratio at each time instant (see Section 3.2). Meanwhile, the singular vectors corresponding to the selected singular values can be converted into mode shape vectors (see Section 3.2). In this way, the proposed TFOMA method provides not only a global view of the modal characteristics over time and frequency but also estimates of modal parameters.

3.3.4. PARAMETER SELECTION STRATEGY

The time-frequency representation of the proposed method depends on the selection of its parameters. Sufficient time and frequency resolutions are necessary for clear visualization of modal characteristics and accurate estimation of modal parameters. The frequency resolution Δf and the time resolution Δt are determined as follows.

$$\Delta f = \frac{f_s}{n_b} \qquad \Delta t = \frac{n_b(1-\alpha_s)\left[n_c(1-\alpha_b)+\alpha_b\right]}{f_s} \tag{3.13}$$

We propose the following strategy to select all the parameters of the TFOMA method.

Step 1. Select the number of segments n_c in PSD estimation. As mentioned in Section 3.2 and 3.3.1, n_c determines the number of non-zero singular values. For structures with separated modes, n_c can be set to 1, whereas in cases of closely-spaced modes, n_c should be greater than the maximum number of physical modes in each identified frequency band.

Step 2. Select the segment length n_b in PSD estimation and the overlap ratio α_s in STFDD. According to Eq. (3.13), they directly affect Δf and Δt: larger n_b leads to smaller Δf but larger Δt, and larger α_s leads to smaller Δt but higher computational costs. We recommend first selecting n_b to provide sufficient frequency resolution, e.g., at least five discrete frequencies in the frequency band of a mode. Then, α_s can be selected to provide sufficient time resolution, e.g., Δt to be shorter than the nonstationary behavior of the signal.

Step 3. Select the half kernel sizes a and b. Under defined Δt and Δf, the kernel lengths in time and frequency are $(2a+1)\cdot\Delta t$ and $(2b+1)\cdot\Delta f$, respectively. For comparisons in a localized manner, we recommend setting a and b as small integers, such as 3~10, to ensure that $(2a+1)\cdot\Delta t$ and $(2b+1)\cdot\Delta f$ are shorter than the duration and bandwidth of each mode, respectively.

Step 4. Select the contribution exponents λ_v and λ_l. As exemplified in Section 3.3.3, we recommend setting $\lambda_l > \lambda_v = 1$ to mimic a thresholding strategy of MAC. The larger λ_l is, the greater the influence of LMSS on MI, i.e., a higher LMSS is required to reach a certain level of MI.

All parameters in the TFOMA method explicitly affect the time-frequency representation. They can be selected and tuned according to the user's prior knowledge of the structural dynamics and goals of analyses.

3.4. VALIDATION VIA LABORATORY TESTS

3.4.1. TFOMA OF AN IN-SITU SLEEPER

We validate the proposed TFOMA method in the V-Track test rig. The introduction of this test rig can be found in Section 2.2.1. As shown in Figure 3.5, we instrument one sleeper with eight accelerometers (PCB 356B21) on its top surface. The vertical accelerations are measured at the sampling frequency of f_s=102,400 Hz. The running

speed of the wheel is 8 km/h. Figure 3.6 (a) plots the measured sleeper accelerations with four phases distinguished, which shows significant nonstationarity. Phase A is the impact response caused by the passage over a joint that is several sleepers away from the instrumented sleeper. Phase B~D belong to the response caused by the wheel passage, divided into pre-passage, under-passage, and post-passage phases.
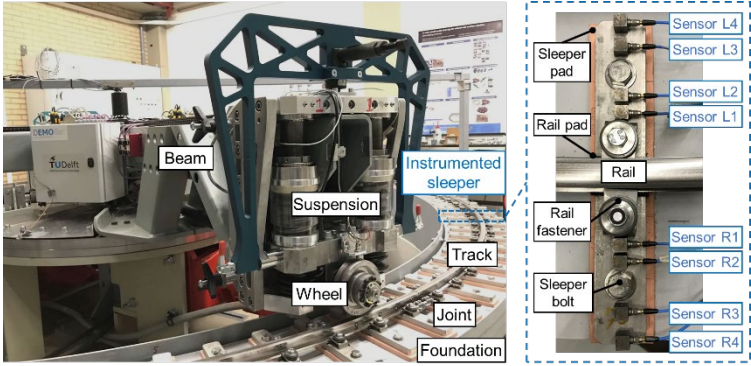

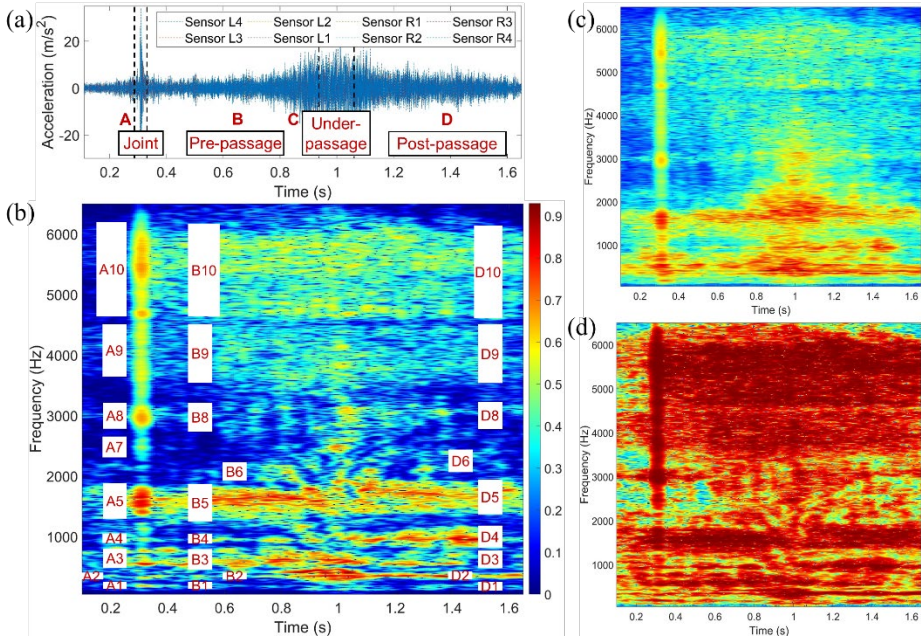Figure 3.5: V-Track test rig and the instrumented sleeper.

Figure 3.6: TFOMA results of laboratory tests. (a) Sleeper accelerations in the time domain; (b) MI spectrogram; (c) Singular value spectrogram; (d) LMSS spectrogram.

We apply the TFOMA method to the measured data with the parameters listed in Table 3.1. The spectrograms of singular value, LMSS, and MI are shown in Figure 3.6 at frequencies up to 6,500 Hz. As shown in Figure 3.6 (c) and (d), most of the large singular values are located below 2,000 Hz, while the large LMSS is present throughout

the frequency range. By fusing the singular values with the LMSS, we obtain the MI spectrogram in Figure 3.6 (b), which shows peak regions with sharper edges than those in Figure 3.6 (c) and (d), making them easier to identify.

Table 3.1: Selected parameters for laboratory tests.

Parameters	Values	Parameters	Values
Number of segments n_c	1	Segment length n_b	10,240 (0.1 s)
Overlap ratio in PSD estimation α_b	0.5	Overlap ratio in STFDD α_s	0.95
Half kernel size in time a	10	Half kernel size in frequency b	5
Exponent of singular value λ_v	1	Exponent of LMSS λ_l	3
Time resolution Δt	5 ms	Frequency resolution Δf	10 Hz

In the MI spectrogram, the impact response in Phase A produces a vertical ridge, along which the MI peaks at some frequencies. In Phase B and D, a number of peak bands can be observed, which continuously dominate at frequencies close to the peaks in Phase A. The peaks in Phase C are less clear as they belong to the forced response phase. We select ten peak bands in Phase A, B, and D, as labeled in Figure 3.6 (b), where the label height represents the bandwidth. At low (or high) frequencies, the density of peak bands is high (or low), and their bandwidths are narrow (or wide). In each selected band, we use points with MI greater than 0.4 for further parameter estimation, and the identified mode shapes and average natural frequencies are shown in Figure 3.7. Most identification results are consistent between Phase A, B, and D, though the passage response suffers more nonstationarity and noise.
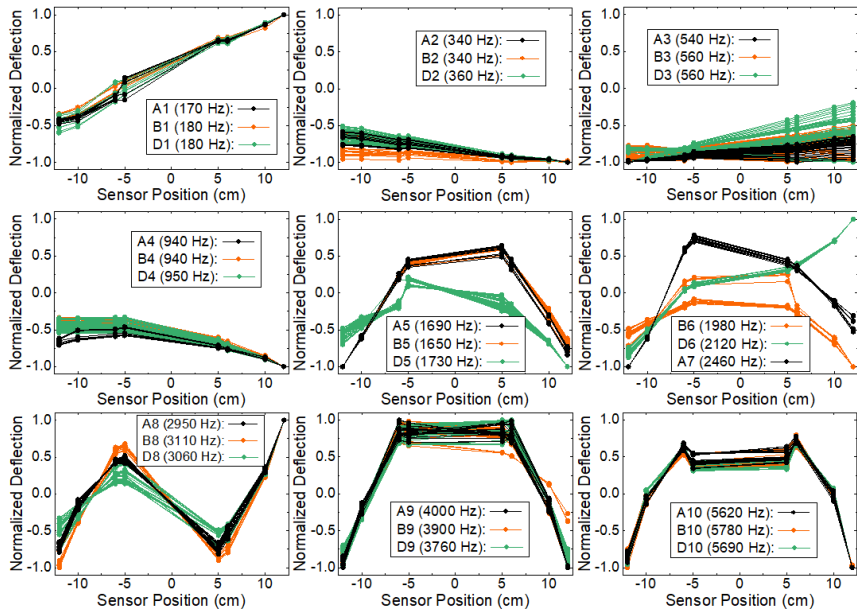

Figure 3.7: Modal identification results of laboratory tests.

3.4.2. EMA and theoretical analysis of a free sleeper

To verify the above identification results, we perform hammer tests on a free sleeper of the same type on an elastic foundation. Since the sleeper is free of rail fasteners, it is instrumented with more distributed accelerometers (PCB 356B21), as shown in Figure 3.8 (a). We use a small hammer (Brüel & Kjær 8206-003) to generate the impact at each of the four locations.

To reduce the effect of leakage and noise, the measured response from each sensor is tapered by an exponential window, and the measured force is tapered by the same exponential window and also a force window [158]. Then, for the i-th sensor (i=1, …, 9) in response to the impact at the j-th location (j=1, …, 4), we compute the cross PSD between the acceleration and the force $S_{a_i p_j}(f)$ and the PSD of the force $S_{p_j p_j}(f)$ using Welch modified periodogram method [148]. Further, the frequency response function (FRF), more specifically the receptance function, is calculated as follows [159].

$$H_{ij}(f) = \frac{S_{a_i p_j}(f)}{S_{p_j p_j}(f)(2\pi f)^2} \tag{3.14}$$

An FRF is a complex function of frequency that describes the response of a structure at the sensor position to excitation at the impact location. A resonance peak indicates the presence of a structural mode at the corresponding frequency. The mode shape vector can be obtained by combining the imaginary parts of the FRFs from different sensors as follows [159].

$$\left[\mathrm{Im}\left(H_{1j}(f)\right), \quad \mathrm{Im}\left(H_{2j}(f)\right), \quad ..., \quad \mathrm{Im}\left(H_{9j}(f)\right) \right]^{\mathrm{T}} \tag{3.15}$$

At each impact location, we repeat the test three times and average the FRFs as the final result. For example, Figure 3.8 (b) plots the magnitude of the FRFs for all sensors in response to Impact 2. Four resonance peaks are identified from all FRFs at different impact locations, labeled as P0~P3, and their mode shapes and average frequencies are shown in Figure 3.8 (c).

Meanwhile, we calculate the theoretical mode shapes by simplifying the sleeper as a free-free beam, and the n-th order mode shape is given as follows [160],

$$w_n(x) = \left[\sinh(k_n x) + \sin(k_n x) \right] + \frac{\sin(k_n L) - \sinh(k_n L)}{\cosh(k_n L) - \cos(k_n L)} \left[\cosh(k_n x) + \cos(k_n x) \right] \tag{3.16}$$

where L is the beam length, x is the coordinate along the beam ($0 \le x \le L$), sinh and cosh are hyperbolic functions, and k_n is the n-th solution of the following equation of k.

$$\cosh(kL)\cos(kL) = 1 \tag{3.17}$$

The mode shapes of a free-free beam with L=25 cm are computed and plotted in Figure 3.8 (c). Clearly, the mode shapes of P1~P3 are in good agreement with the theoretical mode shapes of the first three bending modes, respectively, and P0 is the rigid-body motion of the sleeper.
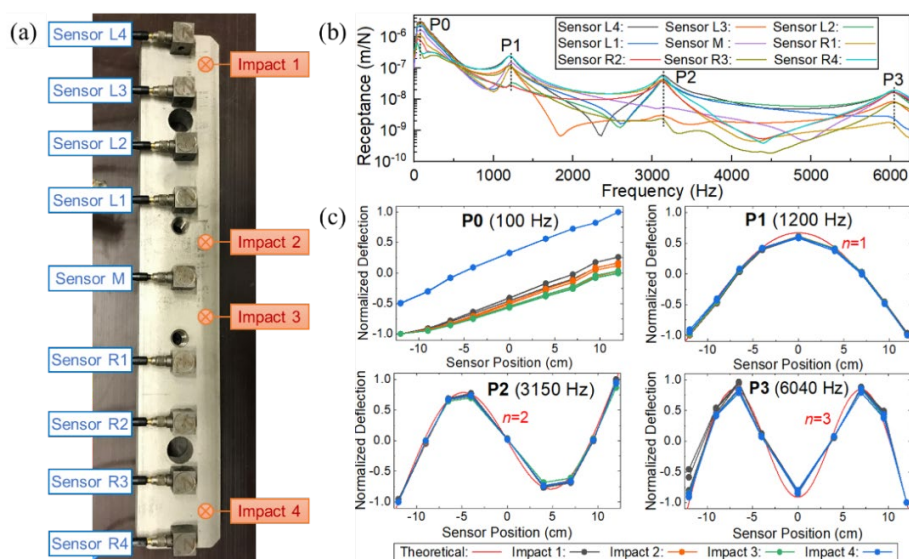
Figure 3.8: EMA and theoretical analysis of a free sleeper. (a) Test setup; (b) FRFs of all sensors for Impact 2; (c) Mode shapes and frequencies of the four resonance peaks.
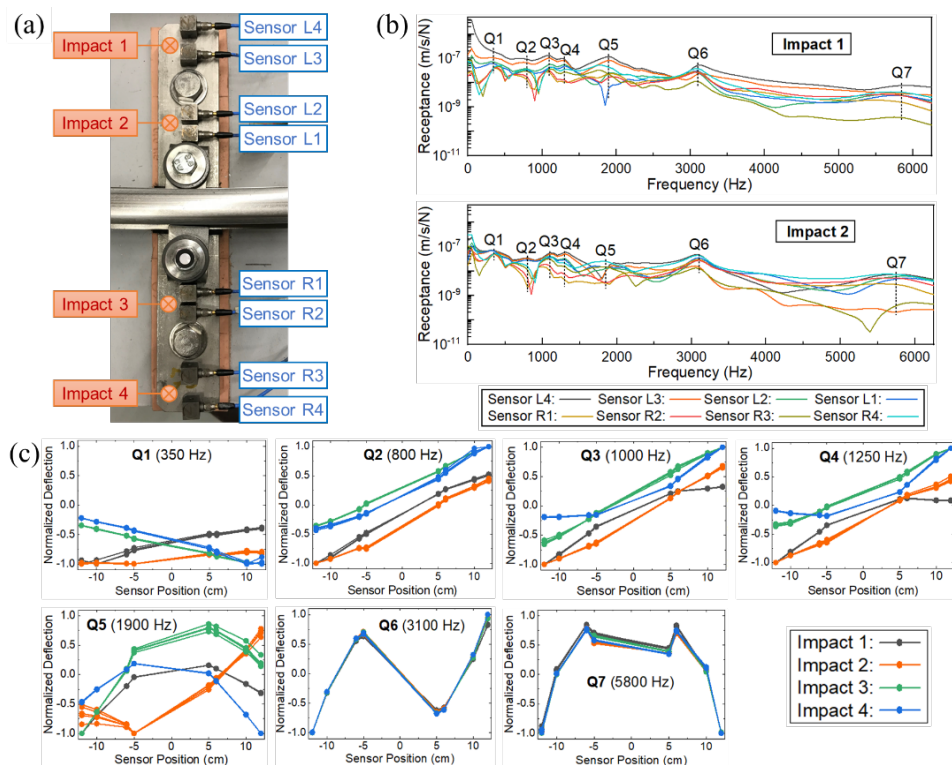

Figure 3.9: EMA results of the in-situ sleeper in laboratory tests. (a) Test setup; (b) FRFs of all sensors for Impact 1 and 2; (c) Mode shapes and frequencies of the seven resonance peaks.

3.4.3. EMA of the in-situ sleeper

Hammer tests are also performed on the in-situ sleeper in Section 3.4.1 using the same hammer. The locations of impacts and sensors are shown in Figure 3.9 (a). We repeat the test five times at each location, which is more than that of the free sleeper due to lower repeatability. The average FRFs for the first two impact locations are shown in Figure 3.9 (b) as examples. Seven resonance peaks are identified, labeled as Q1~Q7. The corresponding natural frequencies and mode shapes are shown in Figure 3.9 (c).

Compared with the free sleeper, the in-situ sleeper shows more resonance peaks below 2,000 Hz, and their mode shapes deviate for different impact locations. Q1~Q4 correspond to rigid-body motions but are not comparable to P0 due to different boundary conditions. Q5~Q7 correspond to P1~P3 (the first three bending modes), respectively. The results of Q5 and P1 show significant deviations. The frequencies of Q6 and P2 are consistent, while those of Q7 and P3 deviate slightly. Besides, the peaks of the in-situ sleeper are smoother due to the damping effect. The above findings reflect the differences in modal characteristics due to different boundary conditions and also the influence of other track components.

3.4.4. Comparisons between TFOMA and EMA

By comparing the identification results of TFOMA and EMA for the same in-situ sleeper, we find that:

- A1/B1/D1~A4/B4/D4 in TFOMA correspond to Q1~Q4 in EMA (the rigid-body motions). They have similar frequency bands, but the bounce motion is more dominant in TFOMA, while the roll motion is more dominant in EMA. This indicates that the rigid-body motions are sensitive to the characteristics of excitations.

- A5/B5/D5 in TFOMA correspond to Q5 in EMA (the 1st bending mode) with the *MAC* of 0.92/0.93/0.44. Among the first three bending modes, the 1st bending mode is the most dominant in both TFOMA and EMA. The frequencies of TFOMA are lower than that of EMA, and A5/B5 provides a higher *MAC* than D5.

- A8/B8/D8 in TFOMA correspond to Q6 in EMA (the 2nd bending mode) with the *MAC* of 0.95/0.98/0.87. Their frequencies are consistent.

- A10/B10/D10 in TFOMA correspond to Q7 in EMA (the 3rd bending mode) with the *MAC* of 0.98/0.97/0.98. Their frequencies are consistent.

- B6/D6/A7 and A9/B9/D9 in TFOMA belong to extra modes related to other track components, e.g., rails.

In summary, TFOMA provides comparable identification results to EMA. The differences in the identified modal parameters reflect the influence of a moving train load on track dynamics. Among the three phases in TFOMA, the impact response and the pre-passage phase outperform the post-passage phase in terms of mode shape consistency with EMA.

3.5. APPLICATION TO FIELD TESTS

3.5.1. TFOMA OF AN IN-SITU SLEEPER

We test the proposed method using sleeper vibrations measured at Faurei Railway Test Center in Romania. The track consists of UIC60 E1 rails, Vossloh W14 fastening systems, and B70-W60 prestressed concrete sleepers. As shown in Figure 3.10, four accelerometers (Brüel & Kjær 4514-004) are mounted on a sleeper. A train passes over the instrumented sleeper at three different speeds –15 km/h, 80 km/h, and 200 km/h. The vertical accelerations are recorded at a sampling frequency of 25,600 Hz. We find that Sensor L2 was not functional, most likely due to a loose installation, so we use the data from the other three functional sensors for analysis.
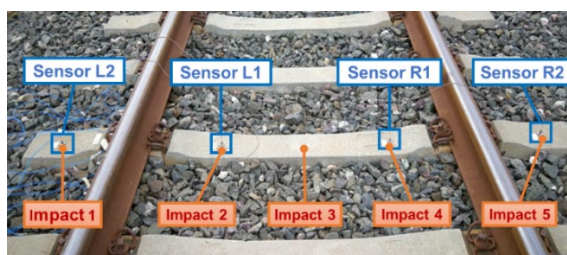

Figure 3.10: The instrumented sleeper in field tests.

The TFOMA method is applied to the measured data with the parameters listed in Table 3.2. According to Section 3.4, only the pre-passage phases are studied, while different lengths of signals are used due to the difference in speeds. The raw data and the corresponding MI spectrograms up to 4,500 Hz are shown in Figure 3.11. Generally, the patterns of MI are similar at different speeds. Some peak bands are wide in frequency, whereas others are narrow. The low-frequency bands are more pronounced at low speeds, especially when the train is close to the sleeper, whereas the high-frequency bands are more pronounced at high speeds and continuously dominant even when the train is still far away from the sleeper. In addition, some peak bands are not horizontal, i.e., their frequencies change as the train approaches.

Table 3.2: Selected parameters for field tests.

Parameters	Values	Parameters	Values
Number of segments n_c	1	Segment length n_b	5,120 (0.2 s)
Overlap ratio in PSD estimation α_b	0.5	Overlap ratio in STFDD α_s	0.95
Half kernel size in time a	10	Half kernel size in frequency b	5
Exponent of singular value λ_v	1	Exponent of LMSS λ_l	3
Time resolution Δt	10 ms	Frequency resolution Δf	5 Hz

We select fourteen peak bands at each speed, labeled as O1~O14. The first four columns of Table 3.3 present the characteristics of each peak band and also the average natural frequencies and mode shapes. In each plot, the identified mode shapes at a certain

speed are plotted in a light color, and their average is plotted in a dark color. In general, the identified frequencies and mode shapes are similar at different speeds while varying slightly due to the influence of train speed and noise. More discussion will be provided in Section 3.5.3.
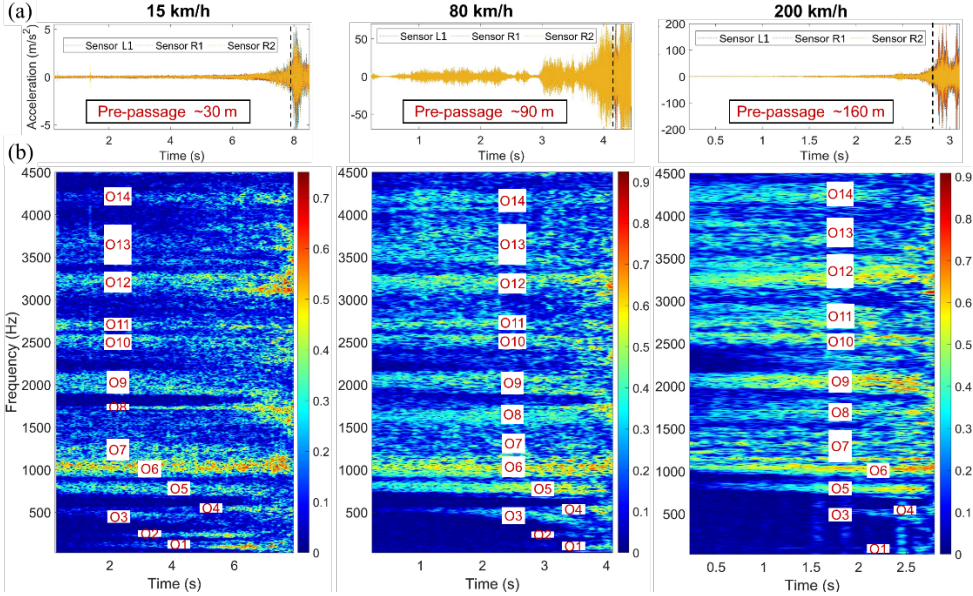

Figure 3.11: TFOMA results of field tests. (a) Sleeper accelerations at 15 km/h, 80 km/h, 200 km/h in the time domain; (b) MI spectrograms at 15 km/h, 80 km/h, 200 km/h.
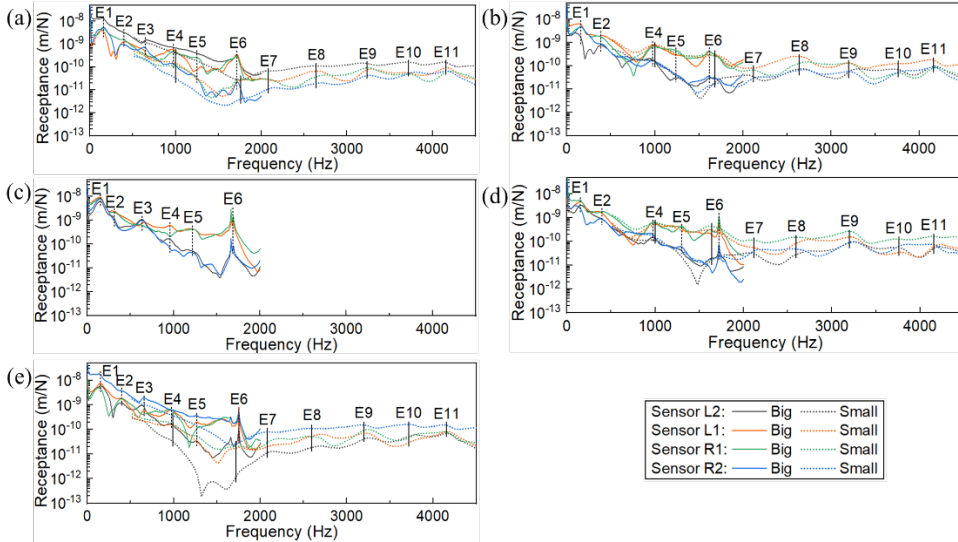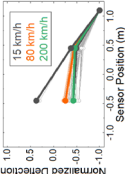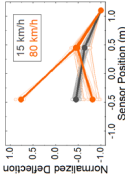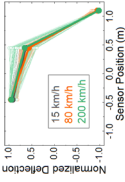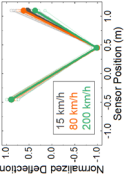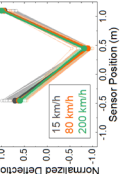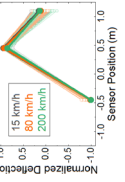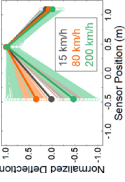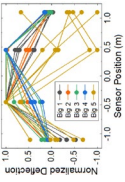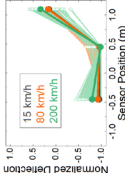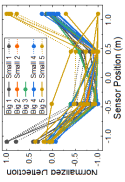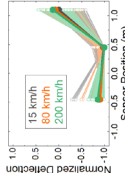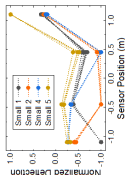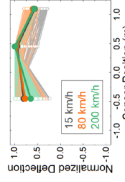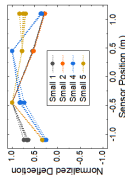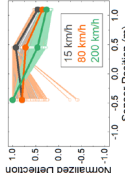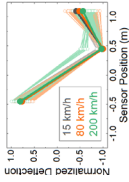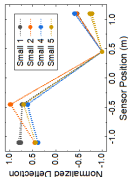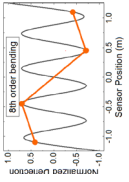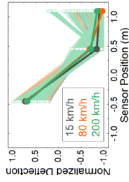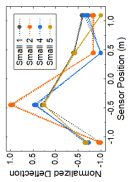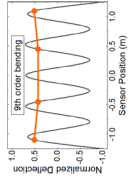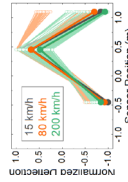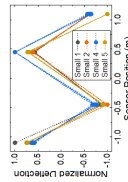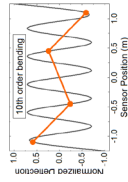

Figure 3.12: EMA results of field tests. (a) FRFs for Impact 1; (b) FRFs for Impact 2; (c) FRFs for Impact 3; (d) FRFs for Impact 4; (e) FRFs for Impact 5.

Table 3.3: Comparisons between the results of TFOMA, EMA, and theoretical analysis.

TFOMA				EMA			Avg. MAC	Theoretical analysis		Comparisons
Order	Characteristics	Avg. freq.	Mode shapes	Order	Avg. freq.	Mode shapes		Order	Mode shapes	
O1	They are pronounced when the train is close, especially at low speeds.	f_{15}=100 Hz f_{80}=95 Hz f_{200}=95 Hz	*(mode shape plot)*	/	/	/	/	Bounce	*(Bounce mode shape plot)*	TFOMA identifies the rigid-body motions, whereas EMA fails.
O2		f_{15}=235 Hz f_{80}=220 Hz	*(mode shape plot)*	/	/	/	/	Roll	*(Roll mode shape plot)*	
O3	Its frequency drops as the train approaches.	f_{15}=475 Hz f_{80}=490 Hz f_{200}=495 Hz	*(mode shape plot)*	E1	160 Hz	*(mode shape plot)*	0.98	1st bending	*(1st order bending plot)*	TFOMA and EMA identify the 1st bending mode, while their frequencies deviate significantly.
O4	It is pronounced when the train is close, especially at low speeds.	f_{15}=535 Hz f_{80}=540 Hz f_{200}=525 Hz	*(mode shape plot)*	E2	395 Hz	*(mode shape plot)*	0.97	2nd bending	*(2nd order bending plot)*	TFOMA and EMA identify the 2nd bending mode, while their frequencies deviate.
O5	Its frequency drops slightly.	f_{15}=760 Hz f_{80}=790 Hz f_{200}=800 Hz	*(mode shape plot)*	E3	650 Hz	*(mode shape plot)*	0.64	3rd bending	*(3rd order bending plot)*	Neither TFOMA nor EMA identifies the 3rd bending mode.
O6	It is the most dominant band at 15 km/h and 80 km/h.	f_{15}=1060 Hz f_{80}=1050 Hz f_{200}=1060 Hz	*(mode shape plot)*	E4	975 Hz (Big); 1000 Hz (Small)	*(mode shape plot)*	0.99	4th bending	*(4th order bending plot)*	TFOMA and EMA identify the 4th bending mode, while their frequencies are consistent.

3

TFOMA				EMA			Avg. MAC	Theoretical analysis		Comparisons
Order	Characteristics	Avg. freq.	Mode shapes	Order	Avg. freq.	Mode shapes		Order	Mode shapes	
O7	Its frequency band is wide while without clear boundaries.	f_{15}=1230 Hz f_{80}=1270 Hz f_{200}=1280 Hz		E5	1250 Hz		0.34	/	/	TFOMA and EMA identify extra modes.
O8	Its frequency band is narrow at 15 km/h and wider at higher speeds.	f_{15}=1725 Hz f_{80}=1695 Hz f_{200}=1705 Hz		E6	1700 Hz (Big); 1700 Hz (Small)		0.99	5th bending		TFOMA and EMA identify the 5th bending mode, while their frequencies are consistent.
O9	It is more pronounced at higher speeds. Its frequency drops slightly.	f_{15}=1995 Hz f_{80}=2050 Hz f_{200}=2060 Hz		E7	2100 Hz		0.82	6th bending		Neither TFOMA nor EMA identifies the 6th bending mode.
O10	They are more pronounced at higher speeds.	f_{15}=2520 Hz f_{80}=2530 Hz f_{200}=2580 Hz		E8	2620 Hz		0.93	7th bending		TFOMA and EMA identify the 7th bending mode, while their frequencies are consistent.
O11		f_{15}=2695 Hz f_{80}=2700 Hz f_{200}=2710 Hz					0.99			

3

TFOMA				EMA				Avg. MAC	Theoretical analysis		Comparisons
Order	Characteristics	Avg. freq.	Mode shapes	Order	Avg. freq.	Mode shapes			Order	Mode shapes	
O12	Its frequency increases slightly as the train approaches.	f_{15}=3220 Hz f_{80}=3240 Hz f_{200}=3230 Hz		E9	3200 Hz			0.99	8th bending		TFOMA and EMA identify the 8th bending mode, while their frequencies are consistent.
O13	Its frequency band is wide while without clear boundaries.	f_{15}=3645 Hz f_{80}=3725 Hz f_{200}=3710 Hz		E10	3720 Hz			0.99	9th bending		Neither TFOMA nor EMA identifies the 9th bending mode, while their mode shapes are similar.
O14	It is more pronounced at higher speeds.	f_{15}=4180 Hz f_{80}=4190 Hz f_{200}=4210 Hz		E11	4160 Hz			0.98	10th bending		TFOMA and EMA identify the 10th bending mode, while their frequencies are consistent.

3.5.2. EMA of the in-situ sleeper

For comparison, we perform hammer tests with the same setup in Figure 3.10. All the four sensors were functional in the tests. We generate impacts at five locations using a big hammer (PCB 086D50) and a small hammer (PCB 086D05). At each location, we repeat the test five times with each hammer. Considering their different excitation frequencies [8], the results of the big and small hammers are used for analyses below 2,000 Hz and above 500 Hz, respectively. The average FRFs are plotted in Figure 3.12, and eleven resonance peaks are identified, labeled as E1~E11. Compared to the sleeper in the test rig, the natural frequencies of the real sleeper are much lower due to its size and material. Most of the resonance peaks, especially at high frequencies, are smooth, which is consistent with the finding in Section 3.4.3. The average frequency and mode shapes for each resonance peak are shown in Table 3.3, where the identified mode shapes deviate for different hammers and impact locations.

3.5.3. Comparisons between TFOMA and EMA

Moreover, we compute the theoretical mode shapes of a free-free beam of length 2.5 m according to Eq. (3.16) and (3.17). Further, in Table 3.3, we match the identified modes of TFOMA with those of EMA and theoretical analysis while referring to the characteristics of sleeper modes reported in [5, 161]. The average *MAC* in Table 3.3 quantifies the consistency of mode shapes between TFOMA and EMA. The main findings are summarized below.

- TFOMA identifies the rigid-body motions of the sleeper at frequencies lower than those of the bending modes, which is consistent with [5, 161]. The bounce motion is more pronounced, which is consistent with the laboratory test. The rigid-body motions are not observed in EMA because the impact forces cannot effectively excite such modes.

- In terms of mode shapes, both TFOMA and EMA consistently (with high *MAC* values) identify the 1st, 2nd, 4th, 5th, 7th, 8th, and 10th bending modes. However, neither identifies the 3rd, 6th, and 9th bending modes, probably because these modes are less dominant or the sensors are close to the nodes.

- The frequencies of E1, E2, and E4 are close to those reported in [5, 161] under unloaded conditions. For the 1st and 2nd bending, the frequencies of TFOMA deviate from those of EMA, reflecting the influence of the train load. For high-order modes, the frequencies of TFOMA and EMA are very close.

- Both TFOMA and EMA identify extra modes probably related to other components.

Furthermore, the pros and cons of TFOMA and EMA are discussed as follows.

- TFOMA can capture the change of modal characteristics over time and frequency, whereas EMA cannot.

- TFOMA works under operational loads in a broad frequency range, but the excitation spectrum is usually not flat, which can cause errors in modal

identification. EMA works under controlled excitations but requires manual impacts and also different hammers for different frequency ranges.

- For a complex coupled system (e.g., a train-track system), the response of a component (e.g., a sleeper) depends not only on its own modal characteristics but also on the dynamical influence of other components (e.g., trains, rails, fasteners, and ballast). As a consequence, extra modes can be more pronounced in OMA than in EMA.

- For each mode, the mode shapes identified by TFOMA spread within a certain variance, while those identified by EMA are sensitive to impact locations and may disappear or be distorted when the impact is close to a node or an edge.

- TFOMA can provide informative results from acceleration measurements of only a few seconds under operational conditions, whereas EMA requires longer experimental time, more workload, and temporary operation shutdowns.

3.6. Discussions

3.6.1. Estimation of damping ratio

This chapter mainly focuses on estimating damped natural frequencies and mode shapes. In this section, the estimation of damping ratios is discussed. First, for the in-situ sleeper in the laboratory tests, the damping ratio of each peak band is obtained while estimating the natural frequencies in Section 3.4.1. Besides, we estimate the damping ratios from the FRFs in Section 3.4.3 using the peak-picking method [162]. Then, for all the matched modes in Section 3.4.4, the estimated damping ratios are plotted against their natural frequencies in Figure 3.13 (a). For most modes, TFOMA in different phases produces damping ratio estimates similar to EMA while underestimating those at low frequencies.
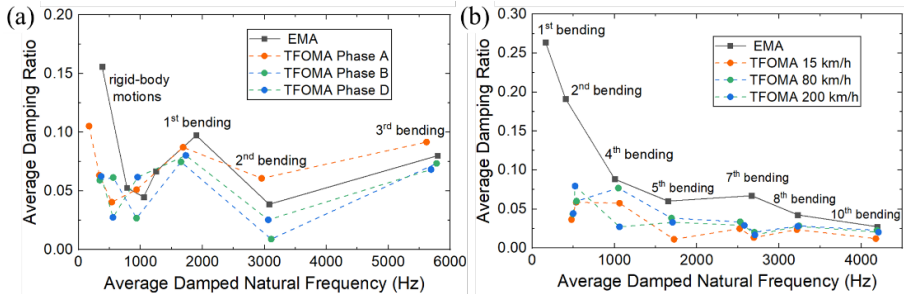
Figure 3.13: Comparison of damping ratio estimation between TFOMA and EMA. (a) Laboratory tests; (b) Field tests.

Similarly, the damping ratios of the sleeper in the field tests are estimated and plotted in Figure 3.13 (b). The results of TFOMA are similar between different speeds, but the estimated damping ratios are lower than those of EMA. These deviations may come from two sources. First, the different loading conditions can lead to different modal characteristics, including damping ratios. This effect is pronounced for railway tracks since the train load is enormous. Second, the estimation based on a truncated spectrum

(either in TFOMA or EMA) can cause errors, especially when the frequency resolution is low or adjacent modes affect each other [83, 85]. In summary, TFOMA can provide accurate damping estimates in cases of well-separated modes, but it needs further improvement to handle structures with significant nonlinearity and dense modes.

3.6.2. IDENTIFICATION OF CLOSELY-SPACED MODES

In this chapter, the proposed method is applied to the modal identification of railway sleepers, where the bending modes of different orders are separated. It has the potential to identify closely-spaced modes by involving multiple non-zero singular values. This section demonstrates such capability using a simulation example. As shown in Figure 3.14 (a), a rectangular plate suspended by springs and dampers vibrates in the x-y plane with three degrees of freedom – x, y, θ. External excitation forces are applied at the upper right corner, and the equations of motion are given as follows.

$$\begin{cases} m\ddot{x} + 2k_x x + 2c_x \dot{x} = P_x \\ m\ddot{y} + 2k_y y + 2c_y \dot{y} = P_y \\ I\ddot{\theta} + 2bk_x \theta + 2ak_y \theta + 2bc_x \dot{\theta} + 2ac_y \dot{\theta} = aP_y - bP_x \end{cases} \tag{3.18}$$

Based on the parameters and excitations defined in Table 3.4, Eq. (3.18) is solved numerically using the Newmark-β method [163] with a time step of 0.2 ms. The bidirectional accelerations of the four edge centers are fed into the TFOMA method with the parameters in Table 3.5. The number of segments n_c=2 is used to distinguish the two translational modes, which are closely spaced since they have equal natural frequencies due to equal stiffness.
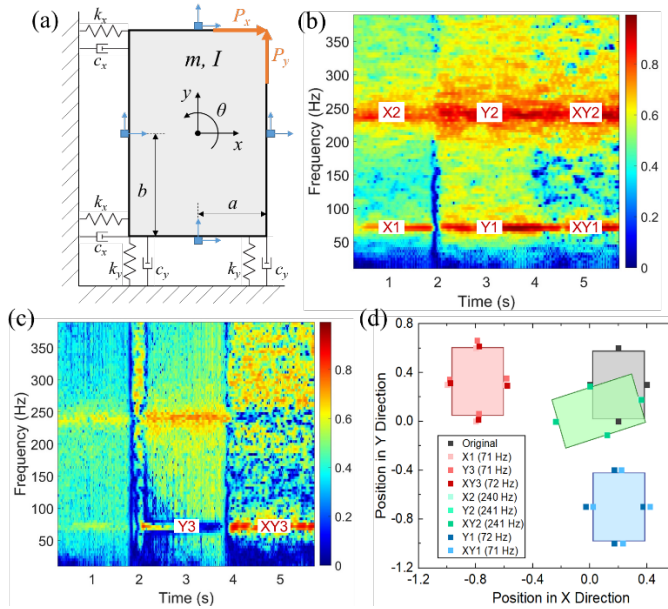

Figure 3.14: TFOMA results of a vibrating plate. (a) Plate model; (b) 1st MI spectrogram; (c) 2nd MI spectrogram; (d) natural frequencies and mode shapes of different peak bands.

Table 3.4: Parameters and excitations of the plate.

Parameters	Values	Parameters	Values
Mass m	1 kg	Moment of inertia I	$m(a^2+b^2)/3$
Half of the width a	0.2 m	Half of the height b	0.3 m
Stiffness k_x, k_y	100 kN/m	Damping c_x, c_y	2 N·s/m
Excitation P_x (0~2 s)	White noise with the power of 10 dBW	Excitation P_y (0~2 s)	0
Excitation P_x (2~4 s)	0	Excitation P_y (2~4 s)	White noise with the power of 20 dBW
Excitation P_x (4~6 s)	White noise with the power of 10 dBW	Excitation P_y (4~6 s)	White noise with the power of 20 dBW

Table 3.5: Selected parameters for the plate.

Parameters	Values	Parameters	Values
Number of segments n_c	2	Segment length n_b	1,250 (0.25 s)
Overlap ratio in PSD estimation α_b	0.5	Overlap ratio in STFDD α_s	0.95
Half kernel size in time a	5	Half kernel size in frequency b	3
Exponent of singular value λ_v	1	Exponent of LMSS λ_l	3
Time resolution Δt	18.75 ms	Frequency resolution Δf	4 Hz

Two MI spectrograms are obtained, as shown in Figure 3.14 (b) and (c), with eight peak bands (with MI>0.8) identified in different phases of the response. The estimated natural frequencies and mode shapes are shown in Figure 3.14 (d). In 0~2 s, the translational mode in the x direction is identified (X1), whereas the one in the y direction is not identified since the excitation is applied only in the x direction. When the excitation is applied only in the y direction in 2~4 s, the translational mode in the y direction is identified (Y1), while the one in the x direction is still identifiable from the decay response (Y3). When the excitations are applied in both directions, the two translational modes are identified (XY1 and XY3), and XY1 (in the 1st spectrogram) is more dominant than XY3 (in the 2nd spectrogram) since the excitation in the y direction has greater power. Moreover, the rotational mode is identified in all three phases (X2, Y2, and XY2). For all modes, the estimated frequencies are consistent with the engine frequencies calculated from the model parameters. The simulation result demonstrates that the proposed method can distinguish closely-spaced modes under nonstationary excitations as long as the modes are effectively excited. We expect the validity of this capability to hold in real scenarios while it remains to be demonstrated.

3.7. CONCLUSIONS

This chapter presents an interpretable OMA method in time-frequency representation. Short-time FDD and a convolution-based strategy are proposed to obtain singular values and local mode shape similarity, respectively, which are further fused into mode indicators by a fuzzy-based strategy. The main conclusions are summarised below.

- TFOMA is an explicit tool that provides not only a global view of modal characteristics but also estimates of modal parameters. Its interpretability is enhanced by including physical information from the user's prior knowledge in selecting parameters and peak bands.

- TFOMA is applicable to strongly nonstationary responses under time-varying loads and conditions and robust to the length of signals due to its discrete and localized nature.

- TFOMA identifies the rigid-body motions and bending modes of the sleepers at frequencies up to 6,500 Hz in the laboratory tests and 4,500 Hz in the field tests. The passage response provides similar results to the impact response, while the pre-passage phase slightly outperforms the post-passage phase. TFOMA works effectively at speeds up to 200 km/h by using only three sensors, and some high-frequency modes are identifiable when the train is 150 m away.

- TFOMA provides identification results comparable to EMA, while their deviations reflect the dynamical influence of train loading and other track components.

3

3

4

SPEED-DEPENDENT CHARACTERISTICS OF TRAIN-BORNE LDV MEASUREMENT

A train-borne laser Doppler vibrometer (LDV) measures the vibration response of railway tracks from a moving train. This chapter proposes a holistic methodology to characterize train-borne LDV measurements by combining computer-aided approaches and real-life measurements. The focus is on the speed-dependent characteristics because the train speed affects the intensity of track vibrations and the intensity of speckle noise, which defines the quality and usability of the measured signals. First, numerical models are established and validated to simulate sleeper vibrations and speckle noise separately. Then, we propose a vibration-noise separation method that can adaptively extract speckle noise and structural vibrations from LDV signals measured at different speeds. The parameters of the separation method are tuned using simulation signals. The method is then validated using laboratory measurements in a vehicle-track test rig and applied to field measurements on a railway track in Rotterdam, The Netherlands. Further, the speed-dependent characteristics of train-borne LDV measurement are determined by analyzing the competition between track vibrations and speckle noise at different speeds. Simulation and measurement results show that an optimal speed range yields the highest signal-to-noise ratio, which varies for different track structures, measurement configurations, and operational conditions. The findings demonstrate the potential of train-borne LDV for large-scale rail infrastructure monitoring.

4.1. Introduction

A running train is a natural source to excite the dynamic response of railway tracks over a broad frequency band. Track vibration measurement enables the dynamic properties of railway tracks to be assessed under operational conditions. A train-borne LDV can measure the vibration of track structures as the train moves. The variation of track vibration and speckle noise with train speed affects the quality and usability of train-borne LDV signals, which further affects the applicability of train-borne LDV technology. To investigate the speed-dependent characteristics of train-borne LDV measurements, this chapter develops a holistic methodology to characterize train-borne LDV measurements and applies it to vibration measurements of railway sleepers.

The methodology of the research is shown in Figure 4.1. In Part 1, numerical models of train-track-LDV dynamics and speckle noise are established and validated with laboratory measurements. This provides insights into the train-borne LDV system prior to field tests and enables sleeper vibrations and speckle noise to be characterized separately without interfering with each other. Since structural vibration and speckle noise are mixed in real-life measurements, Part 2 presents a signal processing method to separate them effectively at different train speeds. The parameters of the separation method are tuned using simulation signals, and the method is then validated with laboratory measurements under well-controlled and well-observed conditions. In Part 3, field measurements of track vibration using a train-borne LDV are performed in Rotterdam, The Netherlands, and the validated separation method is applied to the measured signals. In Part 4, the speed-dependent characteristics are investigated based on the simulations, laboratory, and field measurements. Section 4.2~4.5 of this chapter present Part 1~4, respectively. Conclusions are drawn in Section 4.6, and details of the simulation models are presented in Appendix A.
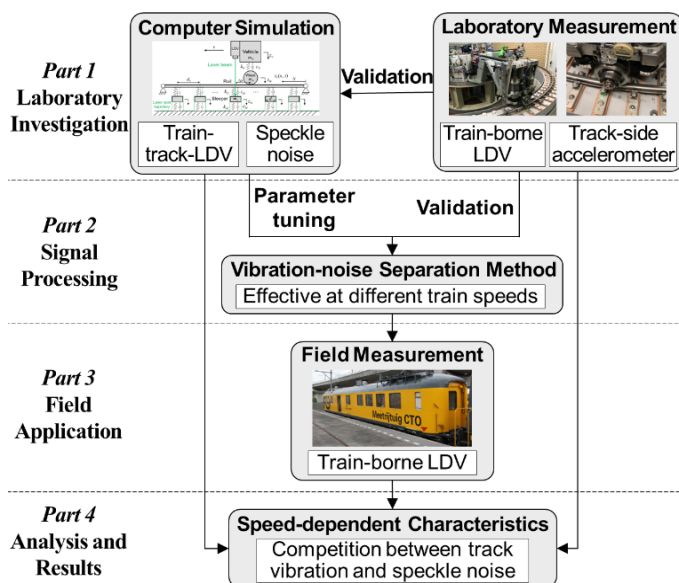

Figure 4.1: Methodology for characterizing train-borne LDV measurements.

4.2. SIMULATION AND VALIDATION

4.2.1. NUMERICAL MODELING

This research first uses modeling and simulation to characterize train-borne LDV measurement and generate signals of track vibration and speckle noise. A vertical train-track-LDV model is built to simulate sleeper vibration measurement using a train-borne LDV, as shown in Figure 4.2. The train is modeled as a quarter vehicle. An LDV is rigidly connected to the vehicle, and its laser spot is targeted onto the track. The track is modeled as a simply-supported Euler-Bernoulli beam discretely supported by sleepers, and the Ritz method is used to characterize the dynamics of the beam [164]. The contact force is calculated based on the Hertz theory considering the vertical irregularity of the rail [164]. All the equations of motion are solved numerically by the Newmark-β method [163], while the contact force is updated at each step.

In Figure 4.2, the laser spot has an offset of Δx from the wheel-rail contact point. Assuming that the vibration of the LDV can be perfectly removed from the LDV signal [165], the ideal vibration of the i-th sleeper measured by the LDV is expressed as follows.

$$\dot{z}(t) = \dot{z}_{si}(t) \quad \text{when } x_{si} - \frac{d}{2} < vt + \Delta x < x_{si} + \frac{d}{2} \tag{4.1}$$

where z_{si} is the displacement of the i-th sleeper, t is the time, d is the sleeper width, v is the vehicle speed, and x_{si} is the position of the i-th sleeper.

Details of the model can be found in Appendix A.1. The model is considered effective and computationally cheap for simulating rigid-body vibrations of sleepers in a multi-layer track structure under a moving train load. Nevertheless, other models, such as finite element models, can also be employed in the proposed methodology.

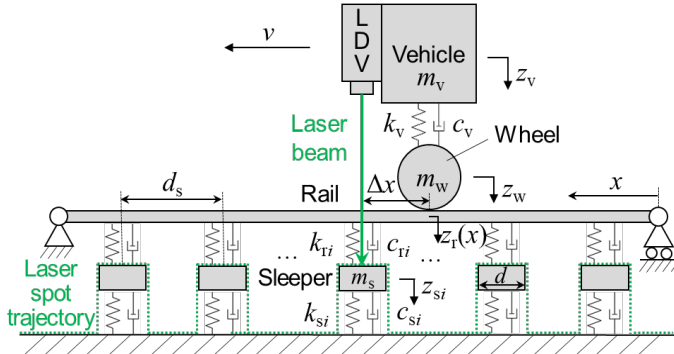Figure 4.2: A train-track-LDV model.

Figure 4.3 (a) shows the working principle of an LDV. A laser beam is projected onto a target surface, and the scattered beam is collected on a photodetector, where speckle patterns inevitably appear [166]. Each speckle is heterodyned with a reference beam, and the intensity of the heterodyned beams is converted into a signal with the following frequency [167].

$$\omega_{\mathrm{D}}(t) = \omega_{\mathrm{R}} + \frac{4\pi}{\lambda}\dot{z}(t) + \frac{d\theta_{\mathrm{M}}}{dt}(t) \tag{4.2}$$

where ω_{R} is an artificial frequency shift, λ is the wavelength of the laser, $\dot{z}(t)$ is the vibration velocity of the target that causes the Doppler frequency shift, and θ_{M} is a phase angle expressed as follows,

$$\theta_{\mathrm{M}} = \arctan\left[\frac{\sum_{k=1}^{K} a_k \sqrt{I_{\mathrm{S}k}} \sin(\theta_{\mathrm{R}} - \theta_{\mathrm{S}k})}{\sum_{k=1}^{K} a_k \sqrt{I_{\mathrm{S}k}} \cos(\theta_{\mathrm{R}} - \theta_{\mathrm{S}k})}\right] \tag{4.3}$$

where K is the total number of speckles, a_k is the area of the k-th speckle on the photodetector, $I_{\mathrm{S}k}$ and $\theta_{\mathrm{S}k}$ are the intensity and phase of the k-th speckle, respectively, and θ_{R} is the phase of the reference beam. According to Eq. (4.2), the speckle noise caused by the phase change rate $d\theta_{\mathrm{M}}/dt$ when measuring $\dot{z}(t)$ is expressed as follows.

$$\xi(t) = \frac{\lambda}{4\pi} \cdot \frac{d\theta_{\mathrm{M}}}{dt}(t) \tag{4.4}$$

For train-borne LDV measurements, speckle translation due to the in-plane motion between the laser spot and the target surface plays a dominant role in $d\theta_{\mathrm{M}}/dt$ [32]. The space and time correlation lengths of the speckles, l_{C} and τ_{C}, are two important parameters depending on the laser properties and measurement setup [168]. The space correlation length l_{C} characterizes the size of each speckle, within which $I_{\mathrm{S}k}$ and $\theta_{\mathrm{S}k}$ are constants following a negative exponential distribution and a uniform distribution, respectively [169]. The time correlation length τ_{C} describes the time length for the speckle pattern to advance by one speckle, which is inversely proportional to v [168].

As shown in Figure 4.3 (b), each speckle is modeled as a square with $m \times n$ grids [170]. A full speckle transition is divided into m partial transitions, and different columns are randomly misaligned along the n grids to account for speckle irregularities. The photodetector is of size $a \cdot l_{\mathrm{C}} \times a \cdot l_{\mathrm{C}}$, and the intensity and phase of the reference beam on the photodetector, I_{R} and θ_{R}, are assumed constant [170]. In the simulation of speckle translation, the photodetector starts from an initial position and moves at the constant speed of $l_{\mathrm{C}}/\tau_{\mathrm{C}}$. At each partial transition, indexed by the j-th step, the overlapping area between the photodetector and each speckle is obtained, and the phase $\theta_{\mathrm{M}}(j)$ is calculated according to Eq. (4.3). Then, the phase change rate at the j-th step is estimated as follows,

$$\frac{d\theta_{\mathrm{M}}}{dt}(j) = \frac{\Delta\theta_{\mathrm{M}}(j)}{\Delta t} = \frac{\theta_{\mathrm{M}}(j) - \theta_{\mathrm{M}}(j-1)}{(\tau_{\mathrm{C}}/m)} \tag{4.5}$$

where $\Delta\theta_{\mathrm{M}}$ should be constrained to be less than $\pi/2$.

Based on the simulated phase change rates, the speckle noise $\xi(t)$ is obtained according to Eq. (4.4). A low-pass finite impulse response filter with cut-off frequency f_{C} is applied to $\xi(t)$ to resemble the signal acquisition process. More details of the model can be found in Appendix A.2.
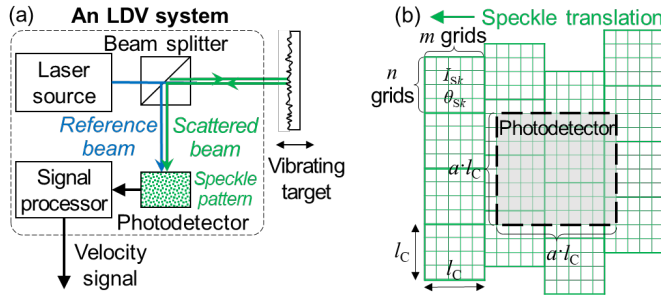
Figure 4.3: (a) Working principle of an LDV. (b) Simulation of speckle translation.

4.2.2. LABORATORY MEASUREMENT

Laboratory measurements play an important role in this research to validate the numerical models and the signal processing method under well-controlled and well-observed conditions. We perform laboratory measurements in the V-Track test rig, as shown in Figure 4.4. The introduction of this test rig and the instrumentation of the LDV can be found in Section 2.2.1. At the same time, the angular position of the beam is measured, which can be used to determine the position of the wheel and the laser spot. Moreover, we install accelerometers (PCB 356B21) on some sleepers to measure their vertical accelerations in response to the passing vehicle. An additional accelerometer is installed on the mirror to capture its effect on the LDV signal. We use the sampling frequency of 102,400 Hz.
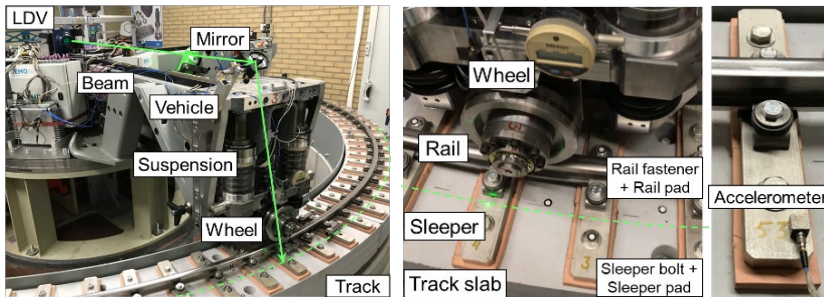
Figure 4.4: V-Track test rig instrumented with an LDV.

4.2.3. MODEL VALIDATION

The parameters for simulating the vehicle-track dynamics are listed in Appendix A.1. We generate the vertical irregularity of the rail by applying a low-pass filter to Gaussian white noise. The spectrum of such artificial spatial noise is smoothly monotonic and maximally flat in the passband. Though it may not perfectly replicate the track geometry in V-Track, it resembles the decay pattern of real-life track irregularity spectrum and enables the dynamic wheel-rail force to cover a wide range of frequencies.

We validate the track dynamics model using the trackside accelerometer measurements in V-Track. Figure 4.5 shows the vibrations of the center sleeper simulated at two different vehicle speeds. The trackside measurements are compared with the simulation results after conversion from acceleration to velocity through

frequency-domain integration [144]. It can be seen that the amplitude and frequency of the sleeper vibration are larger at a higher speed. The simulation results are similar to the measurements in both time and frequency domains, but their amplitudes do not exactly match, especially at the higher speed, mainly due to the simplification of the model and the rail irregularity. Despite such differences, the model is considered applicable for characterizing the rigid-body vibration of the sleepers under the wheel passage. Using a more complex train-track model and a more accurate rail irregularity spectrum can potentially provide a better match between simulations and measurements. This requires more effort for modeling and parameter tuning, which is not the focus of this dissertation.

Figure 4.5: Comparison in sleeper vibrations between simulations and measurements. (a) Vehicle speed 2 km/h; (b) Vehicle speed 12 km/h.
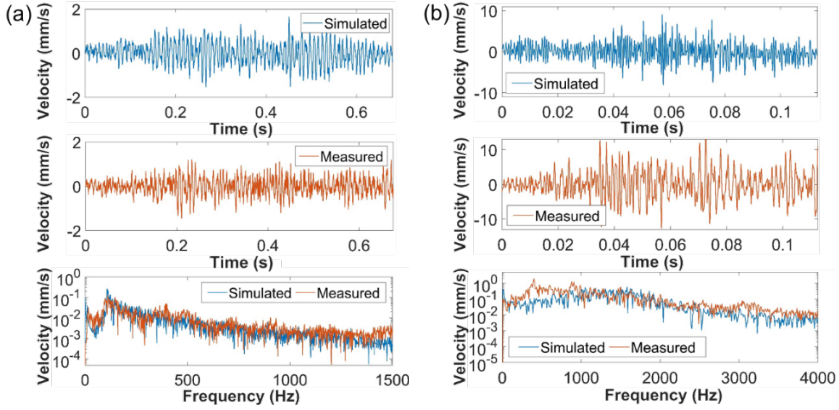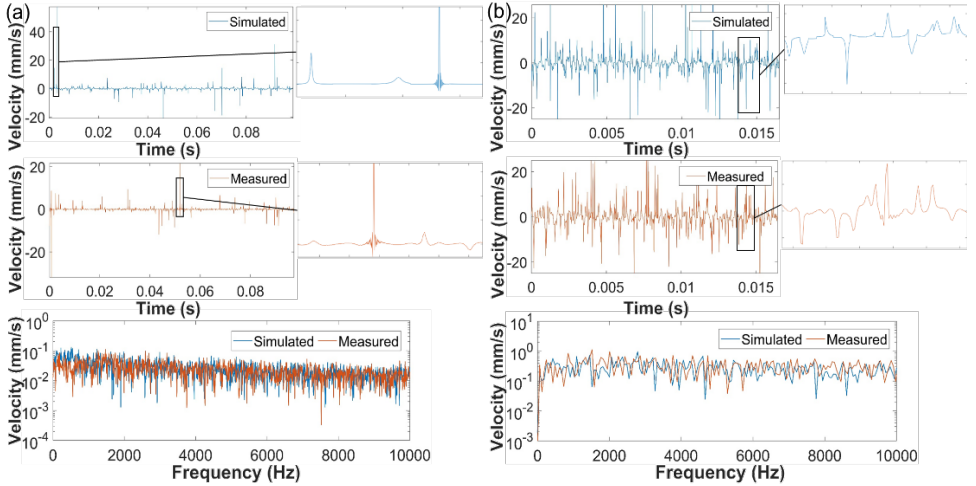
Figure 4.6: Comparison in speckle noise between simulations and measurements. (a) Vehicle speed 2 km/h; (b) Vehicle speed 12 km/h.

We validate the speckle translation model using speckle noise separated from LDV signals in laboratory measurements (the separation method will be introduced in Section

[4.3](#)). The simulation parameters are listed in Appendix [A.2](#), and the simulated speckle noise at two vehicle speeds is compared with the measurements in Figure [4.6](#). It can be seen that, at a higher speed, spikes appear more frequently with greater amplitudes and shorter durations. The simulated speckle noise behaves similarly to the measurements in terms of the interval, amplitude, and duration of spikes. Meanwhile, good consistency can be observed over a wide frequency range. It should be noted that the simulation cannot exactly replicate the measurement due to the extreme randomness of speckle patterns. Instead, the statistical agreement between them at different speeds demonstrates the effectiveness of the established model in reproducing the speckle noise.

4.3. Vibration-noise Separation

4.3.1. A speed-adaptive method

In real-life measurements, structural vibration and speckle noise are mixed. Thus, effective signal processing is needed to separate them. As introduced in Section [1.2.3](#), no existing method can achieve this adaptively at different speeds. In Chapter [2](#), spikes are first distinguished through a wavelet-based detection method. Then, the detected spikes are replaced with estimates through an autoregressive integrated moving average (ARIMA)-based imputation method. Finally, the residual noise is filtered out using a band-pass filter. However, the selected parameters of this method vary at different speeds due to the speed-dependent characteristics of spikes. To address this problem, we adapt the method to extract speckle noise and target vibration without the need to adjust its parameters for different speeds.

Step 1. Perform one-level discrete Haar wavelet decomposition and reconstruction to a raw LDV signal $x_0(t)$ and calculate spike indicators $R_d(t)$ as follows,

$$cD_1(t) = \mathrm{DWT_D}\big[x_0(t)\big] \tag{4.6}$$

$$R_d(t) = \big|\mathrm{IDWT_D}\big[cD_1(t)\big]\big| \tag{4.7}$$

where $\mathrm{DWT_D}[\cdot]$ and $\mathrm{IDWT_D}[\cdot]$ represent forward and inverse discrete wavelet transforms, respectively, and $cD_1(t)$ is the detail coefficients. Then, find $P\%$ locations in $x_0(t)$ with the largest spike indicators $R_d(t)$ and label them as large spikes.

Step 2. Define an ARIMA model with an autoregressive order p_A, a moving average order q_A, and a differencing order d_A, denoted as ARIMA(p_A, d_A, q_A). Train the ARIMA model with $x_0(t)$ along the forward direction, and replace the labeled points sequentially with predictions from the ARIMA model. Repeat the above training and replacement process along the backward direction. Then, average the forward and backward replacements to obtain the imputed signal $x_1(t)$. The noise component (large spikes) is $\xi_1(t) = x_0(t) - x_1(t)$.

Step 3. Apply a band-pass filter (with the cut-off frequency of f_L and f_H) and a high-pass filter (with the same cut-off frequency f_H) to $x_1(t)$, resulting in the target vibration $x_2(t)$ and the noise component (small spikes) $\xi_2(t)$. Finally, superpose $\xi_1(t)$ with $\xi_2(t)$ as the total noise $\xi(t) = \xi_1(t) + \xi_2(t)$.

The above separation method is illustrated in Figure 4.7. Step 1~2 aim to extract $P\%$ most influential points (large spikes) from $x_0(t)$ into $\xi_1(t)$, which are usually dominant over a broad frequency range and easier to be separated through time-domain analysis. Specifically, Step 1 calculates spike indicators $R_d(t)$ that represent the noise component in $x_0(t)$ and then labels $P\%$ data points based on their $R_d(t)$. Step 2 then replaces the labeled spikes with predictions from the ARIMA models and takes the difference between the imputed signal $x_1(t)$ and the original signal $x_0(t)$ as the large spikes $\xi_1(t)$. However, changes in train speed lead to changes in spike characteristics. If the actual percentage of large spikes is lower than $P\%$, e.g., when the train speed is low, normal data points may be labeled as spikes in Step 1. These points are then replaced in Step 2 by predictions with similar amplitude, thus not affecting $\xi_1(t)$ significantly. If the actual percentage of large spikes is higher than $P\%$, e.g., when the train speed is high, some less influential spikes may be retained in $x_1(t)$. Since small spikes are usually at high frequencies, they are filtered out through frequency-domain analysis and then included in $\xi_2(t)$ in Step 3. By combining $\xi_1(t)$ with $\xi_2(t)$, speckle noise is eventually obtained.

The effectiveness of the separation method at various speeds requires a proper selection of its parameters. The most important is the proportion of labeled spikes $P\%$ in Step 1, which affects the labeling of spikes and the number of replacements. The orders of the ARIMA model (p_A, d_A, q_A) affect the performance of imputation in Step 2. According to Section 2.3.2, we recommend setting $d_A=1$ and $q_A=1$ since they provide good results at different speeds. The parameters $P\%$ and p_A should be tuned considering the separation performance and the computational cost at different speeds. This can be achieved either quantitatively based on simulated signals or qualitatively through trial and observation based on measured signals. Moreover, the cut-off frequencies f_L and f_H in Step 3 are important for separating structural vibrations from residual noise. We recommend setting them to the lowest and highest frequencies of interest for the target structural vibration, respectively. Procedurally, f_L and f_H can be defined before or after applying Step 1 and 2.
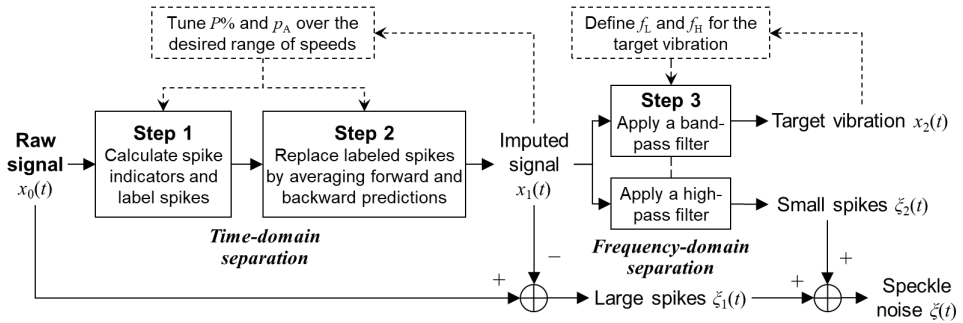

Figure 4.7: Flowchart of the vibration-noise separation method.

4.3.2. PARAMETER TUNING WITH SIMULATIONS

The simulation models in Section 4.2 can generate signals of track vibration and speckle noise at different speeds, which makes it possible to quantify the performance of the separation method and tune its parameters. For each sleeper under a certain vehicle speed,

the simulated train-borne LDV signal is obtained by superposing the simulated sleeper vibration with the simulated speckle noise. Then, we apply the proposed separation method to the superposed signal and compare the separated vibration and noise components with the original vibration and noise signals, respectively. The root-mean-square (RMS) errors and the Pearson correlation coefficient between the separated components and the original signals are calculated to quantify their deviations.

Figure 4.8 shows the separation performance for a single sleeper using different $P\%$ in Step 1. "Raw signal" represents the result without vibration-noise separation, which yields the largest error and the lowest correlation. "Direct filtering" represents applying solely the filter in Step 3 to the raw signal, which separates some noise in the frequency domain. In cases of $P\%>0$, the involvement of the time-domain separation in Step 1 and 2 further improves the performance, and $P\%$ in the range of 10~40% provides low separation errors and high correlation coefficients for both the vibration and the noise at different speeds. When $P\%$ is too small, large spikes cannot be effectively extracted in Step 1, so the errors are large. When $P\%$ is too large, too many points need to be replaced, resulting in large imputation errors.
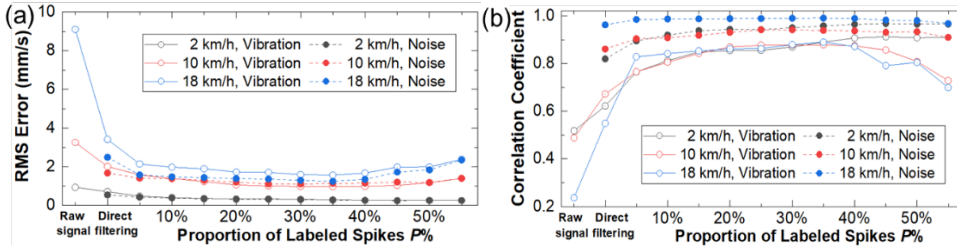

Figure 4.8: Separation performance with different $P\%$ (p_A=20, d_A=1, q_A=1, f_L=0 Hz, f_H=2,000 Hz). (a) RMS errors; (b) Correlation coefficient.
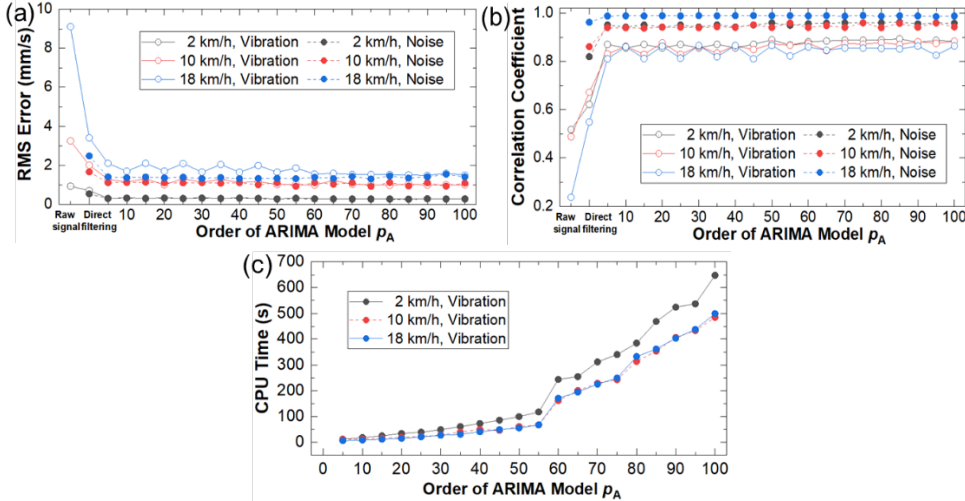

Figure 4.9: Separation performance with different p_A ($P\%$=25%, d_A=1, q_A=1, f_L=0 Hz, f_H=2,000 Hz). (a) RMS errors; (b) Correlation coefficient; (c) CPU time (on Intel Xeon E5-2643 with 32 GB RAM).
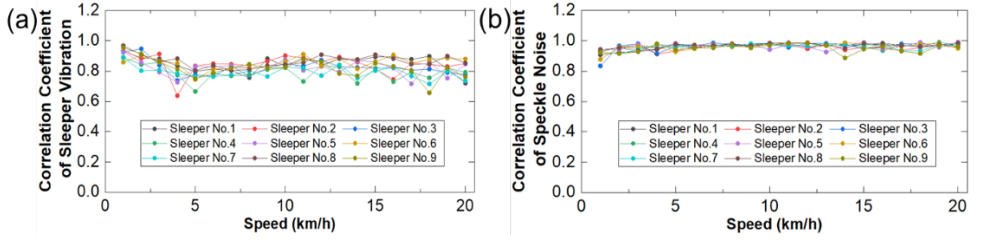
Figure 4.10: Separation performance at different speeds ($P\%$=25%, p_A=20, d_A=1, q_A=1, f_L=0 Hz, f_H=2,000 Hz). (a) Sleeper vibration; (b) Speckle noise.

A similar analysis is performed for the order p_A in Step 2, as shown in Figure 4.9. It can be seen that the root mean square (RMS) error and correlation coefficient are not sensitive to p_A as long as p_A>5. However, p_A significantly affects the computational cost, and the higher the p_A, the longer the CPU time.

In this chapter, we use $P\%$=25% and p_A=20 as a balance between the separation performance and the computational cost. Figure 4.10 plots the separation results for nine sleepers simulated at different speeds. It shows that the separated vibration and noise components are highly correlated with the original signals. Such a high correlation holds at different speeds, and the deviation between the different sleepers is small. This demonstrates the effectiveness of the separation method at different train speeds.

4.3.3. VALIDATION WITH LABORATORY MEASUREMENTS

In this section, we validate the separation method with measurements in V-Track. We use the same parameters in Step 1 and 2 as in Section 4.3.2 ($P\%$=25%, p_A=20, d_A=1, q_A=1). In Step 3, we use f_L=50 Hz to eliminate the effect of the mirror vibration and f_H=1,500 Hz to capture the rigid-body motion of the sleepers, according to Section 3.4. The separation results for a typical sleeper at different speeds are shown in Figure 4.11~4.13. As the speed increases, the signal length becomes shorter, and the frequency resolution becomes lower. By comparing the raw and imputed signals, it can be seen that large spikes are separated after Step 1 and 2, while the small spikes remain to be separated in Step 3. Additionally, the mirror vibration dominates at the low frequencies and is filtered out in Step 3.
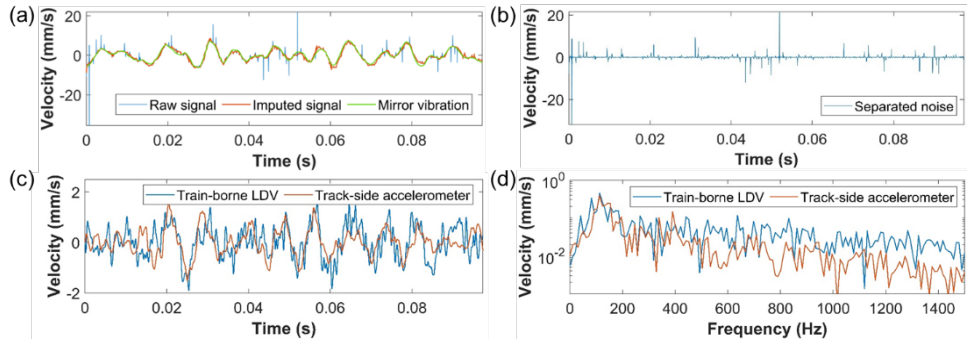

Figure 4.11: Separation result at 2 km/h. (a) Imputed signal; (b) Separated noise; (c) Comparison in the time domain; (d) Comparison in the frequency domain.
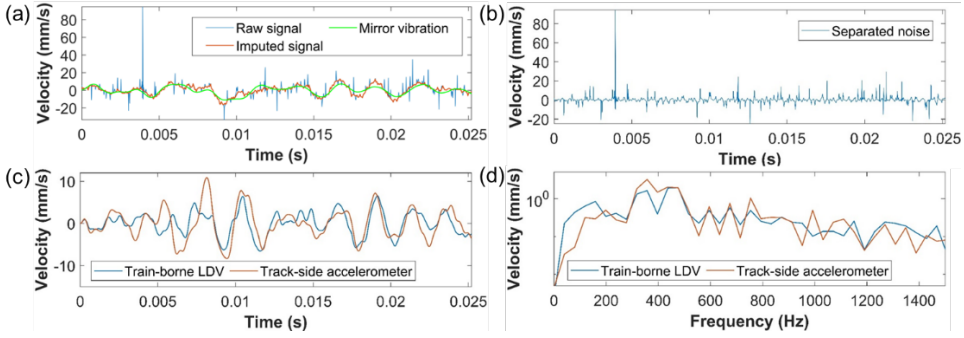
Figure 4.12: Separation result at 8 km/h. (a) Imputed signal; (b) Separated noise; (c) Comparison in the time domain; (d) Comparison in the frequency domain.
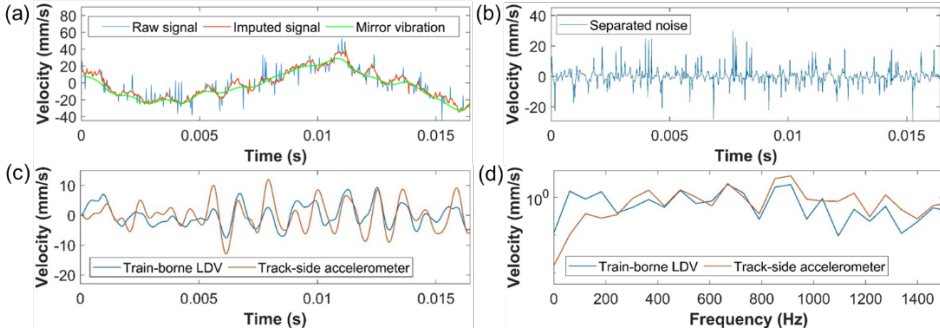

Figure 4.13: Separation result at 12 km/h. (a) Imputed signal; (b) Separated noise; (c) Comparison in the time domain; (d) Comparison in the frequency domain.

Generally, the separated noise is very close to that in the raw signals. Meanwhile, the sleeper vibrations separated from the train-borne LDV signals are consistent with those measured by the trackside accelerometer in both time and frequency domains. These results demonstrate the measuring capability of the train-borne LDV and the effectiveness of the proposed method at different speeds. Some residual noise can be noticed in the separated sleeper vibration, which is less pronounced at higher speeds due to increased vibration amplitude and frequency. The deviations between the train-borne LDV signals and the trackside accelerometer signals are caused by imperfect separation and the spatial deviations between the laser spot and the accelerometers.

4.4. APPLICATION TO FIELD MEASUREMENT

Since the above simulations and laboratory measurements represent scaled and simplified vehicle-track systems, field measurements are necessary to further test the train-borne LDV technology and the vibration-noise separation method in the real world. We test the train-borne LDV technology on the CTO measurement train of TU Delft, as shown in Figure 4.14. The same LDV (Polytec RSV-150) is installed in the cabin, and its laser beam is targeted at sleepers (and ballast) through a hole in the cabin floor. Two accelerometers (PCB 356B21) are installed on the LDV to measure its vibration, and a video camera is used to record the trajectory of the laser spot on track structures. The

wheel-laser offset is around 1.2 m. We use the sampling rates of 102,400 Hz for the LDV and accelerometers and 240 fps for the camera. Since the vibration signals and the video are stored separately, they are synchronized before further analysis.

We conduct the measurements on an operational railway track in Rotterdam, The Netherlands, as shown in Figure 4.15. It is a typical ballasted track with concrete sleepers. The CTO train is pulled by a locomotive connected to the LDV side. We focus on measurements at speeds below 30 km/h since higher speeds cause more significant motion blur, which induces more challenges in accurately positioning the laser spot on each individual sleeper. Figure 4.16 shows the results measured in two typical sections. The upper plots show the change in train speeds with respect to sleeper numbers, in which the speed is estimated by assuming a uniform sleeper spacing. The LDV signal is cut into segments for each sleeper, and the vibration-noise separation method (with the same parameters in Step 1 and 2 as in Section 4.3.2 and 4.3.3) is applied to each segment. The lower plots show by a colored strip the Fourier spectrum of the imputed signal (after Step 1 and 2) for each sleeper. We can see that the amplitude and dominant frequency of the sleeper vibration increase with the increase in speed. A higher speed generates more excitations at higher frequencies, thus leading to larger vibration responses at higher frequencies.
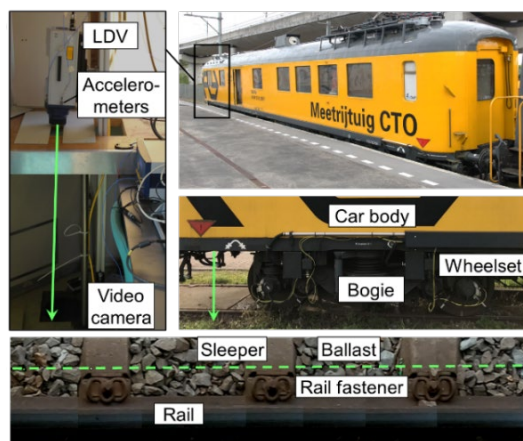

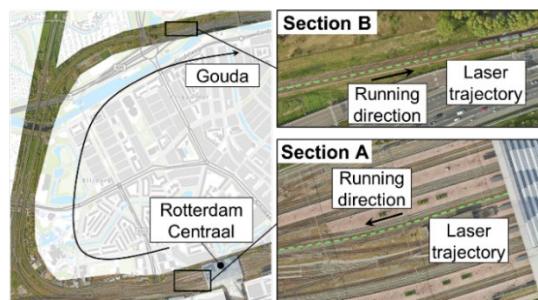Figure 4.14: CTO measurement train instrumented with an LDV.

Figure 4.15: Train route and two selected sections. (Source of aerial photographs: GeoInformatie Portaal of ProRail https://maps.prorail.nl/)

Figure 4.16 shows that the dominant frequency of the sleeper vibration is generally below 300 Hz. This is consistent with the frequency range of rigid-body motions and first-order bending of in-situ sleepers in Section 3.5 and [8]. Therefore, we use f_H=300 Hz in Step 3. It is noteworthy that f_H differs significantly between the field and laboratory measurements due to the different natural frequencies of the sleepers. Additionally, we use f_L=80 Hz to eliminate the influence of the LDV vibration.

Three sleepers are further selected to showcase the vibration-noise separation performance, as plotted in Figure 4.17~4.19. Sleeper ① is measured at 6 km/h, where the LDV vibration dominates the raw signal and the amplitude of the extracted sleeper vibration is small. Sleeper ② and ③ are measured at 21 km/h, and the amplitude and dominant frequency of the sleeper vibration are significantly higher than those of the LDV vibration. Meanwhile, the amplitudes of the extracted sleeper vibration and speckle noise are larger than those of Sleeper ①. In general, the proposed separation method effectively reduces the speckle noise in the raw signals and captures the dominant sleeper vibrations at different speeds.

It is worth noting that the same parameters in Step 1 and 2 work effectively under different scenarios, including simulations (up to 12 km/h), laboratory measurements (up to 12 km/h), and field measurements (up to 30 km/h). In addition, the performance is not sensitive to the variation in signal length due to the variation in speed. This reflects the generalization capability of the proposed method, at least under the tested speeds.
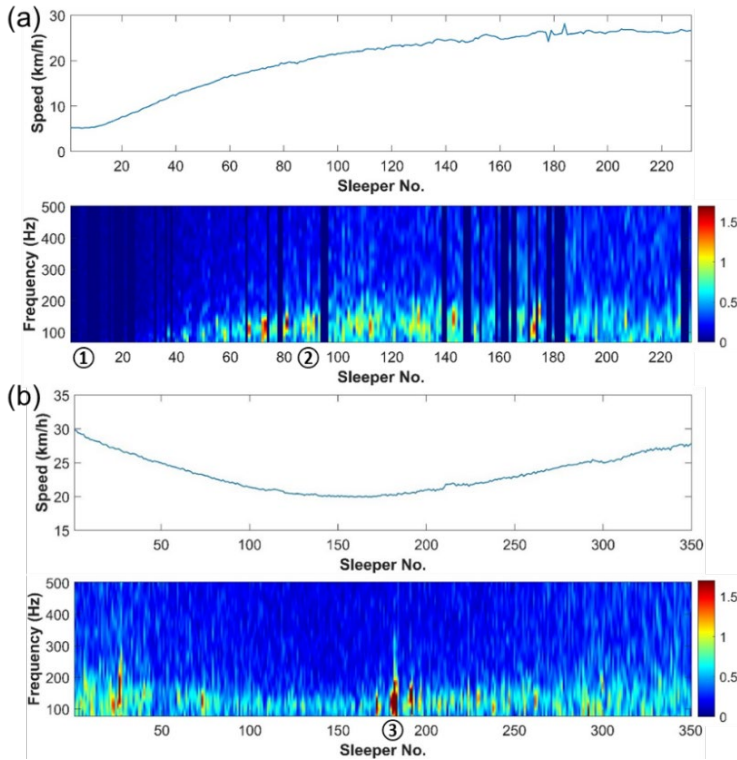
Figure 4.16: Train speed and spectrum of imputed signal for each sleeper. (a) Section A; (b) Section B.
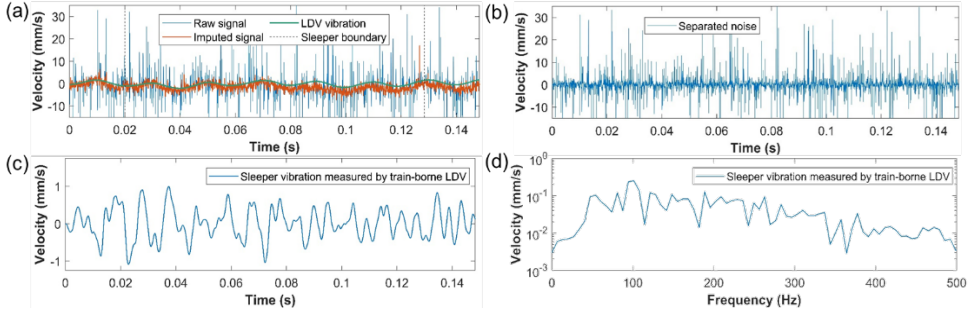
Figure 4.17: Separation result of Sample ①. (a) Imputed signal; (b) Separated noise; (c) Sleeper vibration in the time domain; (d) Sleeper vibration in the frequency domain.
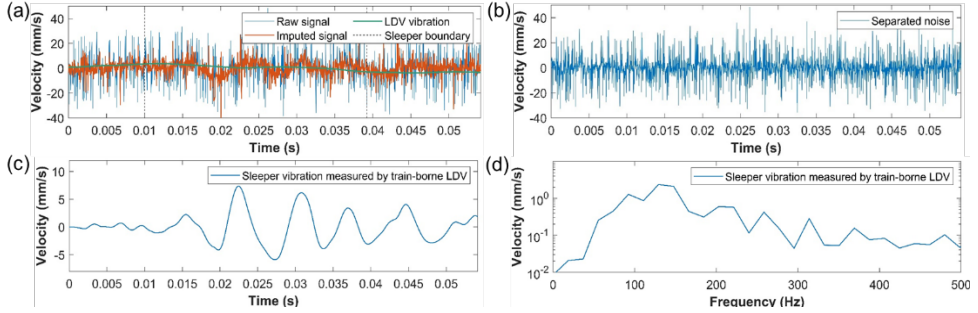
Figure 4.18: Separation result of Sample ②. (a) Imputed signal; (b) Separated noise; (c) Sleeper vibration in the time domain; (d) Sleeper vibration in the frequency domain.
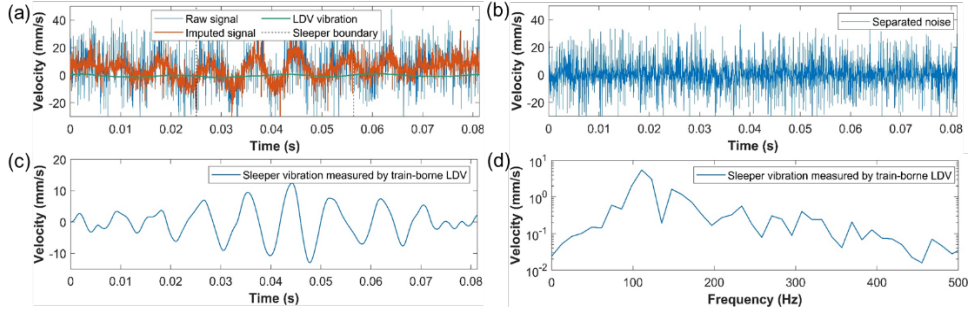
Figure 4.19: Separation result of Sample ③. (a) Imputed signal; (b) Separated noise; (c) Sleeper vibration in the time domain; (d) Sleeper vibration in the frequency domain.

4.5. Speed-dependent Characteristics

Signal-to-noise ratio (SNR) is a key indicator representing the quality and usability of a measured signal. It quantifies how pronounced the real vibration is with respect to the noise, calculated based on their RMS values as follows.

$$SNR = 20\log_{10}\left(\frac{\text{RMS}(\dot{z}(t))}{\text{RMS}(\xi(t))}\right) \tag{4.8}$$

To investigate the influence of train speed on track vibrations and speckle noise and further on the SNR of train-borne LDV measurements, we evaluate the SNRs at different speeds through simulations, laboratory measurements, and field measurements. In the simulation scenario, sleeper vibrations and speckle noise are simulated separately, so the SNRs can be accurately obtained. For the laboratory and field measurements, sleeper vibrations and speckle noise are separated from the LDV signals using the method in Section 4.3, and the SNRs can only be an estimation.

4.5.1. SIMULATIONS

In the simulation study, we assume the stiffness and damping of rail pads and ballast follow Gaussian distributions as a consideration of uncertainties in the track properties. For each parameter, the mean is its nominal value, and the standard deviation is 5% of the nominal value. Random numbers following these distributions are generated for each sleeper. Figure 4.20 (a) shows the simulation results for the nine sleepers in the middle of the track, in which the RMS value is calculated based on the response of each sleeper when the wheel is within ±1.5 sleeper spacing from it. As the speed increases, the sleeper vibration becomes larger, with the slope first increasing and then decreasing, and the deviation between different sleepers also becomes larger. Figure 4.20 (c) shows the response of the center sleeper at 2 km/h, in which the train-borne LDV captures only a fragment of the response under the wheel passage. According to Eq. (4.1), the higher the speed, the shorter the fragment. Figure 4.20 (b) shows the RMS values of the fragments measured on the nine sleepers. The measured sleeper vibrations increase with speed, following the same trend as in Figure 4.20 (a), but the deviation between sleepers is more pronounced, reflecting larger uncertainties due to the shorter length of the measured sleeper response.
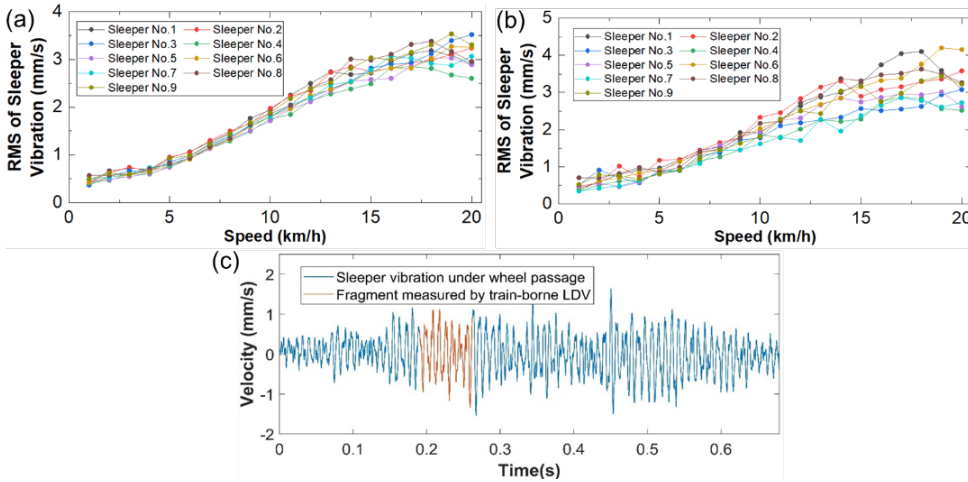

Figure 4.20: Speed-dependent characteristics of simulated sleeper vibrations. (a) Sleeper responses under wheel passage; (b) Fragments measured by the train-borne LDV; (c) An example at 2 km/h.
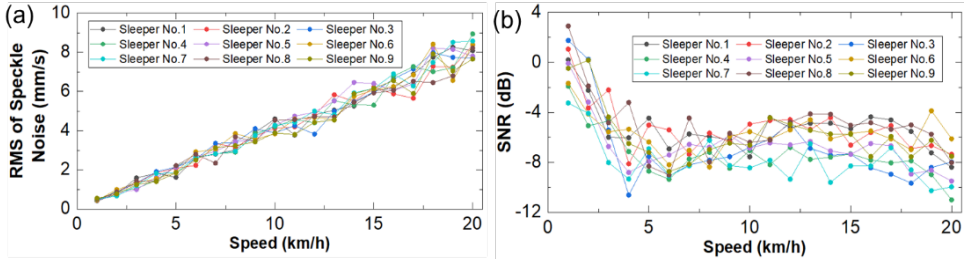
Figure 4.21: Speed-dependent characteristics of simulated speckle noise and SNR. (a) Speckle noise; (b) SNR.

Then, nine simulations of speckle translation are performed at each speed, corresponding to the measurements on the nine sleepers. The results in Figure 4.21 (a) show that the RMS value of the speckle noise increases almost linearly with the increasing speed while its deviation becomes larger. Further, the SNR is calculated for each sleeper, as shown in Figure 4.21 (b). A significant nonlinear behavior can be observed as a result of the competition between the linear increase of the speckle noise and the nonlinear increase of the track vibration with respect to the increasing speed. At low speeds, the sleeper vibration is too small while the speckle noise increases faster, so the SNR first decreases and reaches a local minimum at around 4 km/h. Then, as the sleeper vibration increases more steeply than the speckle noise, the SNR starts to increase and reaches a local maximum at around 10~15 km/h. Further, as the sleeper vibration increases more slowly, the SNR drops gradually as the speed increases.

4.5.2. LABORATORY MEASUREMENT

We apply the vibration-noise separation method to measurements in V-Track at different running laps and calculate the RMS values of the separated vibration, speckle noise, and the corresponding SNR for each sleeper (excluding those near the joints). Figure 4.22 shows their box plot distributions at different speeds. It can be seen from the data points and their percentiles that the sleeper vibration and speckle noise exhibit more significant deviations between sleepers than the simulation results in Figure 4.20 (b). Such deviation is caused by the uncertainties in sleeper dynamics, track geometry, and laser speckle and becomes more pronounced as the speed increases.

Despite the uncertainties, the mean, median, and percentiles in Figure 4.22 (a) show that as the speed increases, the sleeper vibration increases with larger slopes between 4~10 km/h. The measured RMS values are close to the simulation result in Figure 4.20 (b). Meanwhile, Figure 4.22 (b) shows that the speckle noise increases almost linearly with speed, which is consistent with the simulation result in Figure 4.21 (a). These agreements reflect that the established models effectively characterize the track dynamics and the speckle noise in V-Track.

Further, Figure 4.22 (c) shows that, as the speed increases, the SNR first increases (2~6 km/h), becomes flat (6~10 km/h), and then decreases slightly (10~12 km/h). This result is similar to the simulated trend above 4 km/h in Figure 4.21 (b), while deviation occurs at 2 km/h because the RMS values are relatively small and the SNR is sensitive to slight deviations between simulations and measurements.
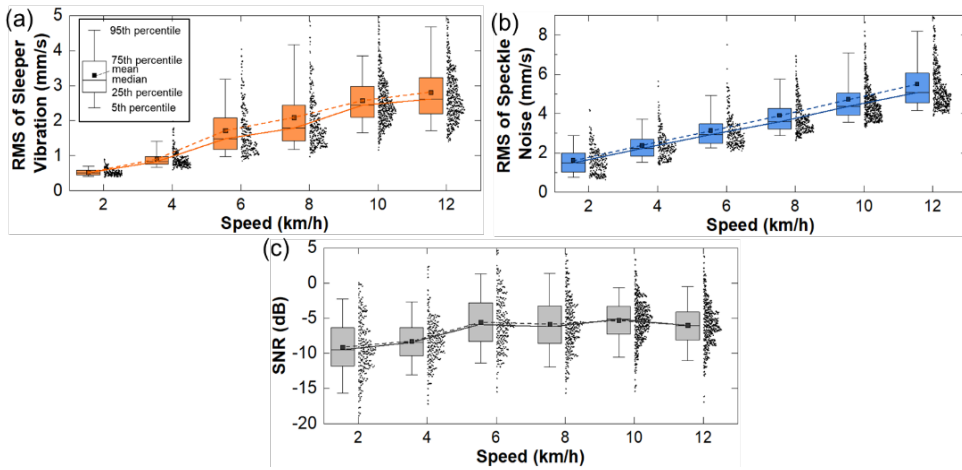
Figure 4.22: Speed-dependent characteristics in laboratory measurements. (a) Sleeper vibrations; (b) Speckle noise; (c) SNRs.

4.5.3. FIELD MEASUREMENT

In the field measurements, considering the possible error in synchronizing the LDV signal with the laser spot position, we cut the measured signal into overlapped segments with different offsets from the estimated center of each sleeper, as shown in Figure 4.23. Then, for each segment, we apply the vibration-noise separation method, calculate the RMS values of the sleeper vibration and speckle noise, and calculate the corresponding SNR. Finally, we take the weighted average of the results from different segments for each sleeper. The weights follow the shape of a Gaussian distribution and decrease toward zero as the segment offsets from the estimated center to the adjacent sleepers.

The results for all the 580 sleepers in Figure 4.16 are plotted in Figure 4.24. It shows trends similar to the simulation and laboratory measurement results in Figure 4.20~4.22. As the speed increases, the sleeper vibration increases first slowly (5~10 km/h), then rapidly (10~20 km/h), then slowly again and even drops slightly (20~30 km/h). Meanwhile, the speckle noise amplitude increases almost linearly with respect to the speed. As a consequence of the competition between the sleeper vibration and the speckle noise, the SNR first drops slightly to reach a local minimum at 7 km/h, then increases to reach a local maximum at 20 km/h, and then drops gradually. Within the speed range investigated, the speed of 15~25 km/h provides a higher SNR than others. The similarity between the simulation, laboratory measurement, and field measurement results demonstrates that the proposed methodology effectively characterizes the speed-dependent characteristics of train-borne LDV measurements.

Nevertheless, it should be noted that the change of SNR with respect to speed depends on the characteristics of sleeper dynamics and speckle noise. Therefore, the optimal speed with the highest SNR varies for different tack structures, measurement configurations, and operational conditions.
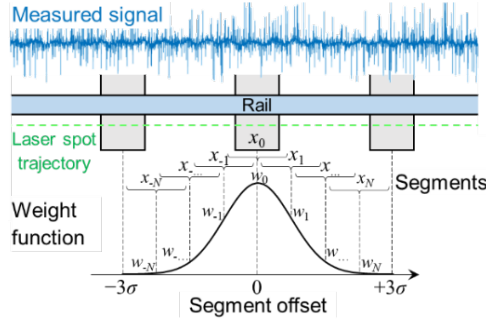
Figure 4.23: Weight assignment for segments with different offsets.
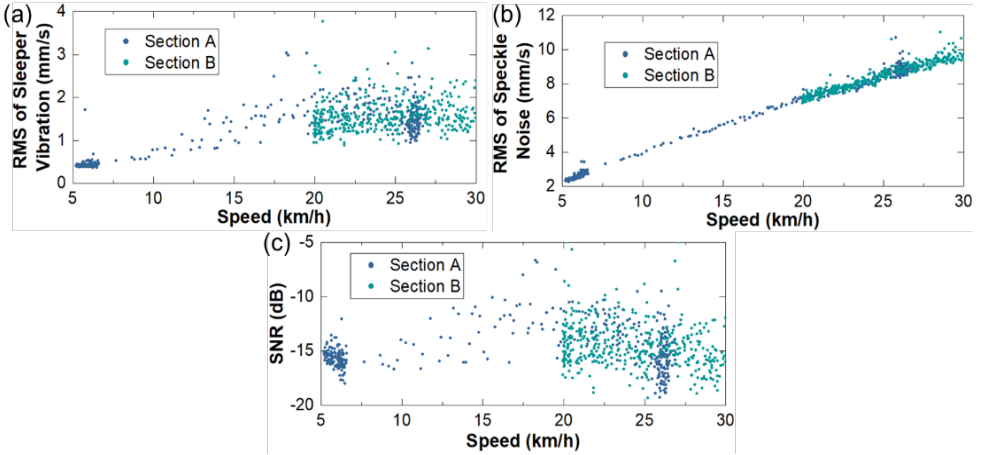
Figure 4.24: Speed-dependent characteristics in field measurements. (a) Sleeper vibrations; (b) Speckle noise; (c) SNRs.

4.6. CONCLUSIONS

This chapter proposes and applies a holistic methodology to characterize train-borne LDV measurements for sleeper vibrations and investigate their speed-dependent characteristics. Validated numerical models are used to separately simulate sleeper vibrations and speckle noise at different speeds and support the parameter tuning of the developed vibration-noise separation method. The method is then validated with laboratory measurements and applied to field measurements at different speeds. The dependence of sleeper vibration, speckle noise, and SNR on train speed is determined using simulations and measurements. The results demonstrate the potential of train-borne LDV to be applied to large-scale rail infrastructure monitoring and also provide us with deeper insights into the quality and usability of signals measured at different speeds. The main conclusions are summarized below.

- The established train-track-LDV model and speckle translation model reproduce the sleeper vibrations and speckle noise in V-Track at different vehicle speeds.

- The vibration-noise separation method extracts speckle noise by first capturing large spikes in the time domain and then filtering out the remaining small spikes in the frequency domain. It can work adaptively at different speeds and robustly under different scenarios and has the potential to be adapted for other different kinds of LDV measurements.

- There are significant uncertainties in sleeper vibrations and speckle noise, which increase with the increase in train speed.

- The RMS value of speckle noise increases almost linearly with speed, whereas the RMS value of sleeper vibration increases nonlinearly with speed. Their competition leads to the nonlinear behavior of SNR with respect to train speed. An optimal speed range yields the highest SNR and varies for different tack structures, measurement configurations, and operational conditions.

4

4

5

ESTIMATING RAILWAY TRACK TRANSFER FUNCTION ON A MOVING VEHICLE

In view of the gaps in measuring transfer functions (TFs) of railway tracks, we propose a methodology to estimate railway track TFs over a wide frequency range from a moving vehicle. Accelerometers are employed to estimate the dynamic train load to railway tracks, and a laser Doppler vibrometer (LDV) is used to scan railway tracks and measure their vibration response as the vehicle moves. First, operational modal analysis is applied to vehicle impact response over a joint to identify its modal parameters, which support the estimation of dynamic wheel-rail forces from vehicle vibrations. This combination eliminates the need to pre-define the vehicle stiffness, vehicle damping, and vehicle body mass and enables the vehicle modal parameters to be updated under operational conditions. Meanwhile, a speed-adaptive despeckle and compensation method is applied to LDV signals to reduce speckle noise and extract track vibrations. Then, a continuous railway structure is segmented into distributed sections, and a TF is estimated for each track section using the estimated wheel-rail force as input and the measured track vibration as output. We validate the proposed methodology in a vehicle-track test rig in our laboratory and test its performance on different track sections (with or without joints) and at different speeds (from 8 km/h to 16 km/h). The results are further compared with trackside measurements and hammer tests. We demonstrate that the track vibrations extracted from the LDV signals are consistent with those measured by trackside accelerometers. The TF estimates from the LDV and accelerometer measurements are close to the frequency response functions measured from hammer tests at 200~800 Hz. The developed system captures differences in the resonance frequencies of the TFs between different track sections, suggesting its potential to be used for structural health monitoring of railway tracks.

5.1. INTRODUCTION

To tackle the research challenges in train-borne measurement of railway track transfer functions (TFs), this chapter develops a railway track TF measurement system in the V-Track test rig. The system consists of an LDV and accelerometers on a moving vehicle. We estimate a single-input single-output TF for each track section using the vertical wheel-rail force as the input and the vertical track vibration as the output. The proposed methodology is validated in the test rig at different locations along the track and at different speeds through comparisons with trackside measurements and hammer tests.

The remainder of this chapter is organized as follows. Section 5.2 presents the methodology for estimating railway track TFs using LDV and accelerometer measurement. Section 5.3 conducts experiments in the V-Track test rig to validate the proposed methodology. Section 5.4 concludes this chapter.

5.2. METHODOLOGY

Figure 5.1 shows the proposed methodology for estimating railway track TFs using LDV and accelerometer measurement on a moving vehicle. Accelerometers are mounted on the main masses of the vehicle, and the laser spot of the LDV can be targeted at track components of interest, such as rails or sleepers. First, the impact response of the vehicle when passing over a joint is captured from the accelerometer measurement and then used to identify the modal parameters of the vehicle (natural frequencies, damping ratios, mode shape vectors, and modal masses). Based on these parameters, the dynamic wheel-rail force is then estimated from vehicle vibrations during vehicle running, denoted as $w(t)$, with t denoting time. Meanwhile, the vibration of railway tracks is extracted from the LDV measurement by compensating for the effect of vehicle vibration and reducing the speckle noise, denoted as $u(t)$. Finally, a TF of each railway track section $H(f)$, with f denoting frequency, is estimated using the segmented wheel-rail force $w(t)$ as input and the segmented track vibration $u(t)$ as output.
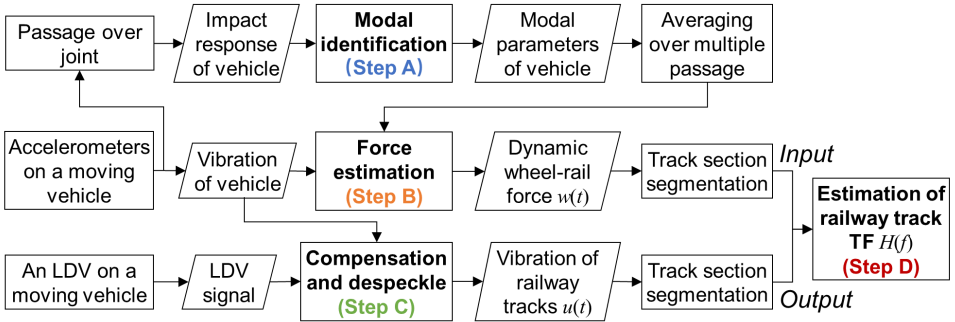

Figure 5.1: Flowchart of the proposed methodology.

5.2.1. INPUT: MODAL IDENTIFICATION AND FORCE ESTIMATION

The dynamics of a vehicle system (with n degrees of freedom) is usually characterized by the following equation of motion,

$$\mathbf{M}\ddot{\mathbf{x}}(t) + \mathbf{K}\mathbf{x}(t) + \mathbf{C}\dot{\mathbf{x}}(t) = \mathbf{w}(t) \tag{5.1}$$

where $\mathbf{M}$, $\mathbf{K}$, and $\mathbf{C}$ are the mass, stiffness, and damping matrices, respectively; $\mathbf{x}(t)$ is the displacement vector; $\mathbf{w}(t)$ is the external force vector, including wheel-rail forces. Eq. (5.1) can be converted to the modal coordinate as follows under the assumption of modal damping,

$$\mathbf{M}^*\ddot{\mathbf{q}}(t) + \mathbf{K}^*\mathbf{q}(t) + \mathbf{C}^*\dot{\mathbf{q}}(t) = \mathbf{p}(t) \tag{5.2}$$

where $\mathbf{M}^*$, $\mathbf{K}^*$, and $\mathbf{C}^*$ are the modal mass, stiffness, and damping matrices, respectively; $\mathbf{q}(t)$ and $\mathbf{p}(t)$ are the modal displacement and force vectors, respectively. From Eq. (5.1) to Eq. (5.2), the following transformation holds,

$$\mathbf{M}^* = \mathbf{\Phi}^\mathrm{T}\mathbf{M}\mathbf{\Phi} \quad \mathbf{K}^* = \mathbf{\Phi}^\mathrm{T}\mathbf{K}\mathbf{\Phi} \quad \mathbf{C}^* = \mathbf{\Phi}^\mathrm{T}\mathbf{C}\mathbf{\Phi} \quad \mathbf{x} = \mathbf{\Phi}\mathbf{q} \quad \mathbf{p} = \mathbf{\Phi}^\mathrm{T}\mathbf{w} \tag{5.3}$$

where $\mathbf{\Phi}$ is the mode shape matrix, consisting of mode shape vectors φ_1, …, φ_n, and $\mathbf{M}^*$, $\mathbf{K}^*$, $\mathbf{C}^*$ are diagonal matrices with the diagonal terms of modal mass m_1^*, …, m_n^*, modal stiffness k_1^*, …, k_n^*, and modal damping c_1^*, …, c_n^*, respectively.

Eq. (5.2) is equivalent to n single-degree-of-freedom systems as follows ($i=1$, …, n),

$$m_i^*\ddot{q}_i(t) + k_i^*q_i(t) + c_i^*\dot{q}_i(t) = p_i(t) \tag{5.4}$$

where $q_i(t)$ and $p_i(t)$ are the i-th component of $\mathbf{q}(t)$ and $\mathbf{p}(t)$, respectively. Further, Eq. (5.4) is equivalent to the following equation,

$$\ddot{q}_i(t) + \omega_i^2 q_i(t) + 2\omega_i\xi_i\dot{q}_i(t) = \frac{p_i(t)}{m_i^*} \tag{5.5}$$

where ω_i and ξ_i are the undamped natural frequency and damping ratio of the i-th mode, respectively.

As introduced in Section 1.2.4, existing wheel-rail force estimation methods usually assume that vehicle parameters $\mathbf{M}$, $\mathbf{K}$, and $\mathbf{C}$ are known, but this requirement is often difficult or expensive to fulfill. Therefore, we identify modal parameters (natural frequencies, damping ratios, mode shape vectors, and modal masses) of the vehicle under operational conditions so as to eliminate the need to define the vehicle parameters.

5.2.1.1. OPERATIONAL MODAL IDENTIFICATION

As shown in Section 3.4, the passage of a wheel over a joint induces a significant impact on the vehicle-track system. Such an impact can excite the vehicle modes over a wide range of frequencies, so the impact response measured by the accelerometers carries the dynamic characteristics of the vehicle. Other types of rail local irregularities can be used as alternative sources, such as degraded welds and crossings. We employ the enhanced frequency domain decomposition method in Section 3.2 to extract these characteristics, and the main steps are briefly given as follows.

Step A1. Estimate the power spectrum density (PSD) matrix of measured impact response using Welch's averaged periodogram method [148]. Considering the decay

pattern of impact response, using an exponential window in this procedure is recommended.

Step A2. Apply singular value decomposition to the PSD matrix at each discrete frequency f to obtain a diagonal matrix $\mathbf{V}(f)$ with singular values and a unitary matrix $\mathbf{U}(f)$ containing singular vectors corresponding to the singular values [78].

Step A3. Plot the spectrum of leading singular values and pick up resonance peaks in the frequency range of interest, which indicate the possible existence of vehicle modes.

Step A4. For each resonance peak, compare the singular vectors of adjacent frequencies, for example, using the modal assurance criterion [66]. If they are of high similarity, a vehicle mode can be confirmed.

Step A5. For the i-th vehicle mode, create an auto PSD using only the singular values of frequencies near the peak and apply inverse Fourier transform to the auto PSD to obtain an autocorrelation function. Then, estimate the damped natural frequency $\omega_{\mathrm{d}i}$ and the logarithmic decrement δ_i using the zero crossings and extremes of the autocorrelation function, respectively [82]. Further, calculate the undamped natural frequency ω_i and the damping ratio ξ_i as follows [82].

$$\xi_i = \frac{\delta_i}{\sqrt{\delta_i^2 + 4\pi^2}} \tag{5.6}$$

$$\omega_i = \frac{\omega_{\mathrm{d}i}}{\sqrt{1 - \xi_i^2}} \tag{5.7}$$

Step A6. For the i-th vehicle mode, normalize each singular vector at frequencies near the peak and rotate each complex component to 0°(or 180°) if its phase lies in the first or fourth (or the second or third) quadrant [66]. Average all these real-valued vectors to obtain the mode shape vector of the i-th vehicle mode, denoted as φ_i.

Step A7. Construct the mode shape matrix $\mathbf{\Phi}$ with all φ_i. Construct the mass matrix $\mathbf{M}$ with at least one known mass, such as the mass of an axle box. Determine the unknown masses by making $\mathbf{\Phi}^{\mathrm{T}}\mathbf{M}\mathbf{\Phi}$ a diagonal matrix, thus ensuring the diagonal property of $\mathbf{M}^*$. Calculate the modal mass matrix $\mathbf{M}^*$ that contains all m_i^* by $\mathbf{M}^*=\mathbf{\Phi}^{\mathrm{T}}\mathbf{M}\mathbf{\Phi}$.

The above method can produce the natural frequencies ω_i and $\omega_{\mathrm{d}i}$, damping ratio ξ_i, and mode shape vector φ_i of the n vehicle modes ($i=1, \ldots, n$). This eliminates the need to pre-define the vehicle stiffness, vehicle damping, and part of the vehicle masses (e.g., the vehicle body mass) for wheel-rail force estimation. The modal identification results can be averaged over multiple passages of different joints, and the vehicle modal parameters can then be updated regularly and used for estimating the wheel-rail force $w(t)$ from measured vehicle vibrations $\ddot{x}(t)$. This helps reduce force estimation errors due to variations and uncertainties in the vehicle parameters.

5.2.1.2. TIME-DOMAIN FORCE ESTIMATION

Based on the identified vehicle modal parameters, we adapt the time-domain method proposed in [110] for estimating wheel-rail forces. According to the Duhamel integral, the *i*-th modal displacement is expressed as follows.

$$q_i(t) = e^{-\omega_i \xi_i t}\left(\frac{\dot{q}_i(0)+\omega_i\xi_i q_i(0)}{\omega_{di}}\sin(\omega_{di}t)+q_i(0)\cos(\omega_{di}t)\right)+\frac{e^{-\omega_i\xi_i t}}{m_i^*\omega_{di}}\int_0^t e^{\omega_i\xi_i \tau}p_i(\tau)\sin(\omega_{di}(t-\tau))d\tau \quad (5.8)$$

where $p_i(0)$ and $\dot{q}_i(0)$ are the initial modal displacement and velocity, respectively.

By taking the first-order and second-order derivatives of Eq. (5.8) with respect to *t*, the modal velocity and acceleration can be obtained, respectively. Then, the modal displacement, velocity, and acceleration are discretized in the time step from *s*-1 to *s* ($\Delta t=t_s-t_{s-1}$, *s*=1, 2, …) as follows.

$$q_i(t_s) = e^{-\omega_i\xi_i\Delta t}\left(\frac{\dot{q}_i(t_{s-1})+\omega_i\xi_i q_i(t_{s-1})}{\omega_{di}}\sin(\omega_{di}\Delta t)+q_i(t_{s-1})\cos(\omega_{di}\Delta t)\right)$$
$$+\frac{e^{-\omega_i\xi_i\Delta t}}{m_i^*\omega_{di}}\int_0^{\Delta t}e^{\omega_i\xi_i\tau}p_i(\tau)\sin(\omega_{di}(\Delta t-\tau))d\tau \quad (5.9)$$

$$\dot{q}_i(t_s)=e^{-\omega_i\xi_i\Delta t}\left((\dot{q}_i(t_{s-1})+\omega_i\xi_i q_i(t_{s-1}))\cos(\omega_{di}\Delta t)-\omega_{di}q_i(t_{s-1})\sin(\omega_{di}\Delta t)\right)$$
$$+\frac{e^{-\omega_i\xi_i\Delta t}}{m_i^*\omega_{di}}\frac{d}{dt}\int_0^{\Delta t}e^{\omega_i\xi_i\tau}p_i(\tau)\sin(\omega_{di}(\Delta t-\tau))d\tau-\omega_i\xi_i q_i(t_s) \quad (5.10)$$

$$\ddot{q}_i(t_s)=\left((2\omega_i^2\xi_i^2-\omega_i^2)\dot{q}_i(t_{s-1})+\omega_i^3\xi_i q_i(t_{s-1})\right)\frac{e^{-\omega_i\xi_i\Delta t}\sin(\omega_{di}\Delta t)}{\omega_{di}}$$
$$-(\omega_i^2 q_i(t_{s-1})+2\omega_i\xi_i\dot{q}_i(t_{s-1}))e^{-\omega_i\xi_i\Delta t}\cos(\omega_{di}\Delta t)$$
$$+\frac{e^{-\omega_i\xi_i\Delta t}}{m_i^*\omega_{di}}\left(\omega_i^2\xi_i^2-2\omega_i\xi_i\frac{d}{dt}+\frac{d^2}{dt^2}\right)\int_0^{\Delta t}e^{\omega_i\xi_i\tau}p_i(\tau)\sin(\omega_{di}(\Delta t-\tau))d\tau \quad (5.11)$$

The following integrals can be obtained when the modal force is assumed constant within the time step from *s*-1 to *s*.

$$\int_0^{\Delta t}e^{\omega_i\xi_i\tau}p_i(\tau)\sin(\omega_{di}(\Delta t-\tau))d\tau = \frac{p_i(t_{s-1})}{\omega_i^2}\left(\omega_{di}e^{\omega_i\xi_i\Delta t}-\omega_{di}\cos(\omega_{di}\Delta t)-\omega_i\xi_i\sin(\omega_{di}\Delta t)\right) \quad (5.12)$$

$$\frac{d}{dt}\int_0^{\Delta t}e^{\omega_i\xi_i\tau}p_i(\tau)\sin(\omega_{di}(\Delta t-\tau))d\tau = \frac{p_i(t_{s-1})}{\omega_i}\left(\omega_{di}\xi_i e^{\omega_i\xi_i\Delta t}+\omega_i(1-\xi_i^2)\sin(\omega_{di}\Delta t)-\omega_{di}\xi_i\cos(\omega_{di}\Delta t)\right) \quad (5.13)$$

$$\frac{d^2}{dt^2}\int_0^{\Delta t}e^{\omega_i\xi_i\tau}p_i(\tau)\sin(\omega_{di}(\Delta t-\tau))d\tau = p_i(t_{s-1})\left(\omega_{di}\xi_i^2 e^{\omega_i\xi_i\Delta t}+\omega_{di}(1-\xi_i^2)\cos(\omega_{di}\Delta t)\right)$$
$$+p_i(t_{s-1})\omega_i\xi_i(1-\xi_i^2)\sin(\omega_{di}\Delta t) \quad (5.14)$$

By substituting Eq. (5.12)~(5.14) to Eq. (5.9)~(5.11), the following relationships can be obtained.

$$q_i(t_s) = e^{-\omega_i \xi_i \Delta t} \sin(\omega_{di}\Delta t)\left(\frac{\dot{q}_i(t_{s-1}) + \omega_i \xi_i q_i(t_{s-1})}{\omega_{di}} - \frac{\xi_i p_i(t_{s-1})}{m_i^* \omega_i \omega_{di}}\right)$$
$$+ e^{-\omega_i \xi_i \Delta t} \cos(\omega_{di}\Delta t)\left(q_i(t_{s-1}) - \frac{p_i(t_{s-1})}{m_i^* \omega_i^2}\right) + \frac{p_i(t_{s-1})}{m_i^* \omega_i^2}$$

(5.15)

$$\dot{q}_i(t_s) = e^{-\omega_i \xi_i \Delta t} \sin(\omega_{di}\Delta t)\left(\frac{(1-\xi_i^2)p_i(t_{s-1})}{m_i^* \omega_{di}} - \omega_{di}q_i(t_{s-1})\right)$$
$$+ e^{-\omega_i \xi_i \Delta t} \cos(\omega_{di}\Delta t)\left(\dot{q}_i(t_{s-1}) + \omega_i \xi_i q_i(t_{s-1}) - \frac{\xi_i p_i(t_{s-1})}{m_i^* \omega_i}\right) - \omega_i \xi_i q_i(t_s) + \frac{\xi_i p_i(t_{s-1})}{m_i^* \omega_i}$$

(5.16)

$$\ddot{q}_i(t_s) = \frac{e^{-\omega_i \xi_i \Delta t} \sin(\omega_{di}\Delta t)}{\omega_{di}}\left((2\omega_i^2 \xi_i^2 - \omega_i^2)\dot{q}_i(t_{s-1}) + \omega_i^3 \xi_i q_i(t_{s-1}) - \frac{\omega_i \xi_i p_i(t_{s-1})}{m_i^*}\right)$$
$$+ e^{-\omega_i \xi_i \Delta t} \cos(\omega_{di}\Delta t)\left(-\omega_i^2 q_i(t_{s-1}) - 2\omega_i \xi_i \dot{q}_i(t_{s-1}) + \frac{p_i(t_{s-1})}{m_i^*}\right)$$

(5.17)

Eq. (5.17) can be written in the following form.

$$p_i(t_{s-1}) = \frac{m_i^* \sin(\omega_{di}\Delta t)\left((2\omega_i^2 \xi_i^2 - \omega_i^2)\dot{q}_i(t_{s-1}) + \omega_i^3 \xi_i q_i(t_{s-1})\right)}{\omega_i \xi_i \sin(\omega_{di}\Delta t) - \omega_{di}\cos(\omega_{di}\Delta t)}$$
$$+ \frac{m_i^* \omega_{di}\cos(\omega_{di}\Delta t)\left(-\omega_i^2 q_i(t_{s-1}) - 2\omega_i \xi_i \dot{q}_i(t_{s-1})\right) - m_i^* \omega_{di}e^{\omega_i \xi_i \Delta t}\ddot{q}_i(t_s)}{\omega_i \xi_i \sin(\omega_{di}\Delta t) - \omega_{di}\cos(\omega_{di}\Delta t)}$$

(5.18)

Further, based on the modal parameters (the natural frequencies ω_i and ω_{di}, damping ratio ξ_i, mode shape vector φ_i, and modal mass m_i^* of the n vehicle modes) obtained in Section 5.2.1.1, the wheel-rail force on the vehicle $w(t)$ can be estimated from measured vehicle vibrations $\ddot{x}(t)$ through the following steps. Since wheel-rail contact forces are applied on wheels, only the elements in $w(t)$ corresponding to forces on wheels represent wheel-rail forces, and the rest are constrained to zero in the estimation process.

Step B1. At the s-th time step, convert the measured acceleration $\ddot{x}(t_s)$ to modal acceleration $\ddot{q}(t_s)$ according to Eq. (5.3). For the i-th mode, estimate the i-th element of the modal force vector $p_d(t_{s-1})$ according to Eq. (5.18) using the current modal acceleration $\ddot{q}(t_s)$ and the previous modal displacement and velocity $q(t_{s-1})$, $\dot{q}(t_{s-1})$ [110]. Use zero initial condition when $s=1$, i.e., $q(t_0) = 0$ and $\dot{q}(t_0) = 0$.

Step B2. Convert the calculated modal force $p_d(t_{s-1})$ to a force vector $w_d(t_{s-1})$ according to Eq. (5.3). Constrain the elements of $w_d(t_{s-1})$ without external forces to zero, denoted as $w(t_{s-1})$. Then, convert the corrected force $w(t_{s-1})$ back to the modal force $p(t_{s-1})$ according to Eq. (5.3).

Step B3. According to Eq. (5.15)~(5.16), calculate the modal displacement and velocity at the current step $q(t_s)$, $\dot{q}(t_s)$ using the corrected modal force $p(t_{s-1})$ [110].

Step B4. Increase s by a time step and repeat the above process till reaching the signal end.

Step B5. Detrend the estimated force $w(t)$ by filtering it with a high-pass filter.

5.2.2. OUTPUT: DESPECKLE AND COMPENSATION

In the proposed methodology, the vibration response of track components is continuously measured by an LDV on the moving vehicle. Speckle noise is inevitable due to the significant in-plane motion of the laser spot on the track surface, and the characteristics of speckle noise vary with the vehicle speed. In this chapter, we reduce speckle noise in a raw LDV signal $u_r(t)$ using the speed-adaptive method developed in Section 4.3. Meanwhile, the vibrations of the LDV and other optical components along the laser beam affect the relative velocity between the laser head and the target. These vibrations are measured, denoted as $\dot{x}_{c_1}(t)$, $\dot{x}_{c_2}(t)$, ..., and their effect on the LDV signal should be compensated. The despeckle and compensation steps are given as follows.

Step C1. The same as Step 1 in Section 4.3.1.

Step C2. The same as Step 2 in Section 4.3.1. Denote the imputed signal as $u_p(t)$.

Step C3. Subtract $\dot{x}_{c_1}(t)$, $\dot{x}_{c_2}(t)$, ... from the imputed signal $u_p(t)$ as follows.

$$u_t(t) = u_p(t) - \sum_j \dot{x}_{c_j}(t) \tag{5.19}$$

Step C4. Apply a band-pass filter with the cut-off frequency of f_L and f_H to $u_t(t)$, resulting in the extracted structural vibration $u(t)$.

The effectiveness of the above method requires a proper selection of its parameters. According to Section 2.3.4 and 4.3, we recommend using $d_A=1$, $q_A=1$ and setting f_L and f_H to the lowest and highest frequencies of interest for railway track vibrations, respectively. The parameters $P\%$ and p_A should be tuned considering the despeckle performance and the computational cost at different speeds, which can be achieved either quantitatively based on simulated signals or qualitatively through trial and observation with measured signals. Once these parameters are defined, the method can be applied to LDV measurements without adjusting its parameters for different vehicle speeds.

5.2.3. TRANSFER FUNCTION ESTIMATION

A railway track is a continuous structure. When measuring its TFs from a running vehicle, the load and response locations move, and the input-output relationship varies. Considering the variation in track dynamic properties between different locations, we divide railway tracks into distributed sections and estimate a TF using measurements on each track section, representing the average input-output relationship for the track section. Each track section should not be too long; otherwise, we cannot capture the variation within it. It should also not be too short; otherwise, insufficient data points can cause large errors and poor frequency resolution. Once the track section length is defined, the estimated wheel-rail force $w(t)$ and the measured track vibration $u(t)$ can be cut for each track section, which can be used as the input and output for TF estimation, respectively.

In this chapter, assuming that the noise is uncorrelated with the excitation, we use the so-called H_1 estimator to calculate the TF. The main steps are given as follows.

Step D1. For each track section, divide $w(t)$ and $u(t)$ into overlapping segments and taper each segment with a window function.

Step D2. Estimate the cross PSD of $w(t)$ and $u(t)$, denoted as $P_{uw}(f)$, and the PSD of $w(t)$, denoted as $P_{ww}(f)$, using Welch's averaged periodogram method [148].

Step D3. Calculate the TF in terms of a receptance function with the input of the wheel-rail force and the output of the track displacement, as follows [111, 112].

$$H(f) = \frac{P_{uw}(f)}{2\pi f \cdot P_{ww}(f)} \tag{5.20}$$

5.3. Laboratory Validation

5.3.1. Experimental setup

We validate the proposed methodology in V-Track, as shown in Figure 5.2. The details of this test rig and the instrumentation can be found in Section 2.2.1. The vehicle system consists of a vehicle body suspended on an axle box with a wheel. The suspension provides not only stiffness and damping but also a static wheel load. There are two such vehicle systems (Vehicle A and Vehicle B) assembled symmetrically at the ends of a rotating beam. Four accelerometers (PCB 356B21) are mounted on the upper and lower masses of the vehicle to estimate the dynamic wheel-rail forces. An additional accelerometer is mounted on the mirror to compensate for its effect on the LDV signal. As shown in Figure 5.2 (b), we instrument some track sections with accelerometers (PCB 356B21) to measure their vertical vibrations for comparisons.
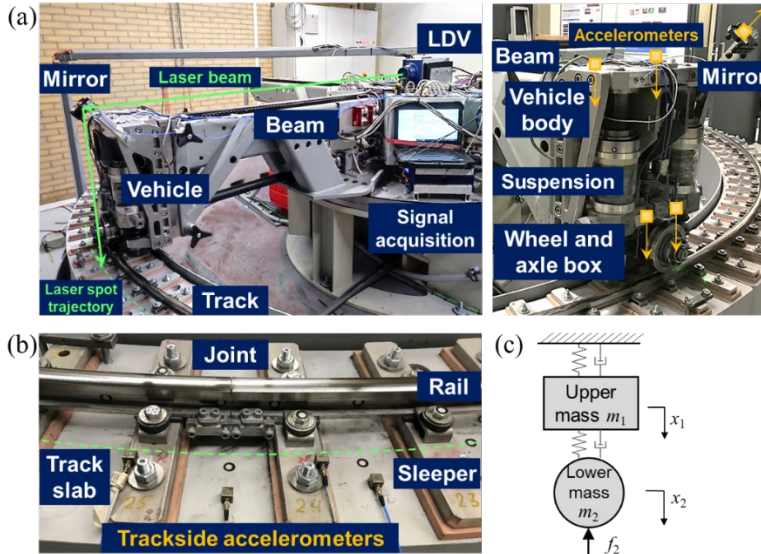

Figure 5.2: Experiment setup and vehicle model. (a) V-Track test rig and the instrumentation; (b) Trackside sensors; (c) Model of the vehicle system.

5.3.2. MODAL IDENTIFICATION AND FORCE ESTIMATION

We use the model in Figure 5.2 (c) to represent the vertical dynamics of the vehicle in V-Track. Each of the two masses has one degree of freedom of bouncing. The spring and damper between them represent the suspension, and those on top represent the combined stiffness and damping from both the connection of the vehicle body on the rotating beam and the flexibility of the rotating beam. A force is applied on the lower mass, representing the contact force on the wheel. For Vehicle A and B, the lower mass represents the wheel and axle box with their total mass known (m_2=40 kg), while the upper mass represents the combination of the vehicle body mass and part of the rotating beam mass, so the total mass m_1 is unknown. All the stiffness and damping are also unknown.

According to Section 5.2.1.1, we use the impact response of each vehicle to identify its modal parameters. Figure 5.3 (a) and (b) show the vibrations of Vehicle A and B when passing over a joint at 4 km/h, respectively. The impact response caused by the passage of the joint can be clearly observed. Both masses show attenuated bouncing motions at relatively low frequencies, while the response of the lower mass contains more high-frequency components.

In order to reduce the effect of pitching motion and noise, we average the signals of the two sensors on each mass. Then, for each vehicle, we apply Step A1~A3 to the averaged signals, and a singular value spectrum can be obtained for each passage over a joint. Figure 5.3 (c) and (d) plot such spectra calculated from different laps of measurements (at the same speed) for the two vehicles. The results show high repeatability between the different laps and also similarity between the two vehicles. For each vehicle, two dominant peaks below 150 Hz are confirmed through Step A4.
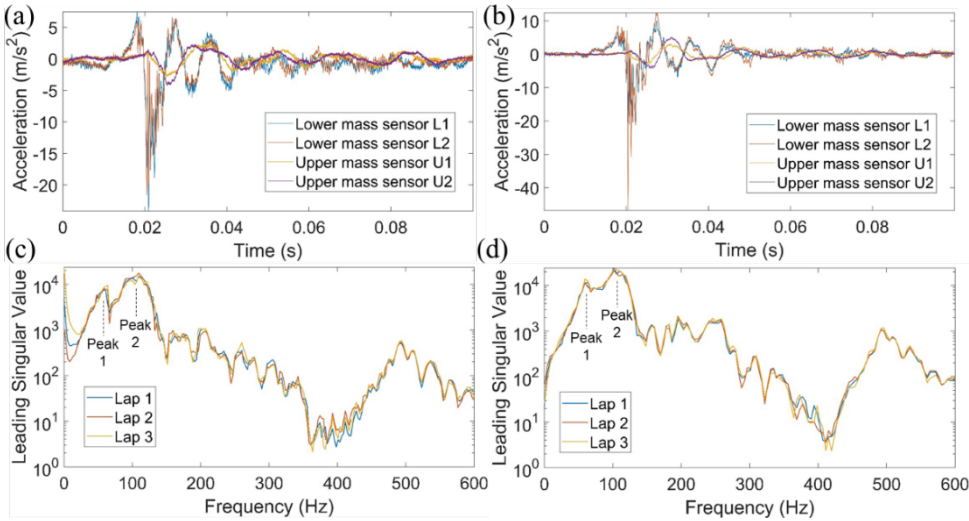

Figure 5.3: Vehicle vibrations and singular value spectra. (a) Impact response of Vehicle A; (b) Impact response of Vehicle B; (c) Spectra of Vehicle A; (d) Spectra of Vehicle B.

Table 5.1: Identified modal parameters of the two vehicles.

Modes	Averaged modal parameters	Vehicle A	Vehicle B
Peak 1 (in-phase bounce)	Undamped natural frequency ω_1	62.0 Hz	62.6 Hz
	Damping ratio ξ_1	0.15	0.11
	Normalized mode shape vector φ_1	$[0.83 \ \ 1]^T$	$[0.74 \ \ 1]^T$
	Modal mass m_1^*	170.9	187.8
Peak 2 (anti-phase bounce)	Undamped natural frequency ω_2	98.5 Hz	111.7 Hz
	Damping ratio ξ_2	0.09	0.14
	Normalized mode shape vector φ_2	$[-0.25 \ \ 1]^T$	$[-0.2 \ \ 1]^T$
	Modal mass m_2^*	52.5	50.8

The modal parameters corresponding to these two peaks are further identified through Step A5 and A7. After averaging over different speeds (2 km/h, 4 km/h, 6 km/h, 8 km/h), different joints, and different laps, we obtain the result in Table 5.1. It shows that the two peaks correspond to the in-phase and anti-phase bouncing motions of the two masses, respectively. Despite the identical design, the identified modal parameters of the two vehicles deviate slightly, highlighting the value of modal identification under operational conditions.

According to Section 5.2.1.2, the identified modal parameters in Table 5.1 are further used to estimate wheel-rail force through Step B1~B5. Figure 5.4 (a) and (b) show the estimated forces using the accelerations of Vehicle A at a joint at different speeds. The results contain both positive and negative forces since static wheel loads are not included. Some residual drifts can also be observed but have little effect on the dynamic components and the TF estimation. High-frequency P1 force and low-frequency P2 force can be observed, and their amplitudes become larger as the vehicle speed increases.
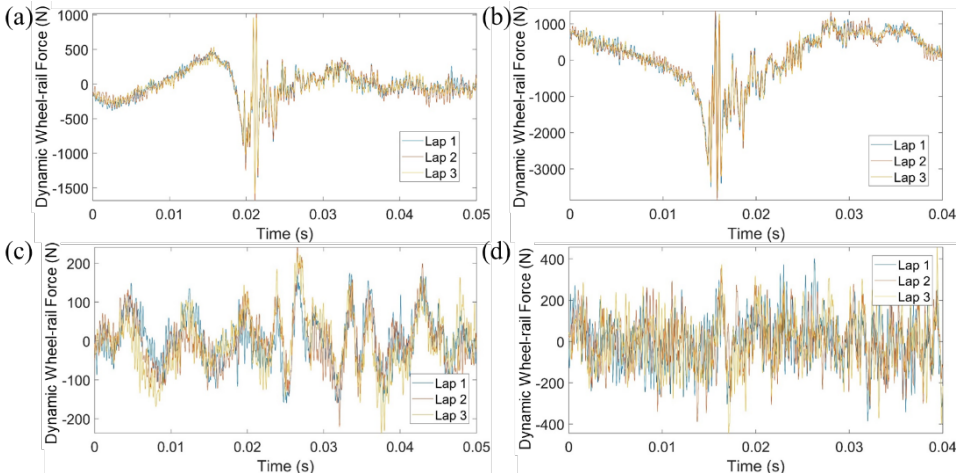

Figure 5.4: Estimated dynamic wheel-rail forces of Vehicle A. (a) Passing over a joint at 8 km/h; (b) Passing over a joint at 16 km/h; (c) Running on a normal track at 8 km/h; (d) Running on a normal track at 16 km/h.

Figure 5.4 (c) and (d) plot the estimated wheel-rail forces of Vehicle A using measurements on a normal track section. The low-frequency components are considered to be related to the vertical alignment of the track, while the high-frequency components are considered to be related to the roughness of the wheel and rail. Meanwhile, the amplitude of the dynamic wheel-rail force becomes larger when the speed is higher.

5.3.3. DESPECKLE AND COMPENSATION

In this section, we validate the despeckle and compensation method in Section 5.2.2. We divide the track structure of V-Track into overlapping track sections centered at each sleeper, and each track section has a length of around two sleeper spacings. Such segmentation enables the track structure to be characterized as a distributed system so that the estimated TF describes the track dynamic properties near each sleeper. Figure 5.5 shows the measurement configurations of Vehicle A on two typical track sections. Considering the laser-wheel offset Δx, the wheel passes over the joint when the LDV measures Track section ①, while the wheel runs on a normal track section when the LDV measures Track section ④. For comparison, we mount three accelerometers (J1~J3 and T2~T4) on each track section.
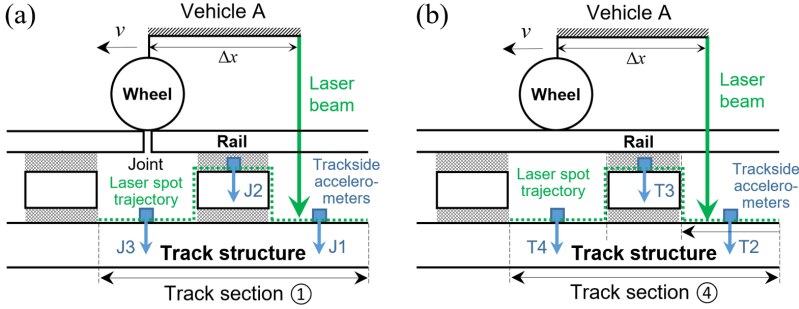

Figure 5.5: LDV and trackside measurement on two track sections. (a) Track section ① with a joint; (b) Track section ④ without joints.

First, measurements on Track section ① at different speeds are studied. The range of the speeds is selected considering the speed-dependent signal-to-noise ratio in Section 4.5.2. We use $P\%=30\%$, $p_A=30$, $f_L=50$ Hz, and $f_H=1,000$ Hz in Step C1~C4, and the despeckle and compensation results are shown in Figure 5.6. The two plots on the left compare the raw LDV signal, the imputed signal (after Step C2), and the mirror vibration (after integration from acceleration to velocity [144]). It shows that spikes are detected and replaced with reasonable predictions. The mirror vibration is dominant at low frequencies, reflecting the necessity to compensate for its effect. The two plots on the right compare the LDV signal after despeckle and compensation with those measured by the trackside sensors (after integration from acceleration to velocity), which shows good agreement in the impact response phase as well as before and after the impact.
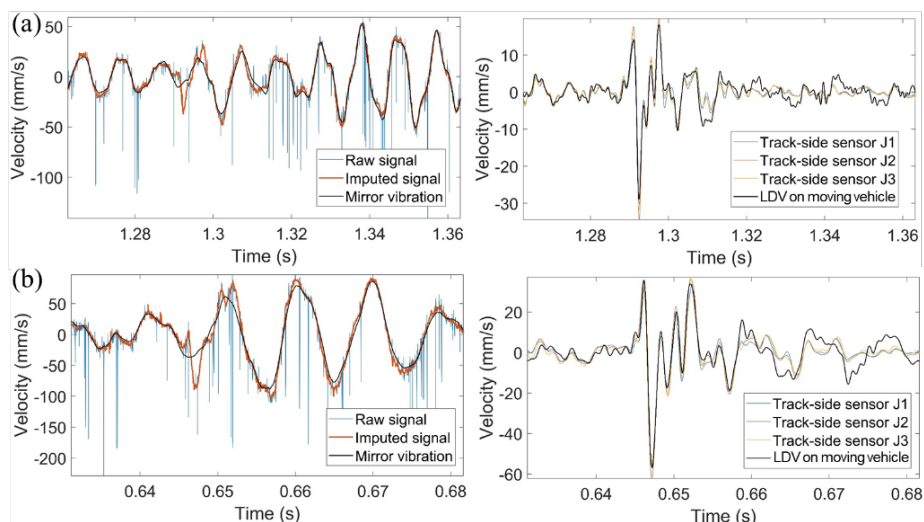
Figure 5.6: Despeckle, compensation, and comparison with trackside measurements on Track section ①. (a) 8 km/h; (b) 16 km/h.
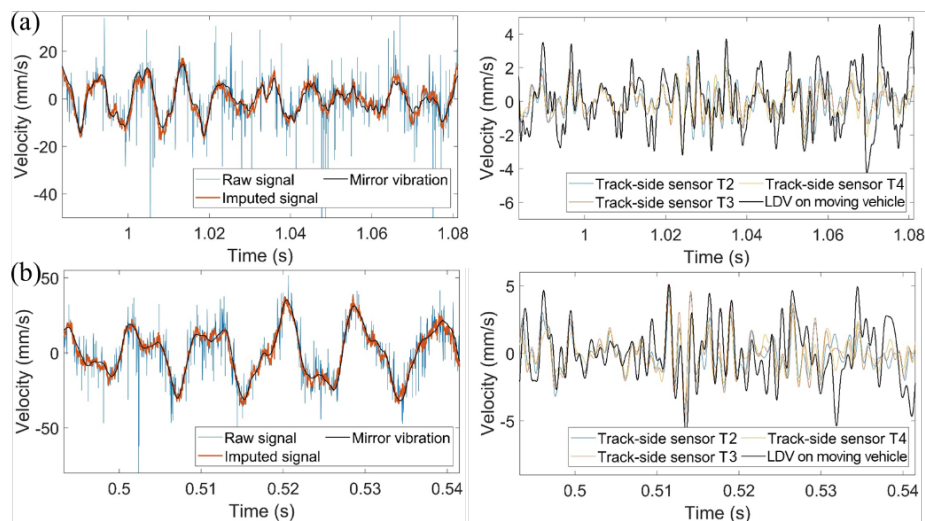
Figure 5.7: Despeckle, compensation, and comparison with trackside measurements on Track section ④. (a) 8 km/h; (b) 16 km/h.

Figure 5.7 presents the despeckle and compensation results for measurements on Track section ④. Although their amplitudes are generally lower than those on Track section ①, the proposed method is still effective in reducing speckle noise and providing results consistent with the trackside measurements. The above results demonstrate the effectiveness of the despeckle and compensation method at different speeds. Slight deviations between the LDV and trackside signals can be observed, caused by imperfect despeckle or compensation and spatial deviations between the laser spot and the accelerometers.

Additionally, it can be seen from Figure 5.6 and 5.7 that the vibrations of the sleeper (J2 or T3) and the track slab (J1, J3 or T2, T4) are very close in the frequency range we are concerned with, as a consequence of the high sleeper pad stiffness in V-Track. This reflects the rationale for combining measurements on the sleeper and track slab (within one track section) for TF estimation, which provides more data points than using only measurement on a single sleeper.

5.3.4. TRANSFER FUNCTION ESTIMATION AND COMPARISON

Based on the measured track vibration and the estimated wheel-rail force on each track section, a TF of the track structure can be estimated according to Section 5.2.3. We take several track sections as examples to showcase the estimation performance. In Step D1, each signal is divided into three overlapping segments of 90% of the section length. In Step D2, a Hanning window is used. The estimated TFs hold the physical meaning (receptance) that is consistent with the conventional definition of railway track TFs or FRFs. This allows the TF measurement system on the moving vehicle to be validated using conventional trackside technology. Therefore, we perform hammer tests on these track sections using a PCB 086C03 hammer and the trackside accelerometers to obtain their FRFs. The estimation of FRFs can be found in Section 3.4.

5.3.4.1. TRACK SECTIONS WITH A JOINT

Figure 5.8 shows the measurement configuration on Track sections ① and ②. Since Vehicle A and B have different laser-wheel offsets, they measure different track sections when passing over the joint. For Vehicle A (or Vehicle B), the laser spot is behind (or ahead of) the wheel and thereby measures Track section ① (or ②) when the wheel passes over the joint. Additionally, hammer tests are performed, with the impact locations denoted as I1~I3 and the trackside sensors denoted as J1~J4.
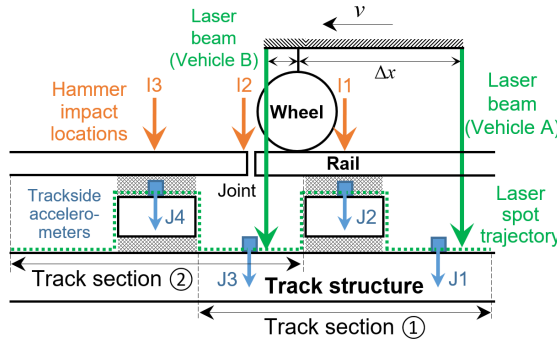
Figure 5.8: Measurement and hammer tests on track sections with a joint.

Figure 5.9 (or Figure 5.10) shows the TFs of Track section ① (or ②) estimated from the measurements on Vehicle A (or B) at two different speeds, in which the solid black line and shaded area represent the mean and stand deviation of the estimates from different laps, respectively. We focus on the frequency range of 200~800 Hz as it belongs to the rigid-body motions (bouncing and rolling) of the sleepers under the wheel passage in V-Track, according to Section 3.4, which are more related to the properties

of the track structure, such as the support stiffness. Meanwhile, the small hammer used in the hammer tests can effectively excite the track modes in this frequency range. It can be seen that the frequency resolution decreases at a higher speed due to the shorter signal length. At frequencies below 600 Hz, the standard deviation is small, indicating good repeatability at different laps, while at higher frequencies, the standard deviation becomes larger. The frequency range of small standard deviations is broader at the higher speed, mainly because the vehicle moving at a higher speed generates larger excitations at higher frequencies.

The colored solid lines in Figure 5.9 represent the average TFs estimated using signals from the trackside sensors instead of the LDV signal. The results of using the LDV and the trackside sensors are close to each other since the LDV signals after despeckle and compensation are close to the trackside signals. This further demonstrates the accuracy of the track vibration measurement using the LDV on the moving vehicle.
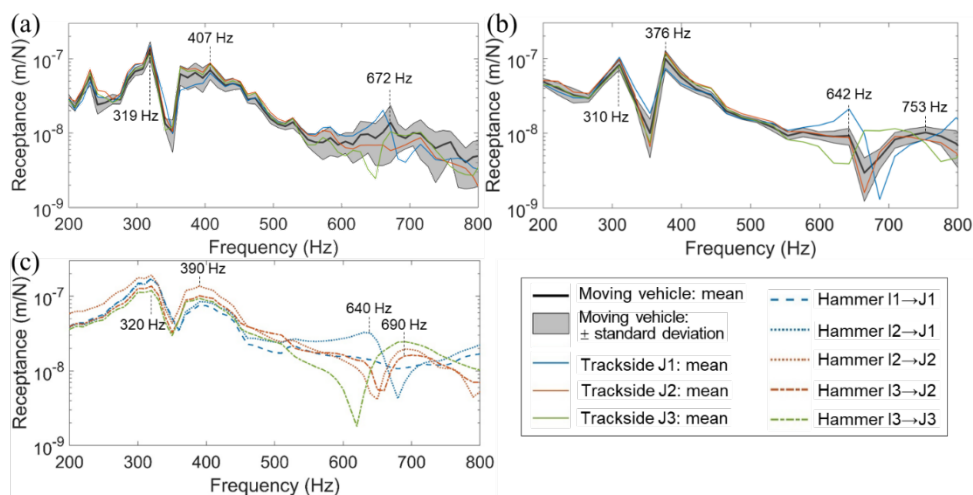
Figure 5.9: TF estimation and comparison on Track section ① (Vehicle A). (a) 8 km/h; (b) 16 km/h; (c) Hammer tests.

Figure 5.10: TF estimation and comparison on Track section ② (Vehicle B). (a) 8 km/h; (b) 16 km/h.

Further, we compare the estimated TFs with FRFs from the hammer tests, where the impact and sensor locations correspond to the wheel-laser offset. A good agreement in their shapes and resonance frequencies can be observed, especially below 500 Hz,

demonstrating the effectiveness of TF estimation on different vehicles and at different speeds. The two resonance peaks at 300~400 Hz in the FRFs are effectively captured by the estimated TFs from the moving vehicle. At frequencies above 500 Hz, the FRFs deviate from each other, representing different dynamic properties for different impact and sensor locations. Consequently, the estimated TFs show large standard deviations as the positions of the wheel and laser spot are moving, and the resonance frequencies of the estimated TFs deviate more from those of the FRFs. Additionally, the FRFs are smoother than the estimated TFs due to less noise and higher frequency resolution.

5.3.4.2. TRACK SECTIONS WITHOUT JOINTS

Similar measurements and comparisons are performed on three track sections without joints, as illustrated in Figure 5.11. The TF estimates of Vehicle A and B on Track section ③ are shown in Figure 5.12 and 5.13, respectively. By comparing them with the FRFs from the hammer tests, we can see good agreement in their shapes and resonance frequencies at different speeds. As the vehicle speed increases, their deviation increases at low frequencies and decreases at high frequencies. Additionally, the differences between the TF estimates on Vehicles A and B are caused by the different positions of the wheels when measuring this track section.

By comparing Figure 5.12 and 5.13 with Figure 5.9 and 5.10, we can see that there is one dominant peak in the frequency range of 300~400 Hz on the track section without joints whereas there are two on the track sections with a joint. This difference reflects the variation in track dynamic properties between these sections. Additionally, the standard deviations of the estimates on the track sections with the joint are generally smaller than those without joints. This confirms that excitations with large amplitude and broad frequency bands improve the TF estimation performance.

The TF estimation results on Track sections ④ and ⑤ are shown in Figure 5.14 and 5.15, respectively. The estimated TFs are in good agreement with the measured FRFs and capture the dominant resonance peaks. As the vehicle speed increases, their deviation at high frequencies becomes smaller, whereas that at low frequencies becomes larger. The results demonstrate the effectiveness of TF estimation on normal track structures at different speeds.
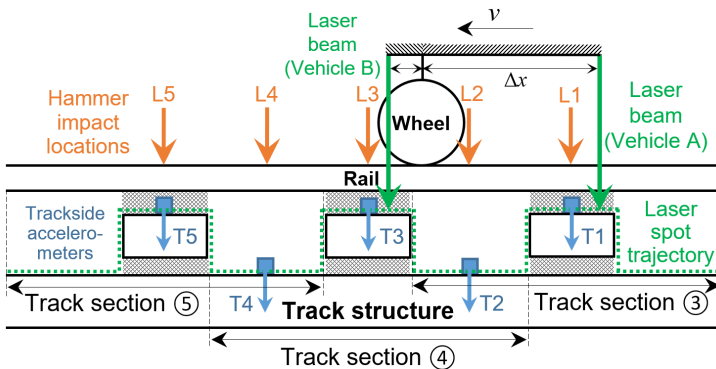
Figure 5.11: Measurement and hammer tests on track sections without joints.

Figure 5.12: TF estimation and comparison on Track section ③ (Vehicle A). (a) 8 km/h; (b) 10 km/h; (c) 14 km/h; (d) 16 km/h; (e) Hammer tests.
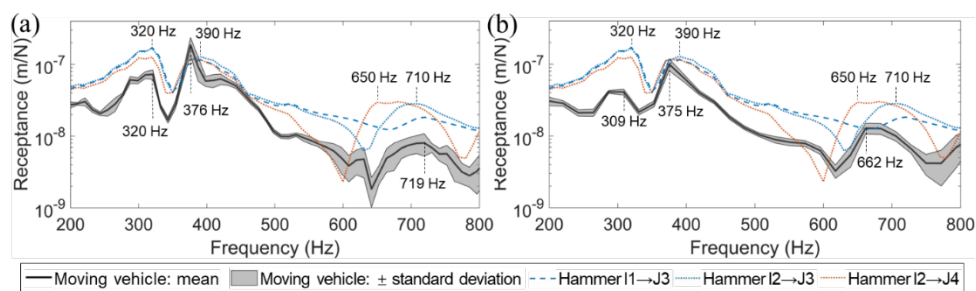

Figure 5.13: TF estimation and comparison on Track section ③ (Vehicle B). (a) 8 km/h; (b) 10 km/h; (c) 14 km/h; (d) 16 km/h.

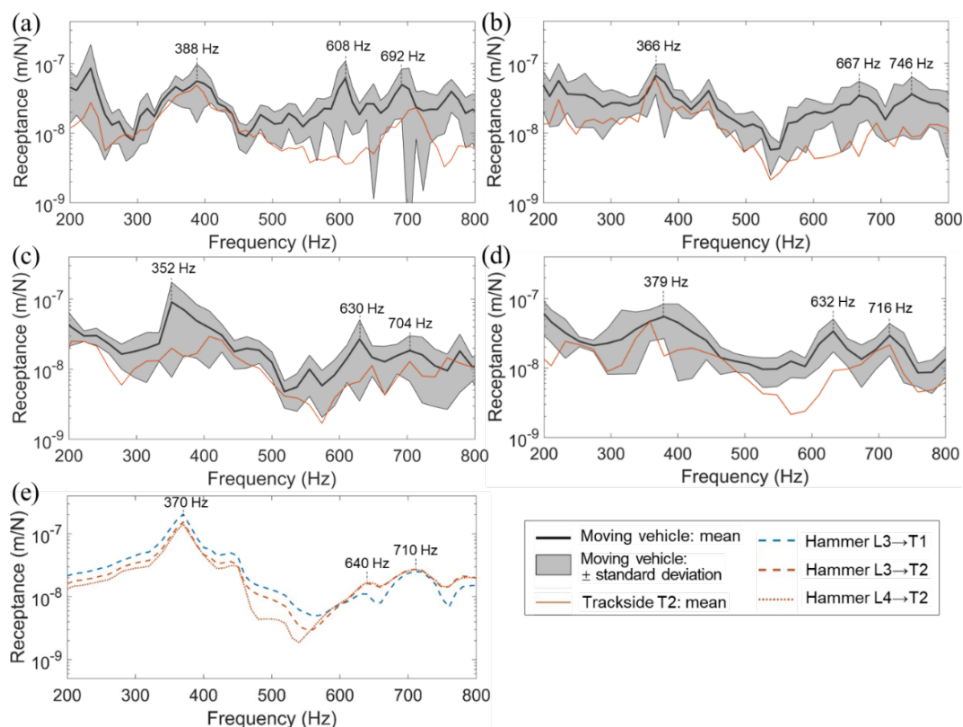Figure 5.14: TF estimation and comparison on Track section ④ (Vehicle A). (a) 8 km/h; (b) 10 km/h; (c) 14 km/h; (d) 16 km/h; (e) Hammer tests.

Figure 5.15: TF estimation and comparison on Track section ⑤ (Vehicle B). (a) 8 km/h; (b) 10 km/h; (c) 14 km/h; (d) 16 km/h; (e) Hammer tests.
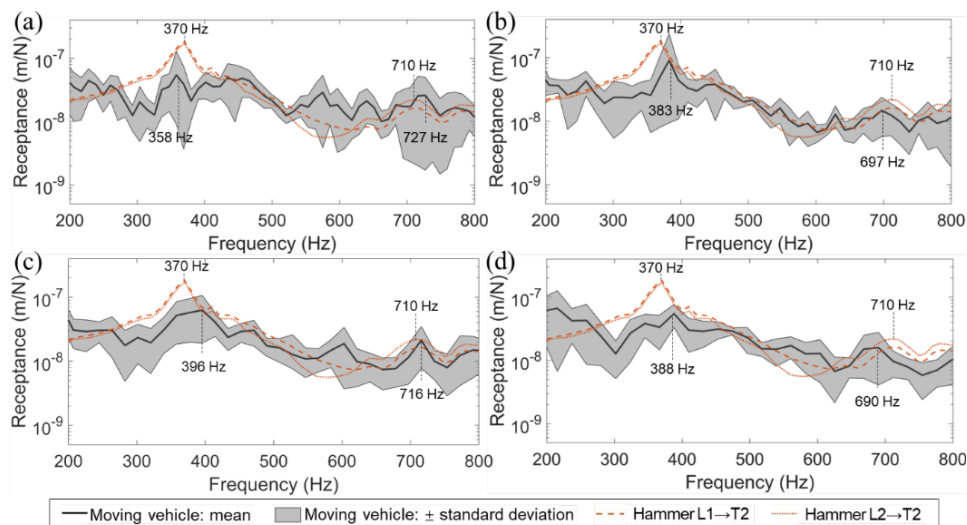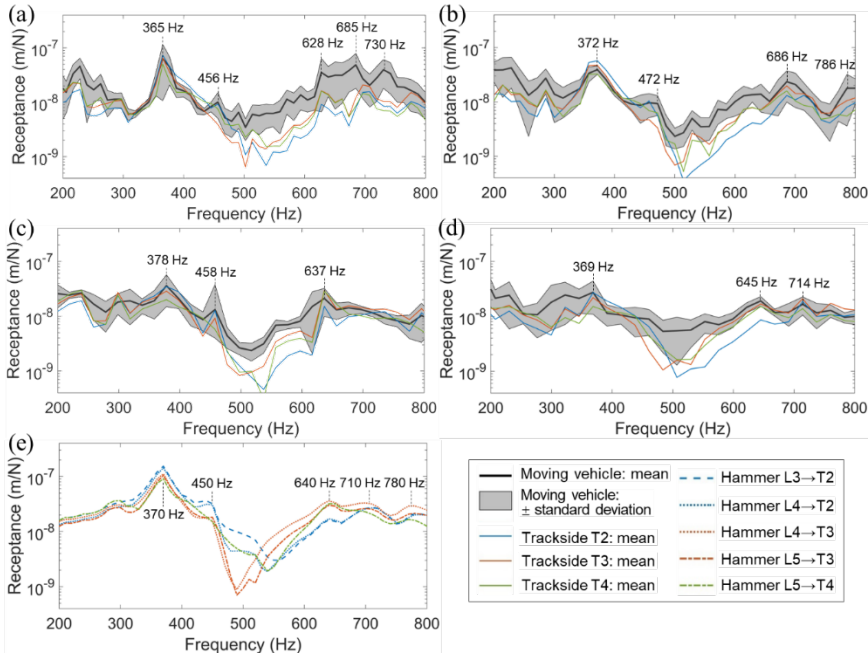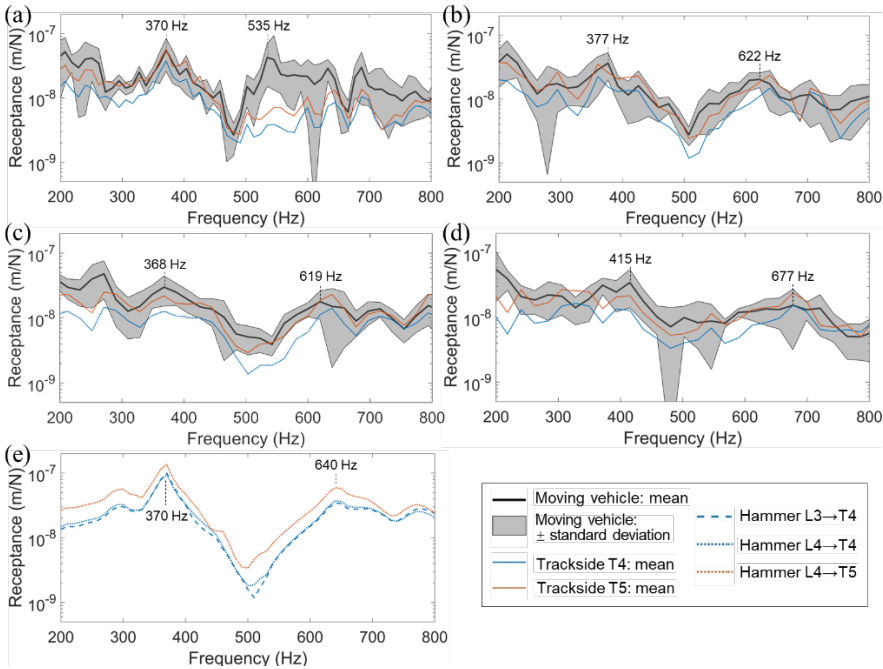
In this chapter, we focus on the shapes and the resonance frequencies of the TFs and FRFs since they depend strongly on the track dynamic properties, such as the track stiffness, thus being useful for structural health monitoring. Nevertheless, deviations in both frequency and amplitude can be observed, and the possible reasons are discussed as follows.

- The track properties, such as stiffness and damping, can differ from unloaded conditions to loaded conditions due to the nonlinearity of track components. The developed system on the moving vehicle has the advantage of measuring the TFs under loaded conditions, whereas the hammer tests measure the FRFs without vehicle loads.
- Errors in the vehicle model for wheel-rail force estimation are considered to be the main source of errors in the TF estimation. Errors in the vehicle parameters can be reduced by regularly updating the vehicle model through the operational modal identification.
- Vehicle A and B are assembled symmetrically on the rotating beam, which affects each other primarily through the rotating beam and secondarily through the track structure. This chapter assumes a single input for each vehicle and a single input for the track structure, so each vehicle is an additional excitation source for the other vehicle and the track structure, thus affecting the force and TF estimation. Our vibration measurements show that such influence is negligible, so decoupling the two vehicles in the TF estimation is still reasonable.

5.4. Conclusions

This chapter proposes a methodology for estimating railway track TFs using LDV and accelerometer measurement on a moving vehicle. Enhanced frequency domain decomposition is applied to vehicle impact response at a joint to obtain its modal parameters, which further support the estimation of dynamic wheel-rail forces from vehicle vibrations using a Duhamel integral-based method. A speed-adaptive despeckle and compensation method is applied to LDV signals to reduce speckle noise and extract track vibrations. A TF is then estimated for each railway track section using the estimated wheel-rail force as input and the measured track vibrations as output. This methodology is validated on different sections of V-Track at different speeds through comparisons with trackside measurements and hammer tests. The main conclusions are summarized as follows.

- The modal identification method eliminates the need to pre-define the vehicle stiffness, vehicle damping, and vehicle body mass for wheel-rail force estimation and enables the vehicle modal parameters to be updated under operational conditions.
- The LDV and accelerometer measurements provide TF estimates that are in good agreement in terms of the shapes and resonance frequencies with the FRFs measured from hammer tests at 200~800 Hz. Such effectiveness holds for the whole vehicle speed range tested, from 8 km/h to 16 km/h.

- The standard deviation of the TF estimates becomes larger at high frequencies due to the variation of track dynamics when the wheel and laser spot are moving. Among the speeds tested, a higher vehicle speed yields smaller standard deviations of the estimated TFs over different laps and also smaller deviations between the estimated TFs and the measured FRFs at high frequencies.
- Unlike conventional hammer tests that can only be applied at one location at a time, usually without vehicle loads, the proposed TF measurement system can continuously scan track structures and measure their TFs under loaded conditions.
- The differences in the shapes and resonance frequencies of the estimated TFs between different track sections reflect the variation of track dynamic properties, suggesting that the system has the potential to be used for structural health monitoring of railway tracks.

5

5

6

CONCLUSIONS AND RECOMMENDATIONS

6.1. CONCLUSIONS

This dissertation presents a new technology based on train-borne laser Doppler vibrometer (LDV) for measuring the load-response relationship of railway tracks. **The developed technology consists of four cornerstones** that address the key challenges, including speckle noise mitigation, operational vibration analysis, speed-dependent characteristics, and transfer function estimation. The interconnections of these cornerstones in developing the technology are summarized as follows.

- The three-step framework for speckle noise reduction (Chapter 2) plays an important role in the investigation of the speed-dependent characteristics by enabling the vibration-noise separation at different speeds (Chapter 4 and 5). It is further combined with the compensation of the LDV vibration to support the estimation of the load-response relationship of the track structure (Chapter 5).

- The operational modal analysis method (Chapter 3) supports the identification of the vehicle modal parameters from the vehicle response under operational conditions (Chapter 5). The identified modal characteristics of the railway sleepers further support the selection of the frequency ranges for extracting the track vibrations from the LDV signals (Chapter 4 and 5).

- The speed-dependent characteristics (Chapter 4) support the selection of the vehicle speed range for estimating the load-response relationship of the track structure (Chapter 5).

The main conclusions of the dissertation are summarized as follows.

- The train-borne LDV is capable of directly measuring the track vibrations from the moving vehicle. The measured vibrations can be combined with the wheel-rail force estimated from the measured vehicle vibrations to estimate the transfer function of the track structure over a wide frequency range.

- Among the three stages of speckle noise mitigation (instrumentation, measurement, and post-processing), post-processing is the only one that allows speckle noise to (attempt to) be removed. Incorporating knowledge of the characteristics of structural vibration and speckle noise can improve the performance of speckle noise reduction.

- As train speed increases, the speckle noise increases almost linearly while the track vibration increases nonlinearly. The competition between them leads to the nonlinear behavior of the signal-to-noise ratio with respect to train speed. The speeds that yield the highest signal-to-noise ratio are different for different track structures, measurement configurations, and operational conditions.

- Operational modal identification using the vehicle vibrations passing over joints eliminates the need to define the vehicle stiffness, vehicle damping, and vehicle body mass for estimating the wheel-rail force.

- Among the speeds and frequency range tested, a higher vehicle speed provides smaller deviations in the estimated transfer functions at high frequencies. The

differences in transfer functions between different track sections reflect the variation of track dynamic properties.

This dissertation validates the developed technology at the following three levels.

- Numerical simulations provide insights into the characteristics of speckle noise and track vibration. Chapter 4 establishes numerical models that effectively replicate the sleeper vibration and speckle noise measured in the V-Track test rig at different speeds. The simulation results further support the parameter selection and quantitative validation of the vibration-noise separation method.

- Laboratory measurements in V-Track provide well-controlled and well-observed conditions for testing the train-borne LDV technology. Chapter 2, 4, and 5 demonstrate that the method effectively reduces the speckle noise and extracts the track vibrations from the LDV signals at speeds of 0.5~20 km/h and frequencies up to 1,000~3,000 Hz. Chapter 5 demonstrates the effectiveness of the transfer function estimation at speeds of 8~16 km/h and frequencies up to 800 Hz.

- Field measurements provide realistic conditions to further test the technology and methods. Chapter 4 applies the vibration-noise separation method to the train-borne LDV measurements on the CTO train and investigates the speed-dependent characteristics at speeds of 5~30 km/h and frequencies up to 300 Hz.

The above investigations based on numerical simulations, laboratory measurements, and field measurements yield coherent results. These findings demonstrate the applicability and usability of the train-borne LDV technology for monitoring track dynamic properties over a wide frequency range, thus potentially enabling more efficient and informative rail infrastructure monitoring.

6.2. FURTHER RESEARCH

In the development and validation of train-borne LDV technology for monitoring track dynamic properties, there are still many challenges to overcome and many possibilities to explore. Recommendations for future research are given below.

- We should pay close attention to state-of-the-art technologies of LDV instruments (such as signal diversity techniques) and test their performance for applications of train-borne LDV measurements. This can potentially improve signal quality, especially when measuring small-amplitude, high-frequency, and transient structural vibrations.

- A benchmark dataset can be created based on train-borne LDV measurements from different vehicle speeds. An extensive comparison of different options at each step of the three-step framework for speckle noise reduction is recommended to obtain the best combination of methods in different situations.

- In operational modal identification, structures are usually assumed linear and slightly damped. However, this cannot hold for railway tracks. Another

challenge is the movement of wheel loads. Therefore, the operational modal analysis method needs to be further improved to provide more accurate and robust identification performance.

- The proposed transfer function estimation method needs to be improved in its applicability to vehicles with multiple wheels and the robustness to model errors. Different transfer function estimators with different smoothing strategies should also be investigated to improve the estimation accuracy.

- The performance of train-borne LDV measurements needs to be tested at higher speeds in field measurements, where more severe speckle noise, lower frequency resolution, and more uncertainties are expected. The quantification of uncertainties is essential to enhance the confidence level of the results.

- When more measurement data and deeper understanding are available, machine learning can be applied to the anomaly detection and health monitoring of railway tracks. This can contribute to intelligent infrastructure monitoring and maintenance.

Future development and validation of the train-borne LDV technology should be closely aligned with its potential application to railway track monitoring and its added value to railway asset management. Efforts should be made to continuously increase the validity, usability, and practicality of the monitoring and assessment results for infrastructure managers and contractors. The ultimate goal is to achieve large-scale monitoring and assessment from instrumented operational trains on a daily basis, thus allowing more effective lifespan control and predictive maintenance.

APPENDIX

A.1. TRAIN-TRACK-LDV MODEL

The vehicle and the wheel are modeled as rigid bodies as follows,

$$m_\mathrm{v} \ddot{z}_\mathrm{v}(t) + k_\mathrm{v} \left[z_\mathrm{v}(t) - z_\mathrm{w}(t) \right] + c_\mathrm{v} \left[\dot{z}_\mathrm{v}(t) - \dot{z}_\mathrm{w}(t) \right] = 0 \tag{A.1}$$

$$m_\mathrm{w} \ddot{z}_\mathrm{w} - k_\mathrm{v} \left[z_\mathrm{v}(t) - z_\mathrm{w}(t) \right] - c_\mathrm{v} \left[\dot{z}_\mathrm{v}(t) - \dot{z}_\mathrm{w}(t) \right] + F_\mathrm{c}(t) = 0 \tag{A.2}$$

where m_v and m_w are the masses of the vehicle and the wheel, respectively, k_v and c_v are the stiffness and damping of the suspension, respectively, z_v and z_w are the vertical displacements of the vehicle and the wheel, respectively, and F_c is the wheel-rail force.

The sleepers are also modeled as rigid bodies, and the equation of motion of the i-th sleeper ($i=1, .., n_\mathrm{s}$) is:

$$m_\mathrm{s} \ddot{z}_{\mathrm{s}i}(t) - k_{\mathrm{r}i} \left[z_\mathrm{r}(x_{\mathrm{s}i}, t) - z_{\mathrm{s}i}(t) \right] - c_{\mathrm{r}i} \left[\dot{z}_\mathrm{r}(x_{\mathrm{s}i}, t) - \dot{z}_{\mathrm{s}i}(t) \right] + k_{\mathrm{s}i} z_{\mathrm{s}i}(t) + c_{\mathrm{s}i} \dot{z}_{\mathrm{s}i}(t) = 0 \tag{A.3}$$

where m_s is the mass of the sleeper; $z_{\mathrm{s}i}$ is the displacement of the i-th sleeper, $k_{\mathrm{r}i}$ and $c_{\mathrm{r}i}$ are the stiffness and damping of the rail pad above the i-th sleeper, respectively, $k_{\mathrm{s}i}$ and $c_{\mathrm{s}i}$ are the stiffness and damping of the ballast below the i-th sleeper, respectively, and $x_{\mathrm{s}i}$ is the position of the i-th sleeper, i.e., $x_{\mathrm{s}i}=(i-1/2)d_\mathrm{s}$ with d_s the sleeper spacing.

The rail is modeled as a simply-supported Euler-Bernoulli beam of length $l=n_\mathrm{s} \times d_\mathrm{s}$. Its displacement at position x and time t is characterized as follows [164],

$$EI \frac{\partial^4 z_\mathrm{r}(x,t)}{\partial x^4} + m_\mathrm{r} \frac{\partial^2 z_\mathrm{r}(x,t)}{\partial t^2} = F_\mathrm{c}(t) \delta(x - x_\mathrm{c}(t)) - \sum_{i=1}^{n_\mathrm{s}} k_{\mathrm{r}i} \left[z_\mathrm{r}(x_{\mathrm{s}i}, t) - z_{\mathrm{s}i}(t) \right] \delta(x - x_{\mathrm{s}i})$$
$$- \sum_{i=1}^{n_\mathrm{s}} c_{\mathrm{r}i} \left[\dot{z}_\mathrm{r}(x_{\mathrm{s}i}, t) - \dot{z}_{\mathrm{s}i}(t) \right] \delta(x - x_{\mathrm{s}i}) \tag{A.4}$$

where E is the elastic modulus of the rail, I is the second area moment of the rail, m_r is the mass of the rail per unit length, $\delta(\cdot)$ is the Dirac function, x_c is the position of the wheel, i.e., $x_\mathrm{c}(t)=x_0+vt$ with v denoting the train speed and x_0 denoting the initial position.

According to the Ritz method, the k-th modal coordinate is denoted as $q_k(t)$, and the k-th modal function is defined as follows [164].

$$Z_k(x) = \sqrt{\frac{2}{m_\mathrm{r} l}} \sin \frac{k \pi x}{l} \tag{A.5}$$

The displacement of the rail is approximated as follows,

$$z_\mathrm{r}(x,t) = \sum_{h=1}^{n_\mathrm{m}} Z_h(x) q_h(t) \tag{A.6}$$

where n_m is the truncated order of modes. Then, Eq. (A.4) can be converted into the following second-order ordinary differential equations.

$$\ddot{q}_k(t) + \sum_{i=1}^{n_\mathrm{s}} c_{\mathrm{r}i} Z_k(x_{\mathrm{s}i}) \sum_{h=1}^{n_\mathrm{m}} Z_h(x_{\mathrm{s}i}) \dot{q}_h(t) + \frac{EI}{m_\mathrm{r}} \left(\frac{k\pi}{l} \right)^4 q_k(t) + \sum_{i=1}^{n_\mathrm{s}} k_{\mathrm{r}i} Z_k(x_{\mathrm{s}i}) \sum_{h=1}^{n_\mathrm{m}} Z_h(x_{\mathrm{s}i}) q_h(t)$$
$$- \sum_{i=1}^{n_\mathrm{s}} k_{\mathrm{r}i} z_{\mathrm{s}i}(t) Z_k(x_{\mathrm{s}i}) - \sum_{i=1}^{n_\mathrm{s}} c_{\mathrm{r}i} \dot{z}_{\mathrm{s}i}(t) Z_k(x_{\mathrm{s}i}) = F_\mathrm{c}(t) Z_k(x_\mathrm{c}(t)) \quad k=1,...,n_\mathrm{m} \tag{A.7}$$

The wheel-rail contact force is calculated based on Hertz theory as follows [164],

$$F_c(t) = \begin{cases} \left(\dfrac{1}{G}\left[z_w(t) - z_r(x_c,t) - z_e(x_c)\right] \right)^{3/2} & z_w(t) - z_r(x_c,t) - z_e(x_c) > 0 \\ 0 & z_w(t) - z_r(x_c,t) - z_e(x_c) < 0 \end{cases}$$

(A.8)

where z_e is the rail irregularity, G is a contact coefficient for a conical wheel, i.e., $G = 4.57 r_w^{-0.149} \times 10^{-8}$ m/N$^{2/3}$, and r_w is the wheel radius.
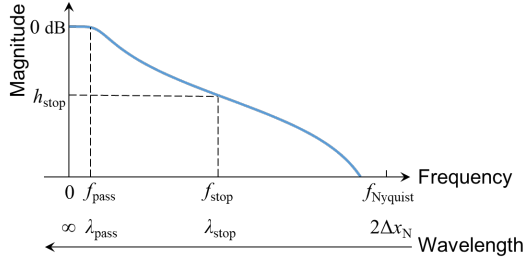

Figure A.1: Spectrum of rail irregularity.

Table A.1: Parameters for simulating track vibration.

Symbol	Parameter	Value	Symbol	Parameter	Value
m_v	Mass of vehicle	50 kg	d	Sleeper width	0.04 m
k_v	Stiffness of suspension	230 kN/m	d_s	Sleeper spacing	0.1258 m
c_v	Damping of suspension	100 N/(m/s)	k_s	Stiffness of sleeper pad	10 MN/m
m_w	Mass of wheel (including axel box)	40 kg	c_s	Damping of sleeper pad	860 N/(m/s)
r_w	Radius of wheel	0.065 m	P_r	Power of Gaussian white noise for rail irregularity	-120 dBW
m_r	Mass of rail per unit length	3.51 kg/m	λ_{pass}	Passband wavelength of rail irregularity	10 mm
I	Second area moment of rail	50,803 mm^4	λ_{stop}	Stopband wavelength of rail irregularity	0.4 mm
n_m	Truncated order of rail modes	25	h_{stop}	Stopband attenuation	55 dB
E	Elastic modulus of rail	205.1 GPa	Δx	Laser-wheel offset	0.063 m
k_r	Stiffness of rail pad	200 MN/m	Δt	Integration step size	1×10^{-5} s
c_r	Damping of rail pad	1.9 kN/(m/s)	γ	Integration parameter	0.5
n_s	Number of sleepers	25	β	Integration parameter	0.25
m_s	Mass of sleeper	1.15 kg			

The rail irregularity z_e is generated (with a spatial interval Δx_N) by applying a low-pass Butterworth infinite impulse response filter to Gaussian white noise. Figure A.1

shows the spectrum of such artificial spatial noise, which is defined by a passband wavelength, a stopband wavelength, and a stopband attenuation.

Eq. (A.1)~(A.3) and (A.7) are solved numerically using the Newmark-β method [163], while the contact force is updated at each step according to Eq. (A.8). The parameters used for simulations are listed in Table A.1.

A.2. SPECKLE TRANSLATION MODEL

The electric field of the reference beam on the photodetector is given as follows [167],

$$E_\mathrm{R} = A_\mathrm{R} \exp\left[i\left(\frac{2\pi}{\lambda} t + \omega_\mathrm{R} t + \theta_\mathrm{R} \right) \right] \tag{A.9}$$

where λ is the laser wavelength, ω_R is an artificial frequency shift, A_R and θ_R represent the amplitude and phase of the reference beam, respectively.

Each speckle is assumed to have its own amplitude and phase, denoted as $A_{\mathrm{S}k}$ and $\theta_{\mathrm{S}k}$, where k represents the k-th speckle. Given the target vibration $z(t)$, the electric field of the k-th speckle is expressed as follows [167].

$$E_{\mathrm{S}k} = A_{\mathrm{S}k} \exp\left[i\left(\frac{2\pi}{\lambda} t - 2\frac{2\pi}{\lambda} z(t) + \theta_{\mathrm{S}k} \right) \right] \tag{A.10}$$

Then, each speckle on the photodetector is heterodyned with the reference beam, and the intensity of such a mixed area is derived as follows [169],

$$\begin{aligned} I_k(t) &= [E_\mathrm{R} + E_{\mathrm{S}k}] \times [E_\mathrm{R} + E_{\mathrm{S}k}]^\mathrm{H} = A_\mathrm{R}^{\,2} + A_{\mathrm{S}k}^{\,2} + 2A_\mathrm{R} A_{\mathrm{S}k} \cos\left(\omega_\mathrm{R} t + \frac{4\pi}{\lambda} z(t) + \theta_\mathrm{R} - \theta_{\mathrm{S}k} \right) \\ &= I_\mathrm{R} + I_{\mathrm{S}k} + 2\sqrt{I_\mathrm{R} I_{\mathrm{S}k}} \cos\left(\omega_\mathrm{R} t + \frac{4\pi}{\lambda} z(t) + \theta_\mathrm{R} - \theta_{\mathrm{S}k} \right) \end{aligned} \tag{A.11}$$

where $^\mathrm{H}$ denotes conjugate transpose, I_R and $I_{\mathrm{S}k}$ are intensities of the reference beam and the k-th speckle, respectively.

The last term in Eq. (A.11) carries the phase change due to the target motion and the laser speckle. After filtering out the DC components and summing up the contributions of all the K speckles, the output of the photodetector is derived as follows [169],

$$u(t) \propto \sum_{k=1}^{K} a_k 2\sqrt{I_\mathrm{R} I_{\mathrm{S}k}} \cos\left(\omega_\mathrm{R} t + \frac{4\pi}{\lambda} z(t) + \theta_\mathrm{R} - \theta_{\mathrm{S}k} \right) = 2\sqrt{I_\mathrm{R}} I_\mathrm{M} \cos\left(\omega_\mathrm{R} t + \frac{4\pi}{\lambda} z(t) + \theta_\mathrm{M} \right) \tag{A.12}$$

where a_k represents the area of the k-th speckle observed on the photodetector, and I_M and θ_M are expressed as follows [166, 169],

$$I_\mathrm{M} = \sqrt{\sum_{p=1}^{K} \sum_{q=1}^{K} a_p a_q \sqrt{I_{\mathrm{S}p} I_{\mathrm{S}q}} \cos\left(\theta_{\mathrm{S}p} - \theta_{\mathrm{S}q} \right)} \tag{A.13}$$

$$\theta_\mathrm{M} = \arctan\left[\frac{\displaystyle\sum_{k=1}^{K} a_k \sqrt{I_{\mathrm{S}k}} \sin\left(\theta_\mathrm{R} - \theta_{\mathrm{S}k} \right)}{\displaystyle\sum_{k=1}^{K} a_k \sqrt{I_{\mathrm{S}k}} \cos\left(\theta_\mathrm{R} - \theta_{\mathrm{S}k} \right)} \right] \tag{A.14}$$

Therefore, the target vibration $z(t)$ can be measured from the frequency of $u(t)$ as follows [167],

$$\omega_D(t) = \omega_R + \frac{4\pi}{\lambda}\dot{z}(t) + \frac{d\theta_M}{dt}(t) \tag{A.15}$$

The phase change rate $d\theta_M/dt$ depends on the properties of the laser speckles and the reference beam. Assuming that the laser is well-focused on the target surface, the space correlation length of the speckles on the photodetector is calculated as follows [168],

$$l_C = \frac{\lambda R}{\pi w} \tag{A.16}$$

where w is the diameter of the laser spot and R is the distance between the target surface and the photodetector. The length l_C describes the size of each speckle, within which the intensity and phase, I_{Sk} and θ_{Sk}, are constant. The intensity and phase of all speckles are assumed to follow the following negative exponential distribution and uniform distribution, respectively [169].

$$P(I_S) = \frac{1}{\langle I_S \rangle}\exp\left(-\frac{I_S}{\langle I_S \rangle}\right) \quad I_S > 0 \tag{A.17}$$

$$P(\theta_S) = \frac{1}{2\pi} \quad -\pi \leq \theta_S \leq \pi \tag{A.18}$$

where $\langle I_S \rangle$ denotes the mean speckle intensity. Random samples of I_{Sk} and θ_{Sk} are generated for each speckle.

Meanwhile, the time correlation length of the speckles on the photodetector is as follows [168],

$$\tau_C = \frac{1}{|v|}\left(\frac{1}{w^2} + \frac{1}{l_C{}^2}\right)^{-1/2} \tag{A.19}$$

where v is the in-plane speed of the laser spot on the surface.

The parameters used for simulations are listed in Table A.2.

Table A.2: Parameters for simulating speckle noise.

Symbol	Parameter	Value	Symbol	Parameter	Value
λ	Wavelength of laser	1,550 nm	m	Number of grids along the translation direction	200
w	Diameter of laser spot	0.19 mm	n	Number of grids along the orthogonal direction	100
a	Number of speckles covered by photodetector length	2	f_C	Cut-off frequency of low-pass filter	100 kHz
R	Distance between target and photodetector	2.7 m			

BIBLIOGRAPHY

[1]   De Man A P. (2002). Dynatrack: A Survey of Dynamic Railway Track Properties and Their Quality. Delft University of Technology.

[2]   Kaewunruen S & Remennikov A M. (2008). Dynamic properties of railway track and its components: a state-of-the-art review. *New Research on Acoustics*, 197-220.

[3]   Carden E P & Fanning P (2004). Vibration based condition monitoring: a review. *Structural Health Monitoring*, 3(4): 355-377.

[4]   Beskhyroun S, Wegner L D, Sparling B F. (2012). New methodology for the application of vibration‑based damage detection techniques. *Structural Control and Health Monitoring*, 19(8): 632-649.

[5]   Lam H F, Wong M T, Yang Y B. (2012). A feasibility study on railway ballast damage detection utilizing measured vibration of in situ concrete sleeper. *Engineering Structures*, 45: 284-298.

[6]   Oregui M, Li Z, Dollevoet R. (2015). Identification of characteristic frequencies of damaged railway tracks using field hammer test measurements. *Mechanical Systems and Signal Processing*, 54: 224-242.

[7]   Janeliukstis R, Clark A, Rucevskis S, et al. (2017). Vibration-based damage identification in railway concrete sleepers. In the 4th Conference on Smart Monitoring, Assessment and Rehabilitation of Civil Structures.

[8]   Shen C, Dollevoet R, Li Z. (2021). Fast and robust identification of railway track stiffness from simple field measurement. *Mechanical Systems and Signal Processing*, 152: 107431.

[9]   Le Pen L, Milne D, Thompson D, et al. (2016). Evaluating railway track support stiffness from trackside measurements in the absence of wheel load data. *Canadian Geotechnical Journal*, 53(7): 1156-1166.

[10]   Yue G D, Xu Z, Wang L, et al. (2016). WSN-based vibration characteristic research for various railway track structures for pattern classification. *International Journal of Pattern Recognition and Artificial Intelligence*, 30(10): 1650020.

[11]   Boogaard M A, Li Z, Dollevoet R. (2018). In situ measurements of the crossing vibrations of a railway turnout. *Measurement*, 125: 313-324.

[12]   Shen C, Li Z, Dollovoet R. (2020). A novel method for railway crossing monitoring based on ambient vibration caused by train-track interaction. In Proceedings of the 26th Symposium of the International Association of Vehicle System Dynamics, 133-141.

[13]   Liu G, Li P, Wang P, et al. (2021). Study on structural health monitoring of vertical vibration of ballasted track in high-speed railway. *Journal of Civil Structural Health Monitoring*, 11: 451-463.

[14]   Li Z, Molodova M, Núñez A, et al. (2015). Improvements in axle box acceleration measurements for the detection of light squats in railway infrastructure. *IEEE Transactions on Industrial Electronics*, 62(7): 4385-4397.

[15] Li J & Shi H. (2019). Rail corrugation detection of high-speed railway using wheel dynamic responses. *Shock and Vibration*, 2695647.

[16] Wei Z, Núñez A, Li Z, et al. (2017). Evaluating degradation at railway crossings using axle box acceleration measurements. *Sensors*, 17(10): 2236.

[17] Quirke P, Cantero D, OBrien E J, et al. (2017). Drive-by detection of railway track stiffness variation using in-service vehicles. *Proceedings of the Institution of Mechanical Engineers, Part F: Journal of Rail and Rapid Transit*, 231(4): 498-514.

[18] OBrien E J, Quirke P, Bowe C, et al. (2018). Determination of railway track longitudinal profile using measured inertial response of an in-service railway vehicle. *Structural Health Monitoring*, 17(6): 1425-1440.

[19] Castillo-Mingorance J M, Sol-Sánchez M, Moreno-Navarro F, et al. (2020). A critical review of sensors for the continuous monitoring of smart and sustainable railway infrastructures. *Sustainability*, 12(22): 9428.

[20] Li C, He Q, Wang P. (2022). Estimation of railway track longitudinal irregularity using vehicle response with information compression and Bayesian deep learning. *Computer‑Aided Civil and Infrastructure Engineering*, 37(10): 1260-1276.

[21] Sresakoolchai J & Kaewunruen S. (2022). Prognostics of unsupported railway sleepers and their severity diagnostics using machine learning. *Scientific Reports*, 12(1): 6064.

[22] Shen C, Zhang P, Dollevoet R, et al. (2023). Evaluating railway track stiffness using axle box accelerations: A digital twin approach. *Mechanical Systems and Signal Processing*, 204: 110730.

[23] Berggren E. (2009). Railway Track stiffness: Dynamic Measurements and Evaluation for Efficient Maintenance. KTH Royal Institute of Technology.

[24] Wang P, Wang L, Chen R, et al. (2016). Overview and outlook on railway track stiffness measurement. *Journal of Modern Transportation*, 24(2): 89-102.

[25] Castellini P, Martarelli M, Tomasini E P. (2006). Laser Doppler vibrometry: development of advanced solutions answering to technology's needs. *Mechanical Systems and Signal Processing*, 20(6): 1265-1285.

[26] Lutzmann P, Göhler B, Van Putten F, et al. (2011). Laser vibration sensing: overview and applications. In Electro-Optical Remote Sensing, Photonic Technologies, and Applications V, 8186, 11-26.

[27] Rothberg S J, Allen M S, Castellini P, et al. (2017). An international review of laser Doppler vibrometry: Making light work of vibration measurement. *Optics and Lasers in Engineering*, 99: 11-22.

[28] Li Z & Rixen D. (2011). Method for detection of a flaw or flaws in a railway track, and a rail vehicle to be used in such a method. Patent NL 2007315. PCT/NL2012/050586, WO2013/032322A1.

[29] OBrien E J & Malekjafarian A. (2016). A mode shape-based damage detection approach using laser measurement from a vehicle crossing a simply supported bridge. *Structural Control and Health Monitoring*, 23(10): 1273-1286.

[30] Kaynardag K, Battaglia G, Ebrahimkhanlou A, et al. (2021). Identification of bending modes of vibration in rails by a laser Doppler vibrometer on a moving platform. *Experimental Techniques*, 45(1), 13-24 .

[31] Kaynardag, K., Yang, C. Salamone, S., (2023). A rail defect detection system based on laser Doppler vibrometer measurements. *NDT & E International*, 102858.

[32] Martin P & Rothberg S. (2009). Introducing speckle noise maps for laser vibrometry. *Optics and Lasers in Engineering*, 47(3-4): 431-442.

[33] Gasparetti M & Revel G M. (1999). The influence of operating conditions on the accuracy of in-plane laser Doppler velocimetry measurements. *Measurement*, 26(3): 207-220.

[34] Vass J, Šmíd R, Randall R B, et al. (2008). Avoidance of speckle noise in laser vibrometry by the use of kurtosis ratio: Application to mechanical fault diagnostics. *Mechanical Systems and Signal Processing*, 22(3): 647-671.

[35] Muramatsu M, Uchida S, Takahashi Y. (2020). Noncontact detection of concrete flaws by neural network classification of laser doppler vibrometer signals. *Engineering Research Express*, 2(2): 025017.

[36] Castellini P & Montanini R. (2002). Automotive components vibration measurements by tracking laser Doppler vibrometry: advances in signal processing. *Measurement Science and Technology*, 13(8): 1266.

[37] Wang Y, Zhang W, Wu Z, et al. (2021). Speckle noise detection and removal for laser speech measurement systems. *Applied Sciences*, 11(21): 9870.

[38] Arruda J R D F, Vianna do Rio S A, Bernardes Santos L A S. (1996). A space-frequency data compression method for spatially dense laser doppler vibrometer measurements. *Shock and Vibration*, 3(2): 127-133.

[39] Siringoringo D M & Fujino Y. (2006). Experimental study of laser Doppler vibrometer and ambient vibration for vibration-based damage detection. *Engineering Structures*, 28(13): 1803-1815.

[40] Revel G M, Castellini P, Chiariotti P, et al. (2011). Laser vibrometry vibration measurements on vehicle cabins in running conditions: helicopter mock-up application. *Optical Engineering*, 50(10): 101502.

[41] Martarelli M & Ewins D J. (2006). Continuous scanning laser Doppler vibrometry and speckle noise occurrence. *Mechanical Systems and Signal Processing*, 20(8): 2277-2289.

[42] Di Maio D, Castellini P, Martarelli M, et al. (2021). Continuous Scanning Laser Vibrometry: A raison d'être and applications to vibration measurements. *Mechanical Systems and Signal Processing*, 156: 107573.

[43] Stanbridge A B, Martarelli M, Ewins D J. (2004). Measuring area vibration mode shapes with a continuous-scan LDV. *Measurement*, 35(2): 181-189.

[44] Allen M S & Sracic M W. (2010). A new method for processing impact excited continuous-scan laser Doppler vibrometer measurements. *Mechanical Systems and Signal Processing*, 24(3): 721-735.

[45] Chen D M, Xu Y F, Zhu W D. (2016). Damage identification of beams using a continuously scanning laser Doppler vibrometer system. *Journal of Vibration and Acoustics*, 138(5): 051011.

[46] Xu Y F, Chen D M, Zhu W D. (2017). Damage identification of beam structures using free response shapes obtained by use of a continuously scanning laser Doppler vibrometer system. *Mechanical Systems and Signal Processing*, 92: 226-247.

[47] Xu Y F, Chen D M, Zhu W D. (2019). Operational modal analysis using lifted continuously scanning laser Doppler vibrometer measurements and its application to baseline-free structural damage identification. *Journal of Vibration and Control*, 25(7): 1341-1364.

[48] Sracic M W & Allen M S. (2009). Experimental investigation of the effect of speckle noise on continuous scan laser Doppler vibrometer measurements. In 27th International Modal Analysis Conference.

[49] Aranchuk V, Lal A K, Hess C.F, et al. (2006). Speckle noise in a continuously scanning multibeam laser Doppler vibrometer for acoustic landmine detection. In Detection and Remediation Technologies for Mines and Minelike Targets XI, 6217: 366-375.

[50] Libbey B, Fenneman D, Burns B. (2005). Mobile platform for acoustic mine detection applications. In Detection and Remediation Technologies for Mines and Minelike Targets X, 5794: 683-693.

[51] Jiang L A, Albota M A, Haupt R W, et al. (2011). Laser vibrometry from a moving ground vehicle. *Applied Optics*, 50(15): 2263-2273.

[52] Rahimi S, Li Z, Dollevoet R. (2014). Measuring with laser Doppler vibrometer on moving frame (LDVMF). In AIP Conference Proceedings, 1600(1): 274-286.

[53] Lv T, Han X, Wu S, et al. (2019). The effect of speckles noise on the Laser Doppler Vibrometry for remote speech detection. *Optics Communications*, 440: 117-125.

[54] Rembe C & Dräbenstedt A. (2015). Speckle-Insensitive Laser-Doppler Vibrometry with Adaptive Optics and Signal Diversity. In Proceedings SENSOR 2015, D1: 505-510.

[55] Van Zandt N R & Spencer M F. (2020). Improved adaptive-optics performance using polychromatic speckle mitigation. *Applied Optics*, 59(4): 1071-1081.

[56] Zhu J, Li Y, Baets R. (2019). Mitigation of speckle noise in laser Doppler vibrometry by using a scanning average method. *Optics Letters*, 44(7): 1860-1863.

[57] Dräbenstedt A. (2014). Diversity combining in laser Doppler vibrometry for improved signal reliability. In AIP Conference Proceedings, 1600(1): 263-273.

[58] Courville S W & Sava P C. (2020). Speckle noise attenuation in orbital laser vibrometer seismology. *Acta Astronautica*, 172: 16-32.

[59] Schewe M & Rembe C. (2021). Signal diversity for laser-Doppler vibrometers with raw-signal combination. *Sensors*: 21(3), 998.

[60] Schewe M & Rembe C. (2021). Analyzing real-time capability of raw laser-Doppler vibrometer signal combination for signal diversity. In Optical Measurement Systems for Industrial Inspection XII, 11782: 55-63.

[61] Oliver D E, Palan V, Bissinger G, et al. (2007). 3-dimensional laser doppler vibration analysis of a stradivarius violin. In Proceedings of the 25th International Modal Analysis Conference, 10-14.

[62] Jin Y & Li Z. (2021). Eliminating speckle noises for laser doppler vibrometer based on empirical wavelet transform. In 2021 13th International Conference on Measurement, 72-75.

[63] Jin Y & Li Z. (2022). Mitigating speckle noise in a laser Doppler vibrometer using Fourier analysis. *Optics Letters*, 47(18): 4742-4745.

[64] Jin Y, Dollevoet R, Li Z. (2022). Removing speckle noise from the signals of a laser Doppler vibrometer on moving platforms (LDVom) by ensemble empirical mode decomposition. *Measurement Science and Technology*, 33(12): 125205.

[65] Peeters B & De Roeck G. (2001). Stochastic system identification for operational modal analysis: a review. *Journal of Dynamic Systems, Measurement, and Control*, 123(4): 659-667.

[66] Rainieri C & Fabbrocino G. (2014). Operational Modal Analysis of Civil Engineering Structures. Springer, New York, 103-210.

[67] Zahid F B, Ong Z C, Khoo S Y. (2020). A review of operational modal analysis techniques for in-service modal identification. *Journal of the Brazilian Society of Mechanical Sciences and Engineering*, 42: 1-18.

[68] Yuen K V & Katafygiotis L S. (2001). Bayesian time–domain approach for modal updating using ambient data. *Probabilistic Engineering Mechanics*, 16(3): 219-231.

[69] Guillaume P, Verboven P, Vanlanduit S. (1998). Frequency-domain maximum likelihood identification of modal parameters with confidence intervals. In Proceedings of the International Seminar on Modal Analysis, 359-366.

[70] Javh J, Slavič J, Boltežar M. (2018). High frequency modal identification on noisy high-speed camera data. *Mechanical Systems and Signal Processing*, 98: 344-351.

[71] Au S K, Zhang F L, Ni Y C. (2013). Bayesian operational modal analysis: theory, computation, practice. *Computers & Structures*, 126: 3-14.

[72] Yan W J & Katafygiotis L S. (2015). A two-stage fast Bayesian spectral density approach for ambient modal analysis. Part I: Posterior most probable value and uncertainty. *Mechanical Systems and Signal Processing*, 54: 139-155.

[73] Au S K (2011). Fast Bayesian FFT method for ambient modal identification with separated modes. *Journal of Engineering Mechanics*, 137(3): 214-226.

[74] Lam H F, Hu J, Yang J H. (2017). Bayesian operational modal analysis and Markov chain Monte Carlo-based model updating of a factory building. *Engineering Structures*, 132: 314-336.

[75] Li B & Au S K. (2019). An expectation-maximization algorithm for Bayesian operational modal analysis with multiple (possibly close) modes. *Mechanical Systems and Signal Processing*, 132: 490-511.

[76] Au S K. (2012). Fast Bayesian ambient modal identification in the frequency domain, Part I: Posterior most probable value. *Mechanical Systems and Signal Processing*, 26: 60-75.

[77] Shih C Y, Tsuei Y G, Allemang R J, et al. (1988). Complex mode indication function and its applications to spatial domain parameter estimation. *Mechanical Systems and Signal Processing*, 2(4): 367-377.

[78] Brincker R, Zhang L, Andersen P. (2001). Modal identification of output-only systems using frequency domain decomposition. *Smart Materials and Structures*, 10(3): 441.

[79] Elhattab A, Uddin N, OBrien E. (2017). Identifying Localized Bridge Damage Using Frequency Domain Decomposition. In 26th ASNT Research Symposium, 75-83.

[80] Alamdari M M, Anaissi A, Khoa N L, et al. (2019). Frequency domain decomposition-based multisensor data fusion for assessment of progressive damage in structures. *Structural Control and Health Monitoring*, 26(2): e2299.

[81] Lin S T, Lu Y, Alamdari M M, et al. (2020). Field test investigations for condition monitoring of a concrete culvert bridge using vibration responses. *Structural Control and Health Monitoring*, 27(10): e2614.

[82] Brincker R, Ventura C E, Andersen P. (2001). Damping estimation by frequency domain decomposition. In Proceedings of IMAC 19: a Conference on Structural Dynamics, 698-703.

[83] Brewick P T & Smyth A W. (2013). An investigation of the effects of traffic induced local dynamics on global damping estimates using operational modal analysis. *Mechanical Systems and Signal Processing*, 41(1-2): 433-453.

[84] Wang T, Zhang L, Tamura Y. (2005). An operational modal analysis method in frequency and spatial domain. *Earthquake Engineering and Engineering Vibration*, 4(2): 295-300.

[85] Zhang L, Wang T, Tamura Y. (2010). A frequency–spatial domain decomposition (FSDD) method for operational modal analysis. *Mechanical Systems and Signal Processing*, 24(5): 1227-1239.

[86] Pioldi F, Ferrari R, Rizzi E. (2016). Output-only modal dynamic identification of frames by a refined FDD algorithm at seismic input and high damping. *Mechanical Systems and Signal Processing*, 68: 265-291.

[87] Pioldi F, Ferrari R, Rizzi E. (2017). Earthquake structural modal estimates of multi-storey frames by a refined Frequency Domain Decomposition algorithm. *Journal of Vibration and Control*, 23(13): 2037-2063.

[88] Hızal Ç. (2020). Modified frequency and spatial domain decomposition method based on maximum likelihood estimation. *Engineering Structures*, 224: 111007.

[89] Ghahari S F, Abazarsa F, Ghannad M A, et al. (2014). Blind modal identification of structures from spatially sparse seismic response signals. *Structural Control and Health Monitoring*, 21(5): 649-674.

[90] Yao X J, Yi T H, Qu C, et al. (2018). Blind modal identification using limited sensors through modified sparse component analysis by time-frequency method. *Computer-Aided Civil and Infrastructure Engineering*, 33(9): 769-782.

[91] Lardies J & Gouttebroze S. (2002). Identification of modal parameters using the wavelet transform. *International Journal of Mechanical Sciences*, 44(11): 2263-2283.

[92] Le T P & Argoul P. (2004). Continuous wavelet transform for modal identification using free decay response. *Journal of Sound and Vibration*, 277(1-2): 73-100.

[93] Ülker-Kaustell M & Karoumi R. (2011). Application of the continuous wavelet transform on the free vibrations of a steel–concrete composite railway bridge. *Engineering Structures*, 33(3): 911-919.

[94] Le T P & Paultre P. (2012). Modal identification based on continuous wavelet transform and ambient excitation tests. *Journal of Sound and Vibration*, 331(9): 2023-2037.

[95] Le T P & Paultre P. (2013). Modal identification based on the time–frequency domain decomposition of unknown-input dynamic tests. *International Journal of Mechanical Sciences*, 71: 41-50.

[96] Le T P & Argoul P. (2015). Distinction between harmonic and structural components in ambient excitation tests using the time–frequency domain decomposition technique. *Mechanical Systems and Signal Processing*, 52: 29-45.

[97] Milne D R M, Le Pen L M, Thompson D J, et al. (2017). Properties of train load frequencies and their applications. *Journal of Sound and Vibration*, 397: 123-140.

[98] Yue G D, Xu Z, Wang L D, et al. (2017). Vibration analysis for slab track at different train speeds using Bayes wavelet denoising. *Proceedings of the Institution of Mechanical Engineers, Part F: Journal of Rail and Rapid Transit*, 231(8): 892-901.

[99] Auersch L. (2006). Ground vibration due to railway traffic—The calculation of the effects of moving static loads and their experimental verification. *Journal of Sound and Vibration*, 293(3-5): 599-610.

[100] Bian X, Jiang H, Chang C, et al. (2015). Track and ground vibrations generated by high-speed train running on ballastless railway with excitation of vertical track irregularities. *Soil Dynamics and Earthquake Engineering*, 76: 29-43.

[101] Jin Y, Dollevoet R, Li Z. (2022). Numerical simulation and characterization of speckle noise for laser Doppler vibrometer on moving platforms (LDVom). *Optics and Lasers in Engineering*, 158: 107135.

[102] Knothe K & Wu Y. (1998). Receptance behaviour of railway track and subgrade. *Archive of Applied Mechanics*, 68: 457-470.

[103] Agostinacchio M, Ciampa D, Diomedi M, et al. (2013). Parametrical analysis of the railways dynamic response at high speed moving loads. *Journal of Modern Transportation*, 21(3): 169-181.

[104] Arlaud E, D'aguiar S C, Balmes E. (2016). Receptance of railway tracks at low frequency: Numerical and experimental approaches. *Transportation Geotechnics*, 9: 1-16.

[105] Wei L, Zeng J, Wu P, et al. (2018). Safety analysis of high speed trains under cross winds using indirect wheel-rail force measuring method. *Journal of Wind Engineering and Industrial Aerodynamics*, 183: 55-67.

[106] Urda P, Muñoz S, Aceituno J F, et al. (2020). Wheel-rail contact force measurement using strain gauges and distance lasers on a scaled railway vehicle. *Mechanical Systems and Signal Processing*, 138: 106555.

[107] Xia F, Cole C, Wolfs P. (2008). Grey box-based inverse wagon model to predict wheel–rail contact forces from measured wagon body responses. *Vehicle System Dynamics*, 46(S1): 469-479.

[108] Pourzeynali S, Zhu X, Ghari Zadeh A, et al. (2021). Comprehensive study of moving load identification on bridge structures using the explicit form of newmark-β method: Numerical and experimental studies. *Remote Sensing*, 13(12): 2291.

[109] Wu J, Zhu T, Wang Y, et al. (2022). TSVD Regularization-Parameter Selection Method Based on Wilson-θ and Its Application to Vertical Wheel-Rail Force Identification of Rail Vehicles. *Shock and Vibration*, 2022: 2598040.

[110] Zhu T, Wang X R, Fan Y W, et al. (2022). A time domain method for wheel-rail force identification of rail vehicles. *Vehicle System Dynamics*, 60(3): 790-809.

[111] Ljung L. (1985). On the estimation of transfer functions. *Automatica*, 21(6): 677-696.

[112] Broersen P M. (1994). A comparison of transfer function estimators. In Conference Proceedings 1994 IEEE Instrumentation and Measurement Technolgy Conference, 1377-1380.

[113] Stenman A, Gustafsson F, Rivera D E, et al. (2000). On adaptive smoothing of empirical transfer function estimates. *Control Engineering Practice*, 8(11): 1309-1315.

[114] Lataire J & Chen T. (2016). Transfer function and transient estimation by Gaussian process regression in the frequency domain. *Automatica*, 72: 217-229.

[115] Naeimi M, Li Z, Petrov R H, et al. (2018). Development of a new downscale setup for wheel-rail contact experiments under impact loading conditions. *Experimental Techniques*, 42: 1-17.

[116] Zhang P, Moraal J, Li Z. (2021). Design, calibration and validation of a wheel-rail contact force measurement system in V-Track. *Measurement*, 175: 109105.

[117] Lin J & Qu L. (2000). Feature extraction based on Morlet wavelet and its application for mechanical fault diagnosis. *Journal of Sound and Vibration*, 234(1): 135-148.

[118] Mallat S G. (1989). A theory for multiresolution signal decomposition: the wavelet representation. *IEEE Transactions on Pattern Analysis and Machine Intelligence*, 11(7): 674-693.

[119] Bilen C & Huzurbazar S. (2002). Wavelet-based detection of outliers in time series. *Journal of Computational and Graphical Statistics*, 11(2): 311-327.

[120] Grané A & Veiga H. (2010). Wavelet-based detection of outliers in financial time series. *Computational Statistics & Data Analysis*, 54(11): 2580-2593.

[121] del Ser D, Fors O, Núñez J. (2018). TFAW: Wavelet-based signal reconstruction to reduce photometric noise in time-domain surveys. *Astronomy & Astrophysics*, 619: A86.

[122] Pratama I, Permanasari A E, Ardiyanto I, et al. (2016). A review of missing values handling methods on time-series data. In 2016 International Conference on Information Technology Systems and Innovation, 1-6.

[123] Qu F, Liu J, Ma Y, et al. (2020). A novel wind turbine data imputation method with multiple optimizations based on GANs. *Mechanical Systems and Signal Processing*, 139: 106610.

[124] Akouemo H N & Povinelli R J. (2014). Time series outlier detection and imputation. In 2014 IEEE PES General Meeting| Conference & Exposition, 1-5.

[125] Liu H, Shah S, Jiang W. (2004). On-line outlier detection and data cleaning. *Computers & Chemical Engineering*, 28(9): 1635-1647.

[126] Layanun V, Suksamosorn S, Songsiri J. (2017). Missing-data imputation for solar irradiance forecasting in Thailand. In 2017 56th Annual Conference of the Society of Instrument and Control Engineers of Japan, 1234-1239.

[127] Box G E, Jenkins G M, Reinsel G C, et al. (2015). Time Series Analysis: Forecasting and Control. John Wiley & Sons.

[128] Chang I, Tiao G C, Chen C. (1988). Estimation of time series parameters in the presence of outliers. *Technometrics*, 30(2): 193-204.

[129] Jones R H. (1980). Maximum likelihood fitting of ARMA models to time series with missing observations. *Technometrics*, 22(3): 389-395.

[130] Wu S F, Chang C Y, Lee S J. (2015). Time series forecasting with missing values. In 2015 1st International Conference on Industrial Networks and Intelligent Systems, 151-156.

[131] Akaike H. (1974). A new look at the statistical model identification. *IEEE Transactions on Automatic Control*, 19(6): 716-723.

[132] Butterworth S. (1930). On the theory of filter amplifiers. *Wireless Engineer*, 7(6): 536-541.

[133] Bianchi G & Sorrentino R. (2007). Electronic Filter Simulation & Design. McGraw Hill Professional.

[134] Amrouche B & Le Pivert X. (2014). Artificial neural network based daily local forecasting for global solar radiation. *Applied Energy*, 130: 333-341.

[135] Demirhan H & Renwick Z. (2018). Missing value imputation for short to mid-term horizontal solar irradiance data. *Applied Energy*, 225: 998-1012.

[136] Dhevi A S. (2014). Imputing missing values using Inverse Distance Weighted Interpolation for time series data. In 2014 Sixth international conference on advanced computing, 255-259.

[137] Zhang P & Li F. (2014). A new adaptive weighted mean filter for removing salt-and-pepper noise. *IEEE Signal Processing Letters*, 21(10): 1280-1283.

[138] Wen Y & Zeng B. (1999). A simple nonlinear filter for economic time series analysis. *Economics Letters*, 64(2): 151-160.

[139] Nodes T & Gallagher N. (1982). Median filters: Some modifications and their properties. *IEEE Transactions on Acoustics, Speech, and Signal Processing*, 30(5): 739-746.

[140] Lee J S. (1986). Speckle suppression and analysis for synthetic aperture radar images. *Optical Engineering*, 25(5): 636-643.

[141] Lee J S. (1983). A simple speckle smoothing algorithm for synthetic aperture radar images. *IEEE Transactions on Systems, Man, and Cybernetics*, 1: 85-89.

[142] Pan Q, Zhang L, Dai G, et al. (1999). Two denoising methods by wavelet transform. *IEEE Transactions on Signal Processing*, 47(12): 3401-3406.

[143] Shakher C, Kumar R, Singh S K, et al. (2002). Application of wavelet filtering for vibration analysis using digital speckle pattern interferometry. *Optical Engineering*, 41(1): 176-180.

[144] Brandt A, Brincker R. (2014). Integrating time signals in frequency domain–Comparison with time domain integration. *Measurement*, 58: 511-519.

[145] Wu T X & Thompson D J. (2004). The effects of track non-linearity on wheel/rail impact. *Proceedings of the Institution of Mechanical Engineers, Part F: Journal of Rail and Rapid Transit*, 218(1): 1-15.

[146] Oregui M, De Man A, Woldekidan M F, et al. (2016). Obtaining railpad properties via dynamic mechanical analysis. *Journal of Sound and Vibration*, 363: 460-472.

[147] Sadeghi J, Seyedkazemi M, Khajehdezfuly A. (2020). Nonlinear simulation of vertical behavior of railway fastening system. *Engineering Structures*, 209: 110340.

[148] Welch P. (1967). The use of fast Fourier transform for the estimation of power spectra: a method based on time averaging over short, modified periodograms. *IEEE Transactions on Audio and Electroacoustics*, 15(2): 70-73.

[149] Hızal Ç & Aktaş E. (2021). Probabilistic investigation of error propagation in frequency domain decomposition‑based operational modal analysis. *Structural Control and Health Monitoring*, 28(8): e2759.

[150] Mitra S K. (2001). Digital Signal Processing: A Computer-based Approach. McGraw-Hill Higher Education.

[151] Buades A, Coll B, Morel JM. (2005). A review of image denoising algorithms, with a new one. *Multiscale Modeling and Simulation*, 4(2): 490-530.

[152] Fan L, Zhang F, Fan H, et al. (2019). Brief review of image denoising techniques. *Visual Computing for Industry, Biomedicine, and Art*, 2(1): 1-12.

[153] Getreuer P. (2013). A survey of Gaussian convolution algorithms. *Image Processing On Line*, 3: 286-310.

[154] Ling W K. (2010). Nonlinear Digital Filters: Analysis and Applications. Academic Press.

[155] Singh H, Raj J, Kaur G, et al. (2004). Image fusion using fuzzy logic and applications. In 2004 IEEE International Conference on Fuzzy Systems, 1: 337-340.

[156] Zhu M & Yang Y. (2008). A new image fusion algorithm based on fuzzy logic. In 2008 International Conference on Intelligent Computation Technology and Automation, 2: 83-86.

[157] Balasubramaniam P & Ananthi V P. (2014). Image fusion using intuitionistic fuzzy sets. *Information Fusion*, 20: 21-30.

[158] Fladung W A. (1997). Windows used for impact testing. In Proceedings-SPIE The International Society for Optical Engineering, 1662-1666.

[159] Zhang P, Li S, Núñez A, et al. (2021). Multimodal dispersive waves in a free rail: Numerical modeling and experimental investigation. *Mechanical Systems and Signal Processing*, 150: 107305.

[160] Rao SS. (2011). Mechanical Vibrations. USA: Pearson, 721-729.

[161] Kaewunruen S & Remennikov A M. (2006). Sensitivity analysis of free vibration characteristics of an in situ railway concrete sleeper to variations of rail pad parameters. *Journal of Sound and Vibration*, 298(1-2): 453-461.

[162] Allemang R J & Brown D L. (1987). Experimental modal analysis and dynamic component synthesis. Volume 3: modal parameter estimation. Cincinnati University Department of Mechanical and Industrial Engineering.

[163] Newmark N M. (1959). A method of computation for structural dynamics. *Journal of the Engineering Mechanics Division*, 85(3): 67-94.

[164] Zhai W. (2020). Vehicle–Track Coupled Dynamics. Singapore: Springer.

[165] Rothberg S J & Tirabassi M. (2012). A universal framework for modelling measured velocity in laser vibrometry with applications. *Mechanical Systems and Signal Processing*, 26: 141-166.

[166] Rothberg S J & Halkon B J. (2004). Laser vibrometry meets laser speckle. In Sixth International Conference on Vibration Measurements by Laser Techniques: Advances and Applications, 5503: 280-291. SPIE.

[167] Martarelli M. (2001). Exploiting the Laser Scanning Facility for Vibration Measurements. University of London.

[168] Asakura T & Takai N. (1981). Dynamic laser speckles and their application to velocity measurements of the diffuse object. *Applied Physics*. 25: 179-94.

[169] Denman M, Halliwell N A, Rothberg S J. (1996). Speckle noise reduction in laser vibrometry: experimental and numerical optimisation. In Second International Conference on Vibration Measurements by Laser Techniques: Advances and Applications, 280-291.

[170] Rothberg S. (2006). Numerical simulation of speckle noise in laser vibrometry. *Applied Optics*, 45(19): 4523-4533.

ACKNOWLEDGMENTS

Europe's Rail

**Co-funded by
the European Union**

CURRICULUM VITAE

Yuanchen Zeng

Nov. 12, 1993	Born in Hebei, China

EDUCATION

Feb. 2020 – Dec. 2023	PhD Thesis: *Monitoring dynamic properties of railway tracks using train-borne vibrometer measurement* Delft University of Technology, The Netherlands
Sep. 2019 – Feb. 2020	Visiting PhD Delft University of Technology, The Netherlands
Sep. 2016 – Sep. 2022	PhD (Master-PhD combined program) Thesis: *Physics-based data-driven methods for health management of high-speed train wheels* Southwest Jiaotong University, China
Sep. 2012 – Jun. 2016	Bachelor in Mechatronics Engineering Zhejiang University, China

EMPLOYMENT

Sep. 2023 – Present	Postdoctoral researcher Delft University of Technology, The Netherlands
Jun. 2015 – Oct. 2015	Marketing Intern CRRC Hangzhou Vehicle Co., Ltd.

LIST OF PUBLICATIONS

JOURNAL PAPERS

1. **Zeng Y**, Nunez A, Li Z. (2022). Speckle noise reduction for structural vibration measurement with laser Doppler vibrometer on moving platform. *Mechanical Systems and Signal Processing*, 178: 109196.

2. **Zeng Y**, Shen C, Nunez A, Dollevoet R, Zhang W, Li Z. (2023). An interpretable method for operational modal analysis in time-frequency representation and its applications to railway sleepers. *Structural Control and Health Monitoring*, 2023: 6420772.

3. **Zeng Y**, Nunez A, Li Z. (2023). Railway sleeper vibration measurement by train-borne laser Doppler vibrometer and its speed-dependent characteristics. Submitted.

4. **Zeng Y**, Nunez A, Li Z. (2023). Estimating transfer functions of railway tracks using laser Doppler vibrometer and accelerometer measurement on a moving vehicle. Submitted.

CONFERENCE PAPERS

1. **Zeng Y**, Nunez A, Li Z. (2023). A Simulation study on characterizing transfer functions of railway tracks using train-borne laser Doppler vibrometer. *International Conference on Experimental Vibration Analysis for Civil Engineering Structures*, 183-192, Cham: Springer Nature Switzerland.

2. **Zeng Y**, Nunez A, Li Z. (2023). Incorporating modal testing into dynamic load identification from structural vibration measurement. *The 14th International Workshop on Structural Health Monitoring*, Accepted.